ATLAS-ASSISTED ASSESSMENT AND DIAGNOSIS OF ALZHEIMER'S DISEASE FROM NEUROIMAGES

G. QIAN

ATLAS-ASSISTED ASSESSMENT AND DIAGNOSIS OF ALZHEIMER'S DISEASE FROM NEUROIMAGES

Guoyu Qian

(B.Eng, M.Sc)

A thesis submitted for the degree of Doctor of Philosophy

School of Design, Communication and Information Technology

Faculty of Science and Information Technology

The University of Newcastle, Australia

November 2010

Declaration

This thesis contains no material which has been accepted for the award of any other degree or diploma in any university or other tertiary institution and, to the best of my knowledge and belief, contains no material previously published or written by another person, except where due reference has been made in the text. I give consent to this copy of my thesis, when deposited in the University Library, being made available for loan and photocopying subject to the provisions of the Copyright Act 1968.

Guoyu Qian

Acknowledgements

First and foremost I would like to express my sincerest gratitude to my supervisors Dr. Suhuai Luo, Professor Jesse Jin, and Professor Wieslaw L. Nowinski, for their supervision, advice, and guidance from the very early stage of this research to the completion of this thesis. I am extremely grateful to Dr. Luo and Prof. Jin for their encouragements, numerous discussions, insightful comments, and a wide range of helps and assistances. I also gratefully acknowledge Prof. Nowinski for his continuous support of my PhD study and research, his valuable time, his patience, and his immense knowledge, in all the time of research and writing of the papers and this thesis.

I convey special acknowledgement to Professor Xuezhen Shen from Shanghai Lixin University of Commerce, for her indispensable help dealing with the statistical analysis on the large number of collected data.

My sincere thanks also go to the friendly staff members of the School of Design, Communication and Information Technology for the great supports, and the officers of the Office of Graduate Studies for the impressive assistances.

I would also like to thank my wife for supporting me throughout all my studies at University.

Finally, I would like to thank everybody who is important to the successful completion of the thesis, as well as expressing my apology that I could not mention personally one by one.

Table of Contents

Abstract

The human brain is the most complicated biological organ. Despite the intensive research on the brain, it still remains a great mystery. Neurodegenerative diseases such as dementia are recognized as a major health problem and are becoming increasingly common at present time, particularly with aging population. This thesis investigates the problems and limitations of current approach of assessment and diagnosis for Alzheimer's disease (AD), a major form of dementia, and presents a rapid and automatic method of cognitive assessment and disease diagnosis by processing the neuroimages and performing the statistical analysis.

The neuroimage processing in this thesis is based on a set of fully automatic image processing algorithms and a digital brain atlas with accurate brain structures segmented and labeled, including the AD-specific structures. The image processing algorithms extract the brain areas from the neuroimages, detect the landmarks on the images, and segment the AD-specific structures from the images by using the digital AD-specific brain atlas. They are presented chapter by chapter in this thesis. The brain atlas is constructed based on a high resolution magnetic resonance imaging volumetric dataset by using a set of powerful and intelligent tools also presented in this thesis.

The algorithms for automated brain extraction from structural and functional neuroimages are presented in the thesis. They include a domain knowledge based brain extraction algorithm for structural computed tomography images and a rapid cerebral and cerebellar region extraction from functional positron emission tomography (PET) images.

To increase the accuracy of PET images registration into the atlas space by the piecewise linear transformation, a new landmark is defined in this thesis to extend the existing Talairach landmarks, a set of commonly used landmarks in human brain registration, in order to include the cerebellum into the space. The cerebellum is an important brain structure for our research due to its role as an intensity normalization reference. The algorithm for automatic detection of the new landmark as well as the other Talairach landmarks is presented.

According to the linkage between the AD diagnosis and cognitive scores like mini mental state examination, and the correlation between the cognitive scores and the changes of several specific brain structures on the neuroimages, the statistical models of stepwise regressions and discriminant classification are performed on the regions of AD-specific structures to calculate the cognitive scores and classify the experiment subjects into different diagnostic groups automatically. The approach has been applied to hundreds of cases and shown promising results. This is the first effort to quantitatively calculate the cognitive scores by processing the neuroimages automatically. It provides an objective, efficient, less expensive, and extendable way for potential clinical diagnosis in the patients with dementia by the fully automatic computer programs.

List of Figures

List of Tables

Chapter 1

Introduction

This chapter provides a high-level overview of the research topic, a rapid and automatic atlas-assisted cognitive assessment and Alzheimer's disease (AD) diagnosis by making use of neuroimages. It begins with a description of the background, the motivation behind the topic, and the objectives and target of the research. Then, it summarizes my novel research contributions to support the thesis. The chapter ends with a discussion on the organization of the rest of the thesis.

1.1 Rationale and Motivation

The human brain is the most complicated biological organ. Despite the intensive research on the brain, it still remains a great mystery. Neurodegenerative diseases are recognized as a major health problem and are becoming increasingly common at present time, particularly with aging population. The disease is a condition in which cells of the spinal cord or brain are lost and do not readily regenerate [Sigel et al., 2006]. The lost of spinal cells causes the problems with movements, such as ataxia; and the lost of brain cells affects memory and causes dementia. Dementia is a term to describe the symptoms of the illnesses which cause a progressive decline in a person's memory, intellect,

rationality, and social skills. Usually the disease process begins a long period of time before symptoms are present and diagnosis is made. Therefore, early diagnosis of dementia becomes an important task for the patients and their families to plan for the future and educate themselves about the disease, even though there is no cure yet to stop the disease progress.

As a major form of dementia, AD accounts for approximately two thirds of all dementia cases worldwide [Jalbert et al., 2008]. Since Dr Alois Alzheimer, a famous German pathologist, first described the characteristic abnormal brain changes of a patient who had died of an unusual mental illness in 1906, the disease is now known as Alzheimer's disease [Berchtold and Cotman, 1998]. According to the website of World Health Organization (WHO), currently there are about 18 million people worldwide with AD. This figure is projected to nearly double by 2025 to 34 millions due to the aging population. In Australia, this figure is 220,050 people with dementia representing 1.06% of the total population in 2007. By 2030, it will have more than doubled to 465,460 representing 1.88% of the population and by 2050 it will reach 731,030 or 2.77% of the population [Economics, 2005].

Currently, AD can be definitively diagnosed only after death by an examination of brain tissue in an autopsy [Koopman et al., 2009]. For living subjects, the steps in the diagnosis process of AD are 1) medical history assessment, 2) clinical examination, and 3) evaluation of memory and thinking abilities [Petersen, 2009]. The medical history assessment is done by clinicians to ask questions about the person's overall health, past medical problems, ability to carry out daily activities, and changes in behavior and personality. The clinical examination includes the tests of blood, urine, or spinal fluid, and brain scans such as computed tomography (CT), magnetic resonance imaging (MRI),

or positron emission tomography (PET), etc. The memory and thinking evaluation is usually done by some score assessment systems to evaluate the abilities of memory, problem solving, attention, counting, and language [Estrada and Soto, 2009]. Due to the uncertainty and subjective judgments, the patients, who are having memory problems, are diagnosed as "possible AD" if the symptoms may be caused by another disease, or "probable AD" if no other cause for the symptoms can be found [Waldemar et al., 2006]. Since no symptoms are obvious during the early stages of the disease, it is still a challenging task for early diagnosis of this degenerated human brain disease which was found and described more than 100 years ago. However, neuroimaging techniques provide the possibility to investigate the human brains in vivo by a visual inspection or quantitative analysis with computer technologies. Therefore, the early detection of the brain changes in structure or function becomes possible.

The initial motivation of this research was to make use of the neuroimaging techniques as the clinical diagnosis or even prediction of AD by applying computer technologies. Several neuroimaging modalities, such as CT, MRI, and PET, have been developed to study brain anatomy, function, and pathology [Allen et al., 2008; Johansen-Berg, 2009]. They are also available for studying the brain in AD [Jack Jr et al., 2008]. The potential roles of neuroimaging in research for AD include cognitive assessment tool, a prediction of mild cognitive impairment (MCI), early diagnosis of AD, separation of AD from other forms of dementia, monitoring of disease progression, and monitoring response to therapies. Neuroimaging includes structural and functional imaging techniques [Frisoni, 2009]. The structural neuroimaging produces high quality images of brain structure, e.g. CT or MRI. They are recommended for the routine evaluation of AD, or are useful to quantify atrophy of the structures of interest or atrophy of whole brain [Fan et al., 2008]. Because structural changes usually occur late in the progress AD,

functional imaging modalities may have greater potential in detection of the disease earlier [Frisoni, 2009]. PET is one of the most popular scanning techniques in current neurological research to provide functional information about physiological and biochemical processes [Senda et al., 2002]. PET scans allow one to observe blood flow or metabolism in any part of the brain [Grafton et al., 1992; Weber et al., 2000]. The fluoro-deoxy-glucose (FDG) is the most widely used PET tracer in the study of AD. In a FDG-PET scan, the subject is injected with a very small quantity of radioactive glucose. Brain cells use glucose as fuel, and if they are more active, they will consume more of the radioactive glucose, and if less active, they will consume less of it [Habra et al., 2010; Kushner et al., 1987]. A computer uses the absorption data to show the levels of activity as a grey brain map, with one value (usually bright) indicating more active brain areas, and another value (usually dark) indicating less active areas.

1.2 Objectives

Numerous research papers on AD analysis based on neuroimages were published (the literature review is given in Chapter 2). Currently, their findings were discussed and validated at research stage only; the clinical AD diagnosis and assessment is still by the conventional approach, i.e. by medical history assessment and evaluation of memory and thinking abilities. It is a lack of the practical clinical trials of AD diagnosis and assessment based on neuroimaging techniques. Computer-based neuroimage processing is playing a key role in early detection and diagnosis of AD, and the intelligent methods and interactive tools are crucial for reliable medical systems. However, processing of neuroimages is a challenging problem due to 1) complicated brain anatomy and function, 2) a variety of techniques for brain imaging, and 3) numerous algorithms for neuroimage

processing. It is becoming even more difficult in disease due to abundant abnormalities and diseases, and the ways of their depiction in diagnostic imaging. Atlas-assisted brain image processing [Gholipour et al., 2007; Nowinski, 2002] is one of major approaches for medical image analysis, and shows its clinical values in the applications, e.g. stroke detection and diagnosis [Nowinski et al., 2008]. It is a powerful approach to fuse data and synthesize results across subjects, time series of same subject, and even modalities. Since it is automated and repeatable, it would be more reliable and objective than current clinical diagnosis by only medical history assessment and interviews with patients. The use of the atlas allows researchers to compare and contrast these brain images captured from different time series of a patient or from different subjects.

The target of this research is to propose an automated and objective approach for AD or MCI early diagnosis and severity assessment by processing neuroimages and performing statistical analysis, based on a digital brain atlas with labels of AD-specific structures (defined in Chapter 3). Therefore, the new three-dimension (3D) digital atlas is hereby constructed first. It is a powerful tool not only for AD early diagnosis and severity assessment, but also for possible applications such as disease progression monitoring and treatment monitoring. The proposed approach is designed and efficiently implemented based on several dedicated algorithms for analysis of neuroimages with AD and MCI.

1.3 Contributions

To support the thesis that delivers significant value to neuroimages processing and the diagnosis and assessment of AD and MCI, several novel research contributions in this thesis are summarized as follows:

- *Algorithms for automated brain extraction from structural and functional neuroimages* [Qian et al., 2009a; Qian et al., 2009b]

  The algorithm for automated brain extraction from CT images is developed to segment brain areas from CT volumetric data efficiently and accurately. Also, the algorithms for automated brain extraction from PET images and the separation of cerebral hemispheres are developed to obtain the brain areas for further processing such as landmark detection and data transformation.

  Due to the absence of anatomic information and various situations in CT images and low contrast and signal-noise ratio in PET images, algorithms for brain segmentation from those images face the problems of processing time, result accuracy, and user intervention. The algorithms for brain areas extraction presented in this thesis are fast, accurate, and fully automatic without any user intervention.

  The details of the algorithms are proposed in Chapter 5.

- *A set of landmarks is extended to include the cerebellum into the atlas space* [Qian et al., 2010a]

  The new landmark is defined as the cerebellum inferior (CBI), which is at the most inferior point of the cerebellum, to enclose the cerebellum into the Talairach space for a rapid Talairach transformation. After adding the new landmark, the whole brain is subdivided into 18 cuboidal regions including both cerebrum and cerebellum (as opposed to the original 12 cuboids) by 9 landmarks, which are 8 modified Talairach landmarks and CBI as well.

  The landmark of cerebellum is missing from the Talairach landmarks, but it is important for cerebellum extraction from the neuroimages to improve the accuracy

and transformation of neuroimages to Talairach space. A new landmark for cerebellum is introduced based on image processing and brain anatomical knowledge. The details of the new landmark definition are described in Chapter 6.

- *An algorithm for automated landmark detection from PET volumetric data* [Qian et al., 2010a]

  The algorithm detects the modified Talairach landmarks and the extended landmark CBI automatically for the subsequent transformation of PET images into the Talairach space.

  As a new landmark is introduced, a new algorithm for landmark detection on PET images is studied and investigated for the subsequent PET image transformation into Talairach space.

  The details of the algorithm are discussed in Chapter 6.

- *Tools for atlas construction* [Qian et al., 2008]

  This is an interactive platform for brain segmentation and post-processing of segmented results. It is developed with functions for interactive segmentation, contour editing, 2D-3D correlation, marching sulci, and multiple dataset synchronization. A new brain atlas was constructed by making use of these functions. It has the accurate regions including AD firstly affected structures e.g. hippocampus, adjacent structures e.g. temporal gyri, and AD less affected structures e.g. cerebellum. It has 3D labels for all the structures of the brain in a high-resolution volumetric format. The details of the tools are presented in Chapter 4.

- *An assessment method to evaluate and diagnose the experiment subjects* [Qian et al., 2010b]

  This method is based on the extracted regions of interest from PET images as well as the diagnosis information of experiment subjects. The regions are the AD-specific structures. The statistical models of the stepwise linear regression and discriminant classification are performed to generate the regression equations and discriminant functions to evaluate the cognitive severity of the experiment subjects and classify them into normal subjects or patients with AD or MCI. This is the first effort to automatically calculate the cognitive scores by processing the neuroimages and give the promising results.

  The method presents a cognitive assessment approach from neuroimages automatically, instead of manual assessment which is time-consuming, subjective, and costly.

  The details of the method and the results are presented in Chapter 7.

1.4 Thesis Organization

The rest of this thesis is organized as follows.

- Chapter 2 discusses the clinical diagnosis and assessment approaches for AD and MCI and the markers of AD on neuroimages. It also presents the state-of-the-art methods and algorithms popularly used for analysis of AD neuroimages, image processing methods for structural and functional neuroimages, digital brain atlases for different applications, statistical analysis of AD assessment and diagnosis from neuroimages.

- Chapter 3 gives an overview of the proposed research work in this thesis and the materials used in this research. The proposed research work includes the introduction of the components of atlas-based approach, and the implementation of AD assessment from neuroimages. The details of each component are introduced in the subsequent chapters.
- Chapter 4 presents a new brain atlas constructed by a set of interactive and intelligent construction tools.
- Chapter 5 discusses the design and implementation of the automated brain extraction methods from neuroimages including structural CT images and functional PET images.
- Chapter 6 extends the Talairach landmarks to include a new landmark for more accurate transformation of PET images into the standard Talairach space.
- Chapter 7 statistically analyzes the data extracted from the PET images based on the atlas to generate the regression equations and discriminant functions to assess the cognitive scores of experiment subjects and classify them into AD, MCI, and normal groups.
- Finally, Chapter 8 provides the research summary and discusses the directions for future work.

Chapter 2

Related Work and Background

This chapter provides the state-of-the-art literature review of related work, including the clinical assessment and treatment for Alzheimer's disease (AD), roles of structural and functional neuroimaging in AD assessment and diagnosis, digital brain atlases and their applications in neuroimage processing, automated methods of brain extraction from neuroimages, and statistical analysis methods for medical image data processing and AD diagnosis. It ends with a summary of related work.

2.1 Clinical AD Assessment and Treatment

For any disease treatment, early diagnosis is very important. AD is a progressive neurodegenerative disorder associated with slow impairment in cognition, function, and behavior. Pathologically, AD damages large cortical neurons initially in the temporal lobes and later in the remaining neocortex and association areas [Petrella et al., 2003]. Unfortunately, the cause of AD is unknown yet, and there is no single test to identify AD. The diagnosis of AD can only be confirmed by examination of the brain tissue, i.e. by autopsy.

2.1.1 Clinical AD Assessment

The AD progress has a few steps from mild AD to moderate AD and then to severe AD. Usually the early stage of AD is also called mild cognitive impairment (MCI), which is a diagnosis given to those who have cognitive impairments but do not interfere significantly with their daily activities. Currently, the clinical examinations like brain scans or laboratory tests only are the aided approaches to rule out other causes of dementia-like symptoms. The diagnosis of AD in a living subject is made by careful clinical consultations by the dementia severity assessment systems, e.g. mini mental state examination (MMSE) [Folstein et al., 1975] and clinical dementia rating (CDR) [Morris, 1993] (see the appendixes for details).

The MMSE is the most commonly used score system to assess cognitive changes in patients with dementia. The MMSE covers five areas: orientation, registration, attention and calculation, recall, language and praxis. A series of questions and tests are answered by the patients, and then the maximum score of 30 points is given to the correct answers. Table 1 lists the range of scores to assess the cognitive function of a patient. Although it is a simple way to quantify changes in cognitive function and has been translated into many languages, it has several limitations [Crum et al., 1993]: 1) education levels of different patients may affect the scores, 2) it is not sensitive in detecting mild dementia, and 3) abnormalities are not specific for AD or other dementia (refer to Appendix A for more details).

Table 1. Mini mental state examination

MMSE Score	24-30	18-23	0-17
Interpretation	Normal	MCI	AD

The CDR is another scale used to characterize six domains of cognitive and functional performance applicable to AD and related dementias. They are memory, orientation, judgment and problem solving, community affairs, home and hobbies, and personal care. The necessary information to make each rating is obtained through an interview of the patient and/or a family member by filling a CDR table (Table 2) to guide the clinician in making appropriate ratings based on interview data and clinical judgment. In addition to ratings for each domain, an overall CDR score may be calculated [Morris, 1993] through dividing the domains into a primary category (Memory) and the secondary category (other 5 domains). For example, in Table 2, the primary category is 0, and 5 secondary categories are greater than 0, so the global CDR is presented as 0.5 (refer to Appendix B for more details). This global score is useful for characterizing and tracking a patient's level of impairment or dementia.

Table 2. Clinical dementia rating scores based on six domains

	0	0.5	1	2	3
Memory	√				
Orientation		√			
Judgment and Problem Solving			√		
Community Affairs			√		
Home and Hobbies			√		
Personal Care				√	
Global CDR		○			
Interpretation	None	Questionable	Mild	Moderate	Severe

2.1.2 Clinical AD Treatment

Unfortunately, there is no cure for AD at present. The disease cannot be stopped or reversed back by any treatment. The primary goals of treatment for AD are to improve the quality of life for the patients. Typically there are three approaches:

- slowing the progression of cognitive decline and treating specific symptoms with drug therapies. There are some drugs currently being used to temporarily improve mental function and treat secondary symptoms such as depression and anxiety. They cannot stop the disease but can slow the progression of symptoms on some people.
- managing the behavioral symptoms to improve functioning and reduce behavioral problems by non-drug approaches or prescription drugs.
- support and education for the family. It can enable a person with dementia and his/her family to receive help in understanding and adjusting to the disease and to prepare for the future in an appropriate way, including financial and living arrangements and finding aids and services from the communities and learn effective ways of interacting with the person with dementia.

2.2 Roles of Structural Neuroimaging in AD

Brain structures are studied and identified as more-affected or less-affected by AD, by processing and analysis of the neuroimages generated by structural neuroimaging techniques like computed tomography (CT) and magnetic resonance imaging (MRI). This section gives a brief introduction of human brain structures and the atrophies of whole brain or several anatomical brain structures affected by AD.

2.2.1 Human Brain Structure

The human brain is the center of the human nervous system and is a highly complex organ. The human brain has three major structural components: cerebrum, cerebellum, and brainstem shown in Figure 1. The cerebrum is the largest part of the human brain, associated with higher brain function such as thought, action, intelligence, and reasoning.

The cerebral cortex consists of several lobes: the frontal lobe, parietal lobe, occipital lobe, temporal lobe, and insular lobe. The frontal lobe is associated with reasoning, planning, parts of speech, movement, emotions, and problem solving. The parietal lobe is associated with movement, orientation, recognition, perception of stimuli. The occipital lobe is associated with visual processing. The temporal lobe is associated with perception, auditory, memory, and speech. And the insular lobe is a small triangular area on the medial surface of the lateral sulcus; it can be seen in the intact brain only by separating the frontal and parietal lobes from the temporal lobe [Solms and Turnbull, 2002]. The cerebellum, or "little brain", is similar to the cerebrum in that it has two hemispheres and has a highly folded surface or cortex. This structure is associated with regulation and coordination of movement, posture, and balance.

The hippocampus and amygdala are the first affected brain structures inside the cerebrum by AD progress [Braak and Braak, 1991; Minoshima et al., 1997], shown in Figure 2. The hippocampus is a major component of the human brains. It belongs to the limbic system and plays important roles in long-term memory and spatial navigation. Like the cerebral cortex, it is a paired structure located inside the medial temporal lobe, beneath the cortical surface [Amunts et al., 2005]. The amygdala is located deep within the medial temporal lobes of the brain. It is considered part of the limbic system [Amunts

et al., 2005]. The atrophy of whole brain or AD-affected structures including hippocampus and amygdala is an early marker of the disease.

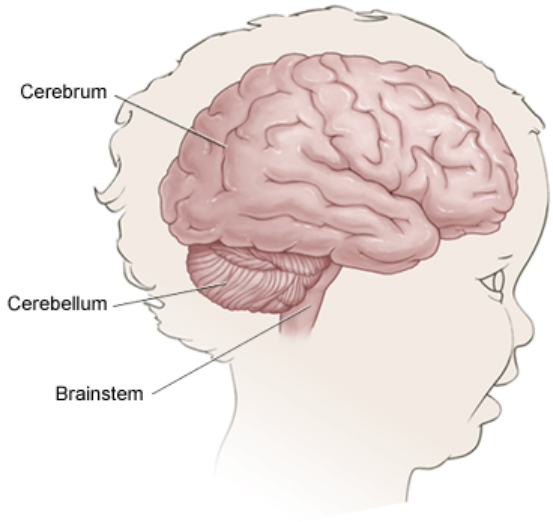

Figure 1. Major parts of human brain
(adapted from the website of Children's Hospital Central California, http://www.childrenscentralcal.org)

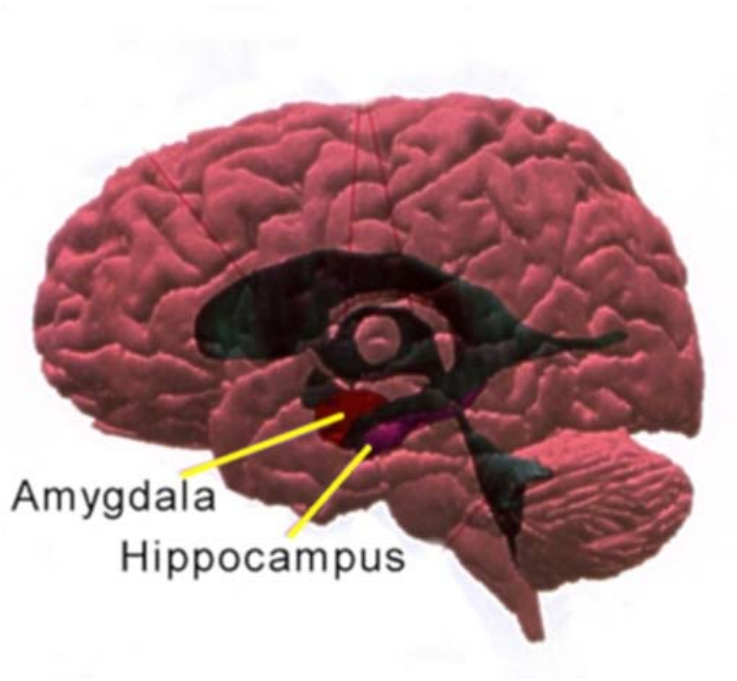

Figure 2. Hippocampus and amygdala
(adapted from the website of Bioasis Technologies Inc, http://blog.bioasis.ca)

2.2.2 Global Brain Atrophy on Structural Neuroimages

Structural neuroimaging such as MRI is a non-invasive technique to render images of brain inside the skull. Measurement of brain atrophy is proposed by various groups as an approach of processing MRI images of AD patients. Atrophy of the brain grey matter was reported as 2.7% per year in AD patients compared to 0.5% in normal aging [Chan et al., 2001]. Another report presented different figures: the annual volume loss of grey matter in normal aging is less than 1% and the rates as high as 4% occur in early AD [Ashburner et al., 2003]. However, global brain atrophy also occurs due to normal aging and lacks the specificity to the disease. Besides global brain atrophy, several brain structures were measured and reported on rate of atrophy too.

2.2.3 AD-affected Structures on Structural Neuroimages

The structures within the medial temporal lobe are the first to be affected by pathology in AD [Braak and Braak, 1991; Minoshima et al., 1997]. They are hippocampus, amygdala, entorhinal cortex, and hippocampal gyrus. The medial temporal lobe atrophy in patients with AD was confirmed by several MRI studies [Frisoni et al., 1999; Henry-Feugeas, 2007; Jack Jr et al., 1997] as well as autopsy-confirmed AD [Whitwell et al., 2008]. Figure 3 shows the cerebral lobes: the frontal lobe, parietal lobe, occipital lobe, and temporal lobe. The temporal lobes are located at the both sides of the cerebrum. Figure 4 shows the temporal lobe which is divided into superior, medial and inferior parts. The red line is the superior temporal sulcus, which divides the superior temporal gyrus (peach) from the middle temporal gyrus (lime). The blue line is the inferior temporal sulcus, which divides the middle temporal gyrus from the inferior temporal gyrus (lavender).

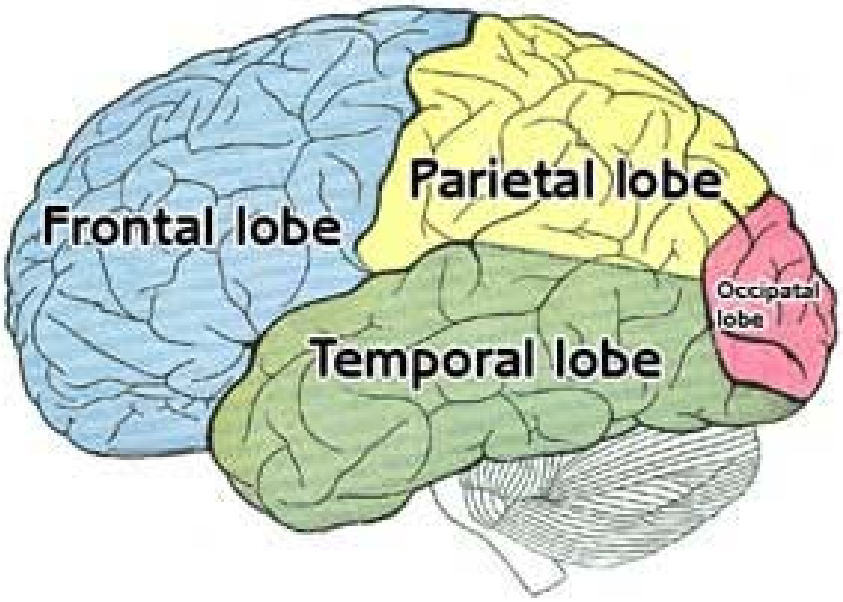

Figure 3. The cerebral lobes

(adapted from the website of Elements4Health, http://www.elements4health.com)

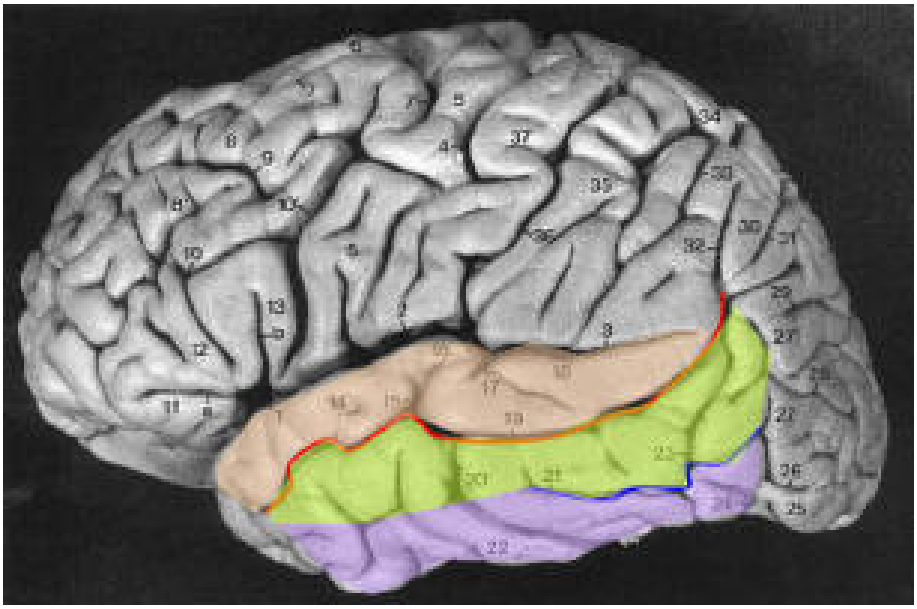

Figure 4. The temporal lobes

Superior (peach), medial (lime), and inferior (lavender) (adapted from the website of fMRI 4 Newbies, http://psychology.uwo.ca/fmri4newbies)

In cross-sectional and longitudinal studies, the hippocampus has shown an increased rate of atrophy in AD patients (4-6% per year) compared to matched control (1-2% per year) [Jack et al., 2000; Jack Jr, 1998; Laakso et al., 2000]. The atrophy of the hippocampus happens early in the development of AD [Chetelat and Baron, 2003; Teipel et al., 2003], and is an early mark present before dementia onset [Fox et al., 1996; Jack et al., 1999; Kaye et al., 1997]. In mild AD, the affected regions spread into the adjacent inferior temporal, and then the prefrontal cortex and other brain regions in later stages of the disease [Minoshima et al., 1997].

2.3 Roles of Functional Neuroimaging in AD

In this section, functional MRI (fMRI) and positron emission tomography (PET) are discussed as well as glucose metabolism reduction and AD imaging with fluoro-deoxy-glucose (FDG) PET.

2.3.1 fMRI and PET

fMRI measures the change in blood flow related to neural activity in the human brain. It is one of the most recently developed forms of neuroimaging [Amaro, 2006]. Since the early 1990s, fMRI has come to dominate the brain mapping field due to its relatively low invasiveness, absence of radiation exposure, and relatively wide availability.

Figure 5 shows an example of fMRI images which are merged with a MRI image (Figure 5a) and a 3D display of a brain surface (Figure 5b). fMRI plays a role of comparing mild AD and healthy elderly with processing of semantic and phonological information [Saykin et al., 1999]. It may also be useful in confirming a memory disorder

diagnosis and detecting individuals with initial dysfunction in learning as a result of AD [Kato et al., 2001]. A fMRI study reported that MCI and AD patients have less medial temporal lobe activation on the memory task than the normal subjects [Townsend and Cherry, 2001].

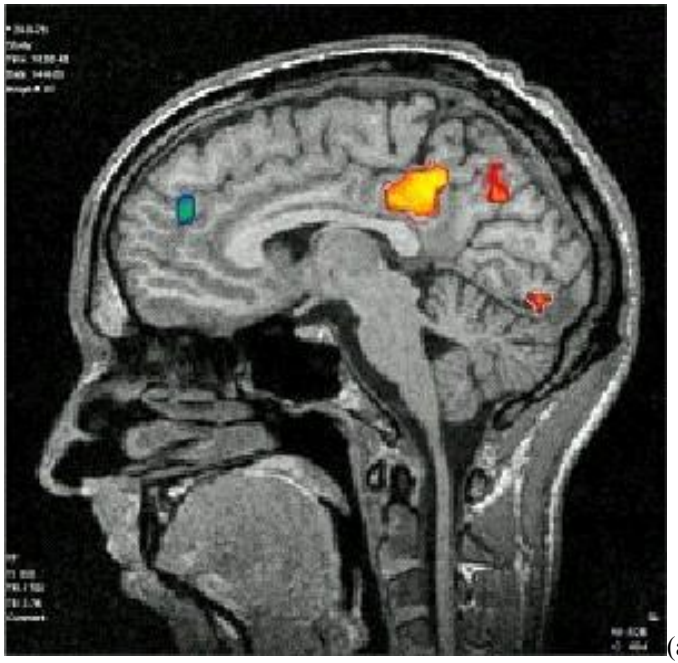

(a)

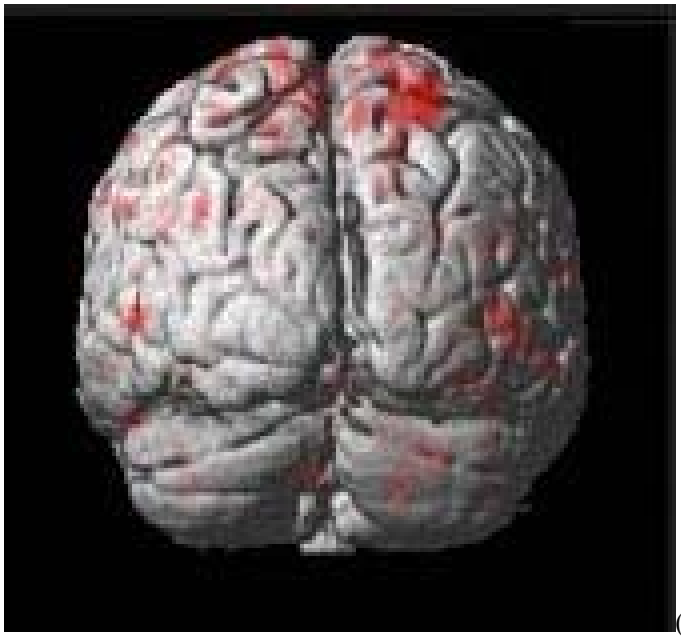

(b)

Figure 5. Functional magnetic resonance imaging
Merged with (a) a MRI image and (b) a 3D display of brain surface

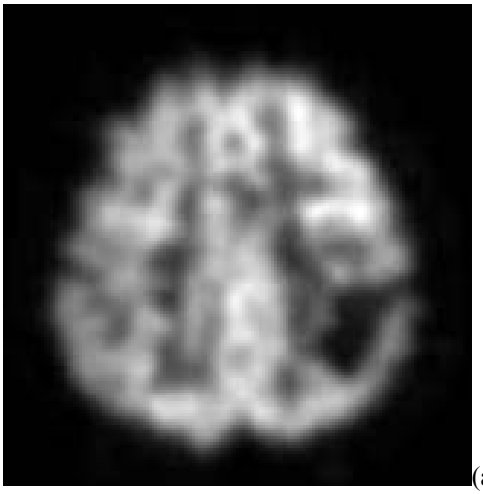

(a)

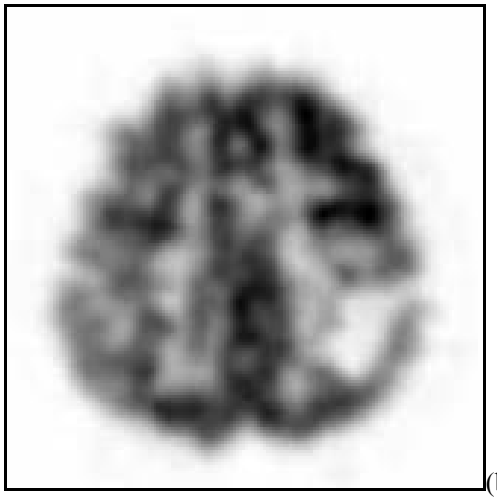

(b)

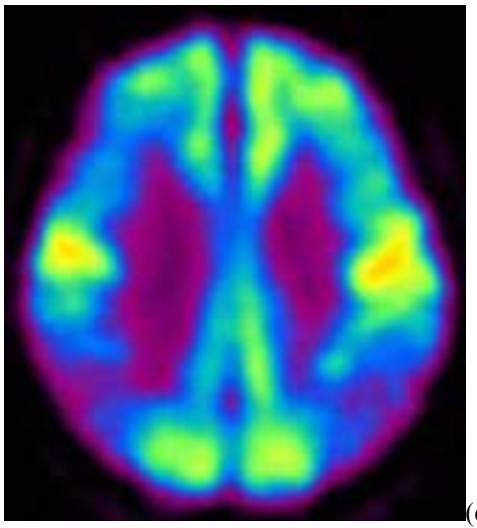

(c)

Figure 6. Positron emission tomography

(a) original image; (b) inversion image; (c) color mapped

PET is a powerful non-invasive tool used to study the biochemistry and physiology of the working brain. It measures the metabolic activity and neurotransmission of nerve cells to produce a three-dimensional (3D) image of functional processes in the brain [Senda et al., 2002]. PET scans provide the images to observe blood flow or metabolism in any part of the brain. The FDG is the most widely used PET tracer in the study of AD.

The FDG-PET neuroimaging and its role in diagnosing AD and MCI, and predicting the progression from MCI to AD have been recently reviewed [Borrie, 2007; Foster et al., 2007; Mosconi, 2005; Petrella et al., 2003; Ryu and Chen, 2008; Zakzanis et al., 2003]. The reviews indicate that FDG-PET becomes a standard technique to measure glucose metabolism within AD-affected areas or within whole brain, and also becomes a tool to evaluate the treatments for patients in neurological diseases. Figure 6 shows an example of glucose metabolism PET image (Figure 6a), its inversion (Figure 6b), and the color mapped image (Figure 6c) for more apparent inspection, respectively. The brain cells give bright value in the image if they are more active and show dark in the image if they are less active shown in Figure 6a.

2.3.2 Glucose Metabolism Reduction in PET

Patients with AD have characteristic reductions in glucose metabolic measurements of regional brain activity, which are progressive and correlate with dementia severity [Mosconi et al., 2007]. The reduced glucose metabolism was found in AD patient FDG-PET images in several areas which are correlated with the AD-affected structures on MRI images. The correlation between severity of cognitive impairment and extent of

hypometabolism was confirmed [Mazziotta et al., 1992]. The neuropathological diagnosis with FDG-PET images is even reported that it is superior to the diagnosis with clinical examination [Foster et al., 2002]. PET scans are abnormal even when symptoms of AD are very mild or even at MCI stage [de Leon et al., 2001; Matsuda, 2007; Minoshima et al., 1997; Silverman et al., 2001]. Thus PET may be useful in early diagnosis of MCI, or differentiating neurological disease from other causes of behavioral and cognitive dysfunction [Gilman et al., 2005; Kerrouche et al., 2006].

FDG-PET provides quantitative estimates of the local cerebral metabolic rate of glucose. There are several studies reported that the glucose hypometabolism of the medial temporal lobe was found from PET [Hunt et al., 2007; Ishii, 1996; Jagust et al., 2006; Jagust et al., 1993], and confirmed in patients with pathologically verified dementia [Hoffman et al., 2000]. A longitudinal study demonstrated that the patients with AD had significantly lower glucose metabolism than healthy comparison subjects in parietal, temporal, occipital, frontal, and posterior cingulate cortices [Alexander, 2002]. Since many reports have given the same conclusions of glucose metabolism reduction in those affected regions from AD patient FDG-PET images, FDG-PET imaging is receiving more and more attention because it may precede structural changes in AD.

2.3.3 FDG-PET Image Processing

The visual inspection of glucose metabolic PET images has to be done by professionals or experts. It is not only time-consuming for numerous cases but also inconsistent and subjective for different investigators. In the past decades, computer technologies were rapidly developed in computing power, imaging technology, and algorithm development. It becomes possible to have automatic or semi-automatic

methods to analyze images in order to reduce the inconsistence by visual inspection and increase the performance.

It is important to establish a standardized workflow for processing and analysis of the imaging data, for example the preprocessing steps to enhance the data include image intensity homogeneity-correction and normalization. Usually computer software needs a few steps to analyze FDG-PET images. They are normalization of images, registration of different cases or modalities, spatial transformation of images into dimensions of a brain template such as the Talairach atlas, segmentation of regions of interest, and analysis of comparing individual images with template images or the baseline state of same subject.

Since PET images lack precise anatomical landmarks because of a low signal-noise rate and low contrasts between anatomical structures, it is usually difficult to identify anatomical regions of interest in PET images. The statistical analysis methods and clustering analysis methods are usually applied for image processing. For FDG-PET images, the calculation of absolute metabolic rates needs blood samples [Takagi et al., 2004]. Its cost is high and its quantification procedure is too complicated. Therefore, a non-invasive analysis method has become a standard approach. It normalizes radioactivity distribution in a region to a reference region (e.g. the cerebellum) or the global brain to avoid the collection of blood samples and complicated calculation.

As neuroimages are typically very large (millions of voxels), the data reduction methods are applied to reduce the computational cost before the statistical analysis. They are roughly divided into two groups: voxel-based methods and region-of-interest (ROI) based methods. The former considers each voxel as a separate entity for statistical analysis, and the latter focuses on particular areas of the brain to summarize the massive amounts of data in an area into a single number for each ROI in the brain, for example,

the average value of all voxels within the region. The most commonly cited software packages for performing voxel-based analysis are the statistical parametric mapping (SPM) [Friston et al., 1995] method and stereotactic surface projections (SSP) method [Ishii et al., 2001].

SPM is open-source software, and is based on MATLAB platform. It is mostly used for analyzing metabolic rates of glucose, and widely applied to PET data and their longitudinal analysis. The software of SPM (http://www.fil.ion.ucl.ac.uk/spm/) has modules of realignment, normalization, smoothing, segmentation, and statistics. The realignment module aligns a time-series of images acquired from the same subject to the first image which is selected as a reference by using a least squares approach and a six parameter spatial transformation (rigid transformation). The normalization module selects template e.g. MNI from Montreal Neurological Institute, to align images to a standard space. The clustering methods are used to segment grey matter, white matter and cerebrospinal fluid from the brain. The statistical module applies hypothesis tests like t-test and F-test.

Figure 7 shows an example of SPM analysis result of neuroimages. Statistical parametric map in three orthogonal projections (sagittal orientation in Figure 7a, coronal orientation in Figure 7b, and axial orientation in Figure 7c) shows voxels where less activities (darker areas) in brain areas. There are many reports which applied SPM software as their research tool for FDG-PET images. For instance, SPM was applied to statistically analyze the predefined regions of interest [Perneczky et al., 2006], to measure the glucose update [Brenner et al., 2005], to visually inspect the glucose metabolic PET images by experts [von Borczyskowski et al., 2006], to test verbal and nonverbal semantic memory in AD patients [Zahn et al., 2004], and to differentiate other dementia

from AD [Okamura et al., 2001]. In addition, the differences between morphologic and functional changes in the same patients with mild AD were investigated by using SPM [Ishii et al., 2005], the monitoring on effects of treatment was determined by SPM [Teipel et al., 2006], and the study to compare the overall glucose metabolism between early onset and late onset AD was also present by using SPM analysis [Kim et al., 2005].

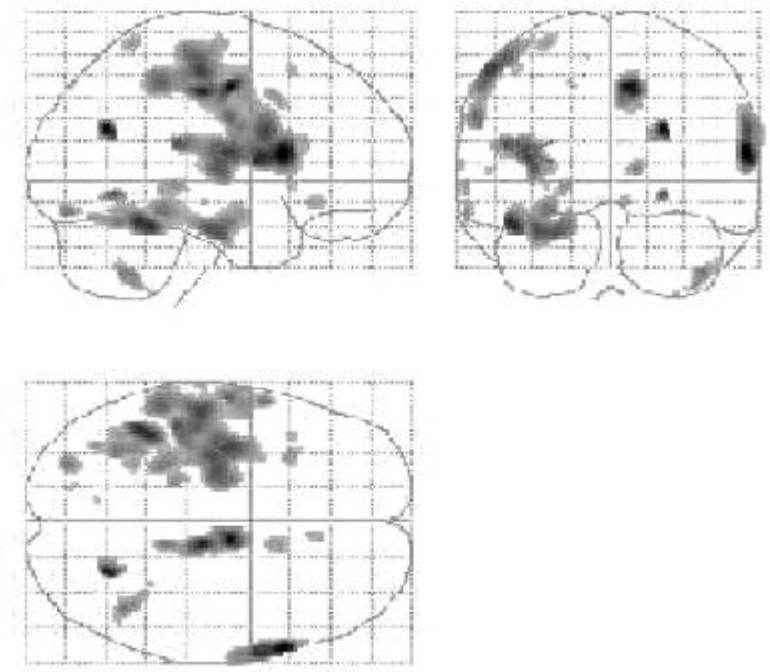

Figure 7. An example of SPM results

SSP is another voxel-based approach highly cited by other researchers in processing of FDG-PET images [Minoshima et al., 1995]. The approach has several steps: 1) analysis of glucose metabolic PET images by using an anatomical transformation to the uniform shape of a standard stereotactic brain template; 2) each image set is realigned to the stereotactic coordinate system first, and then the difference in an individual's brain size is removed by a linear scaling method [Minoshima, 1994]; 3) regional anatomical differences are normalized by a nonlinear warping technique [Minoshima, 1994]; 4)

regional metabolic information was extracted from each image set and then compared to the normal database by means of a z-score on a pixel-by-pixel basis; 5) a normal database was created by averaging extracted datasets of the normal subjects; and 6) any significant metabolic changes are represented in a 3D surface projection view for visual inspections.

Though SSP approach has evidence to be more effective than the standard axial display in FDG-PET images, unfortunately it may not represent subcortical structures as well as white matter. However, it has been successfully applied to improve visual interpretation of PET images [Burdette et al., 1996], to diagnose early onset of mild AD [Ishii et al., 2006], and to differentiate other dementia from AD by analysis of FDG-PET images [Kono et al., 2007].

There are several other approaches mentioned in different reports. A method of dynamic PET images segmentation based on a similarity metric is presented [Brankov and Wernick, 2003], a clustering algorithm depending on the shape of the time signal rather than distance was proposed and compared with other clustering algorithms such as k-means [Johnson and Wichern, 1988] and Gaussian mixture approach [McLachlan and Krishnan, 1997].

Basically the voxel-based approaches such as SPM and SSP typically applied to the applications which need the analysis of whole brain, but they are usually computationally costly in comparing that of ROI-based approaches. It may face difficulties to study accurately small regions such as the hippocampus in atrophic brains. Since the linkage between AD and certain areas of the brain is commonly recognized, the ROI-based methods are more efficient for statistical analysis. They are applied to both structural medical images [Jack et al., 2000] and functional medical images [McColl et al., 1994]. One of the ROI-based methods is atlas-assisted neuroimage processing.

2.4 Talairach Atlas and Landmarks

Atlas-assisted operations on medical images of human brain are widely applied to image segmentation [Carmichael et al., 2005; Lawes et al., 2008], data normalization [Buckner et al., 2004], and localization analysis [Bhanuprakash et al., 2006; Hu et al., 2005b; Nowinski et al., 2008], especially for the PET images with a poorer spatial resolution and lower signal-noise ratio than other modalities like MRI or CT. Numerous printed and electronic brain atlases have been developed [Nowinski, 2001a; Toga et al., 2006]. Talairach and Tournoux introduced a brain atlas [Talairach and Tournoux, 1988], which is commonly used as a reference brain and a gold standard in human brain mapping. Detailed anatomical description including Brodmann's areas provided in this atlas is referred when researchers report the location of brain areas in the stereotactic space. However, the Talairach atlas has several limitations. It has partial inconsistencies between orthogonal plates, variable slice distances, and does not completely represent the in vivo anatomy of subjects.

2.4.1 Talairach Space and Coordinates

The Talairach space is a well-defined common coordinate reference system of human brain. The Talairach coordinate system is used to describe the location of brain structures independent from individual differences in the size and overall shape of the brain. It is defined by a set of landmarks including two subcortical landmarks and six cortical landmarks. Distances in Talairach coordinates are measured from one of the landmarks, the anterior commissure, as origin. Talairach coordinates is that the right hemisphere has positive X values, the anterior part has positive Y values, and the superior part has positive Z values; with the anterior commissure being at coordinate (0, 0, 0).

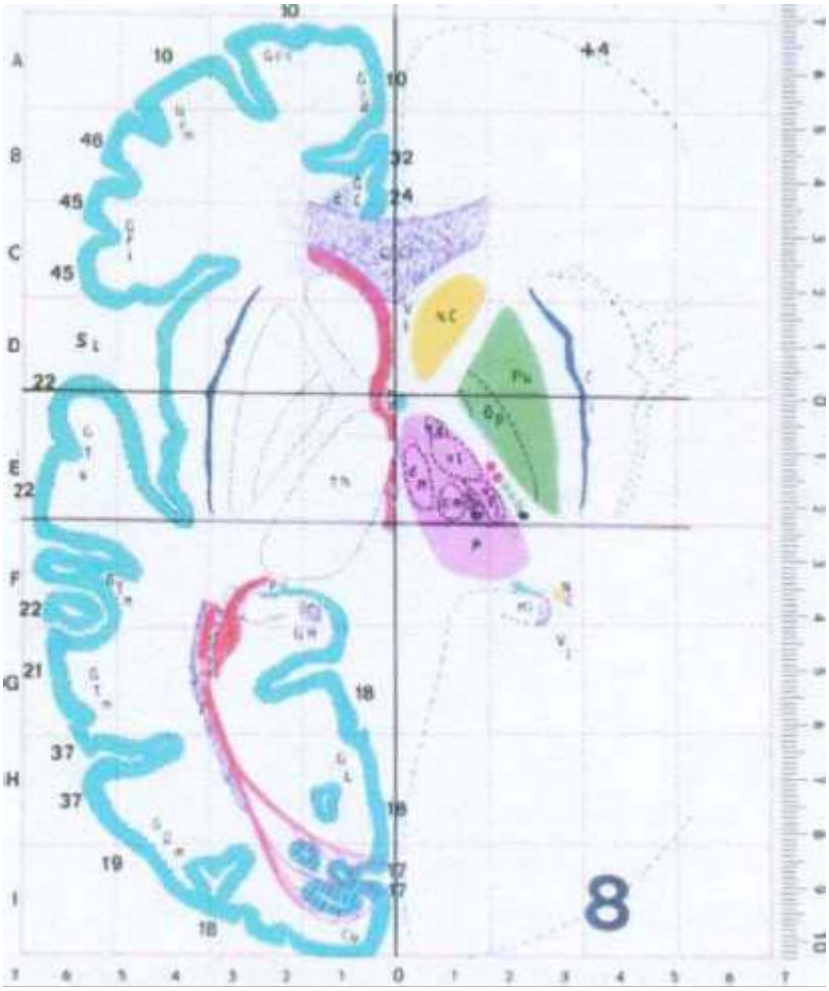

Figure 8. An axial slice of digitized original Talairach atlas

2.4.2 Original Talairach Landmarks

The original Talairach landmarks contain two subcortical landmarks (internal landmarks): anterior commissure (AC) and posterior commissure (PC), and six cortical landmarks (external landmarks): left (L), right (R), anterior (A), posterior (P), superior (S), and inferior (I) [Talairach and Tournoux, 1988]. AC is the point of intersection of the lines passing through the superior edge of the anterior commissure and the posterior edge of the anterior commissure. PC is the point of intersection of the lines passing through the inferior edge of the posterior commissure and the anterior edge of the posterior

commissure. The external landmarks are the points on the cortex. They are: the most superior point of the parietal cortex (S) and the most inferior point of the temporal cortex (I); the most anterior point of the frontal cortex (A) and the most posterior point of the occipital cortex (P); the most lateral points (left and right) of the parietotemporal cortex (L and R). Each cortical landmark is identified by three coordinates on axial, coronal and sagittal orientations. Figure 8 shows an axial slice of the digitized original Talairach atlas.

2.4.3 Modified Talairach Landmarks

The original Talairach landmarks have some limitations and several problems. For examples, the original brain atlas does not contain all of the landmarks, inconsistency of the landmark definitions and their locations in the atlas, AC and PC are located beyond their own structures. In addition, the cortical landmarks are not defined in a constructive way. A set of modified Talairach landmarks, conceptually equivalent to the original Talairach landmarks, was introduced [Nowinski, 2001b] to overcome the problems and become more constructive by computer program. The modified Talairach landmarks are automatically identified on magnetic resonance neuroimages [Bhanuprakash et al., 2006; Hu et al., 2005b], and applied to the Talairach transformation and other atlas-assisted automatic interpretations and applications [Hu et al., 2005b; Nowinski et al., 2008].

The modified Talairach landmarks define the AC and PC within the midsagittal plane (MSP), and are the central points of the anterior commissure and posterior commissure respectively. The landmarks A, P, L and R are identified from the AC-PC plane passing through both the AC and PC; the landmark I is identified on a coronal plane passing through AC (VAC); and the landmark S is identified on another coronal plane passing through PC (VPC). The whole brain is subdivided into 12 cuboids. Figure 9 gives the

modified Talairach landmarks on axial (Figure 9a), coronal (Figure 9b), and sagittal (Figure 9c) MRI images. However, the cerebellum is not included into the modified Talairach landmarks.

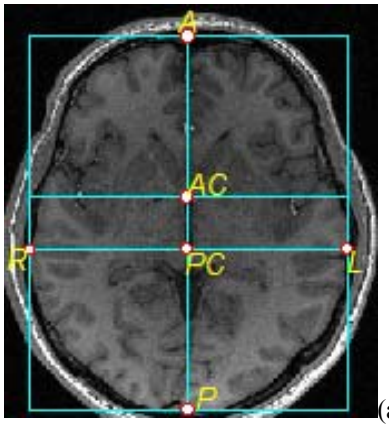

(a)

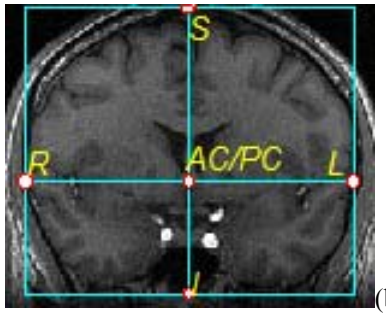

(b)

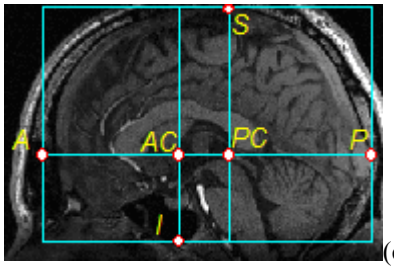

(c)

Figure 9. Modified Talairach landmarks

The landmarks on (a) axial, (b) coronal, and (c) sagittal orientations

2.5 Automated Brain Extraction Methods

Brain extraction from neuroimages is a crucial component in neuroimage analysis systems and medical imaging applications. It is usually a first and essential step to subsequent image processing and further analysis, such as visualization of brain cortex, registration with other neuroimages, further segmentation of brain structures, and morphometry. Segmentation methods are highly dependent on image acquisition modality. This section discusses the state-of-the-art methods and algorithms of brain extraction from CT, MRI and PET neuroimages.

2.5.1 Brain Extraction from CT Neuroimages

Besides the intensity thresholding, which is often used as an initial step of image processing operations [Pham et al., 2000], the segmentation methods of CT images include region growing [Mulenbruch et al., 2006; Pohle and Toennies, 2001; Sandor et al., 1991], model-based active contour [Chertkow and Black, 2007; Luo, 2006; Pardo et al., 1997], combination of statistical clustering and model-based segmentation [Lei and Sewchand, 1992], watershed transformation [Wegner et al.], atlas-based segmentation [Ding et al., 2005], machine learning-based approach [Akselrod-Ballin et al.], and knowledge-based segmentation [Brown et al., 2000; Sonka et al., 1994]. A comparison of different techniques using wavelet, ridgelet, etc. in CT images is available [Dettori and Semler, 2007].

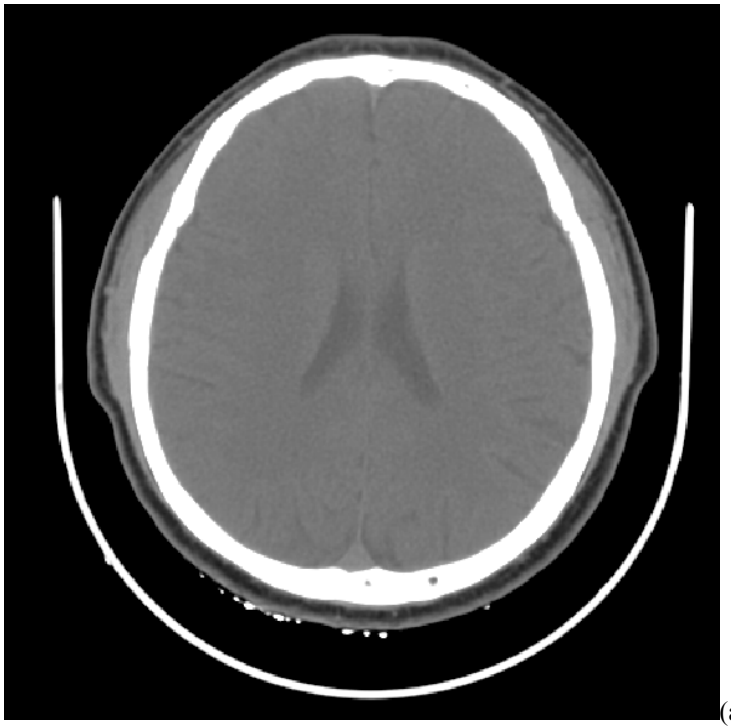

(a)

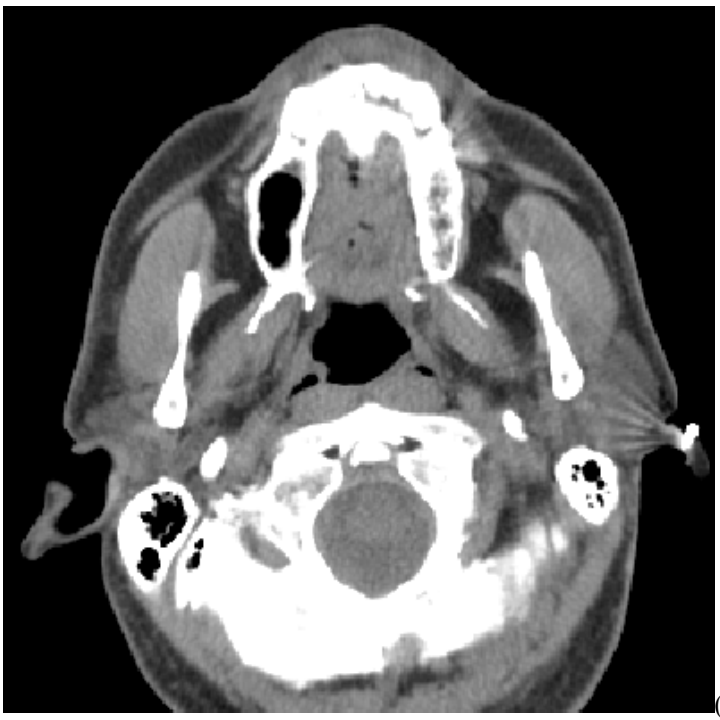

(b)

Figure 10. Examples of CT images

(a) a superior slice; (b) an inferior slice

For CT head images, most of the above mentioned segmentation methods are also applicable. Region growing [Sandor et al., 1991] works fine for the superior (dorsal) slices which usually have a closed bright area on two-dimension slice CT images, see Figure 10a. However, for the most inferior slices, as shown in Figure 10b, the method could face difficulty in choosing the seed point automatically and grow outside the crania. Contour extraction [Soltanian-Zadeh and Windham, 1997] requires user interaction to specify the threshold at different regions. Fuzzy C-means clustering [Hu et al., 2005a] needs several initial parameters, e.g., the number of clusters. The rule-based approach [Matesin et al., 2001] requires prior knowledge and is time consuming. The combination of K-mean clustering, feature extraction, and neural network classification [Loncaric and Kovacevic, 1997] resulted in a complex and difficult to use system.

2.5.2 Brain Extraction from MRI Neuroimages

MRI images provide more detailed information of anatomic structures, e.g. cortical gyri and sulci, than CT. However, it may be more difficult for MRI scans to be accurately segmented than CT scans. There are a number of methods for brain extraction from MRI proposed over a few past decades. These methods include histogram-based thresholding and morphological operations [Shan et al., 2002; Stokking et al., 2000], connected component analysis [Lemieux et al., 1999], region growing and edge detection [Xuan et al., 1995], atlas-guided brain structure identification [Akselrod-Ballin et al., 2006], model-based or knowledge-guided active contour method [Shan et al., 2005], automatic and adaptive brain morphometry [Hu et al., 2008], and hybrid models [Boesen et al., 2004; Chupin et al., 2007]. In the scientific community, there are several downloadable highly

cited software packages for brain extraction and further segmentation of brain structures. They are:

- FMRIB software library (FSL) - a library of analysis tools for neuroimages [Jack et al., 2004]
- BrainSuite - a MR image analysis tool [Shattuck and Leahy, 2002]
- Statistical parametric mapping (SPM) - a software toolkit for the analysis of neuroimages [Friston et al., 1995]
- FreeSurfer - a set of tools for subcortical segmentation, reconstruction of the cortical surface and overlay of functional data onto the reconstructed surface [Dale et al., 1999].

To evaluate the methods of automated brain extraction, above four software packages were downloaded and executed. Table 3 lists these packages with related information such as version, web address to download, the tested components with parameters, and the execution time. *FSL* was running under free software *WMware Player* available at *http://www.vmware.com/products/player/*. The player is a virtual machine on Windows operating system. *SPM* is running with *MATLAB*, a numerical computing environment and programming language.

Currently the most automated methods reported their accuracy by comparison of segmented results with some ground truth. This is done by pixel-by-pixel comparison without applying any anatomical knowledge. Therefore, if the ground truth is only visually correct in images but not anatomically correct by knowledge, the comparison may only make sense in pure image processing terms. Besides, in some software packages it is difficult to check the segmentation quality without mapping it to the origin, e.g. in *FreeSurfer*.

Table 3. Automated methods evaluation

	Software	Version & URL	Tested Components	Parameters	Execution Time
1	FMRIB software library (FSL)	Version 4.0 www.fmrib.ox.ac.uk	- BET (brain extraction tool) - FAST (automated segmentation tool)	- f = 0.5 - g = 0 - type = T1	7 mins
2	BrainSuite	Version 2.0 brainsuite.usc.edu	- BSE (skull stripping) - BFC (non-uniformity correction) - PVC (tissue classification)	- Erosion Size = 2	3 mins
3	Statistical parametric mapping (SPM)	Version SPM5 www.fil.ion.ucl.ac.uk	- Segment under 'Spatial Pre-processing' (brain segmentation)	- CSF= Native Space	22 mins
4	FreeSurfer	Version 4.2.0 surfer.nmr.mgh.harvard .edu	- Preprocessing and skull stripping - Brain structure segmentation and surface generation	- autorecon1 - autorecon2	15 hours

There are a few reviews [Boesen et al., 2004; Klauschen et al., 2009] attempting to evaluate these software packages by measurement of segmented whole brains or brain structures and comparison with ground truth or gold standard. The selected data consisted of simulated datasets and some of real cases. BrainWeb [Cocosco et al.], an online interface to a 3D MR image simulated brain database which is available at http://www.bic.mni.mcgill.ca/brainweb, is widely selected to play such a role in providing different datasets with variations of parameters (e.g. noise level, slice thickness,

etc.), as well as the anatomical model (phantom). Another widely used online database is Internet Brain Segmentation Repository (IBSR) which is available at http://www.cma.mgh.harvard.edu/ibsr. IBSR provides manually guided expert segmentation results on simulated and real data for evaluation and development of segmentation methods.

2.5.3 Brain Extraction from PET Neuroimages

Due to a poor spatial resolution and a low signal-noise ratio of the PET images, automated brain extraction from those images is a challenging task. There are a few registration tools such as Analyze [Robb et al., 1990] and SPM [Friston et al., 1995], which include the components of brain extraction from PET images. They are applied to extract physiological information from PET images by registration with a brain template or another structural modality (e.g. MRI) which has anatomical information to be used as a reference. These tools need the user to load images and perform several steps on them for registration. There are also a few automated or semi-automated methods of brain extraction from PET images including thresholding [Mykkanen et al., 2000] that needs user interventions, cluster analysis and pattern classification methods [Koivistoinen et al., 2004; Wong et al., 2002] which usually need input parameters.

2.6 Statistical Analysis in AD Diagnosis

The statistical analysis has been used in several neurological diseases such as emotion disorder [Kober et al., 2008] and anxiety-related disorder [Etkin and Wager, 2007]. In addition, it was performed to analyze the relationship between the AD diagnosis and the different score systems like MMSE and intelligence quotient [Kawano et al., 2000], the

relationship between the cognitive function and regional cerebral flow [Ushijima et al., 2002], and the correlations between cerebral glucose metabolism and neuropsychological test [Lockwood et al., 2002]. However, the statistical analysis with different statistical models such as correlation test, regression analysis, neural network, and several classification methods, was often used to discover or verify the relationships or correlations between the cognitive scores and the changes detected from the neuroimages.

The current clinical criterions only have a high sensitivity and specificity for AD diagnosis at middle or late stages of the disease [Petrella et al., 2003]. Thus, the new diagnosis of AD in patients with dementia at early stage of the disease becomes a challenging task and research topic for many researchers. This section focuses on the methods of early diagnosis of AD or MCI by the statistical analysis based on the results of neuroimage processing.

The reviews of structural and functional neuroimaging roles in the diagnosis of AD can be found at [Chetelat and Baron, 2003] and [Borrie, 2007], respectively. PET is currently used as an assisting tool to clinical diagnosis, especially in differentiating AD from vascular dementia and other dementias such as frontal lobe dementia. The growing evidence has shown that PET would likely come to the forefront both as a diagnostic tool and as a prognostic tool [Frisoni, 2009; Petrella et al., 2003]. However, MRI is still the favorites of many researchers.

The statistical models of *t* test, bootstrap procedure were applied on the hippocampus for group analysis and individual analysis, after the hippocampi were segmented automatically from the MRI images [Colliot et al., 2008]. Group differences in hippocampal volume were assessed by using *t* test, and bootstrap methods were used to obtain estimates of *p* values, the classification rate, sensitivity, and specificity. A *p* value

of less than 0.05 was considered as an indication of a significant difference. Each participant was assigned to the closest group by comparing the mean values of the groups and the participant. The results of the study gave 84% classification rate between the AD patients and normal controls, and 69% between the patients of AD and MCI. However, they require confirmation with larger groups of participants.

Another method to identify individuals with MCI and AD from MRI images was presented by [Desikan et al., 2009]. Baseline volumetric T1-weighted MRI scans were examined using automated software tools to identify the volume and mean thickness of neuroanatomic regions. All MRI scans were processed using the FreeSurfer software package, and the neocortex of the brain on the MRI scans was then automatically subdivided into the regions of interest including the amygdala and hippocampus. The statistical analysis such as the logistic regressions was applied on the training data for entorhinal cortex thickness and volume. The study showed the results that the MMSE scores correlated with severity of atrophy and the extent of atrophy.

A method of cortical thickness measurement from MR images as well as statistical analysis was proposed for early diagnosis of AD [Querbes et al., 2009]. The mean cortical thicknesses were compared between diagnosis groups of healthy controls, progressive MCI, stable MCI, and AD by a multiple analysis of covariance. A normalized thickness index was defined to be the prediction of the clinical diagnosis outcome. It distinguished stable MCI from progressive MCI, and predicted amnestic MCI to AD and compared it to the predictive values of the main cognitive scores at baseline.

PET images were reported to differentiate AD from dementia with Lewy bodies [Gilman et al., 2005; Kono et al., 2007] and vascular dementia [Kerrouche et al., 2006]. Most of the papers have proposed the methods and algorithms to verify the correlations

between the cognitive severity and the structural or functional changes detected from the neuroimages. The cognitive scores such MMSE or CDR are widely used in clinical practice for the diagnosis of AD and MCI. The correlation of MMSE scores with brain structural changes have been reported in the literature. For examples, the high correlation in AD between MMSE scores and changes in temporal lobes was reported [Thompson et al., 2004]. [Duan et al., 2006] showed high correlation between cognitive impairment and selective white matter damage in AD, measured as a reduction of fractional anisotropy, particularly in the splenium of the corpus callosum. [Apostolova et al., 2006] investigated the correlation between MMSE scores and hippocampal volume changes. [Baxter et al., 2006] showed high correlation in AD between MMSE scores and decrease of grey matter in the left temporal lobe. A strong correlation between MMSE scores and grey matter loss in several cortical regions was observed in clinical and pre-clinical AD [Apostolova et al., 2006].

Cognitive scores are playing very important roles in the correlation with the changes of anatomical structures and functional regions, and diagnosis of dementia as well. However, so far there is still no quantitative assessment of cognitive scores based on the changes detected from the neuroimages.

2.7 Summary

Currently, clinical AD assessment and diagnosis in a living subject is based on medical history assessment and careful clinical consultations by the dementia severity assessment score systems. It is inefficient, inaccurate, and subjective. Usually the most commonly recognized symptom of AD is memory loss, such as difficulty in remembering what recently happened or learned. These earliest observable symptoms are often

mistakenly related to aging or stress. When the symptoms are more obvious and serious, such as difficulties with language or daily activities, the patients have missed their early diagnosis of the disease.

Neuroimaging provides the opportunities to assist cognitive assessment and AD diagnosis to be more objective and less costly. Structural and functional neuroimaging techniques become increasingly important parts in AD research, and perhaps in the near future will become a tool for AD clinical diagnosis. Currently, the structural neuroimages like CT and MRI are useful materials for brain atrophy detection and analysis of AD-specific structures. However, brain structure change or atrophy may only be detected when the cells of the structure are damaged, or the dementia symptoms are obvious. That means the early assessment and diagnosis of AD needs another tool which is more sensitive to the patients at the initial stage, i.e. before the brain structure change and clinical symptoms.

Unlike structural neuroimages, the functional neuroimages like FDG-PET show the glucose consumption change of the brain cells of the patients at the very initial stages of AD. They are becoming the standard imaging technique to detect and assess AD and MCI. However, visual inspection of PET images is a time-consuming task, and inconsistent and subjective as well. Automatic processing of PET images becomes a new challenging task due to the lower image resolution and lower signal-noise ratio of PET images than that of CT or MRI. The edges of a structure are usually not clear or even not visible on FDG-PET images. Therefore, a structural template or atlas with structural information is becoming a key role for the segmentation of PET images. Despite of numerous printed and digital brain atlases, the Talairach atlas is the gold standard in human brain mapping as a reference brain.

The cognitive severity score values such as MMSE are highly correlated with the changes of several structural areas and functional regions. However, quantitative assessment of the cognitive scores based on the changes detected from the neuroimages is still absent. A rapid and automatic atlas-based approach of AD assessment and diagnosis by processing PET neuroimages and performing statistical analysis is presented in the next chapter.

Chapter 3

Proposed Methodology

This chapter gives an overview of the proposed methodology in this thesis, including the components of the atlas-based approach for cognitive assessment and Alzheimer's disease (AD) diagnosis from positron emission tomography (PET) images and their relationships, the definition of AD-specific structures, and the materials used in this research work.

3.1 Components of Atlas-based Approach

Atlas-assisted operations on medical images of human brain are widely applied in segmentation, registration, data normalization, etc. In order to assist AD assessment and diagnosis, the atlas must have the following features: 1) the atlas images have high resolutions at all three orientations; 2) the AD-specific structures are accurately segmented and labeled; and 3) the standard space for spatial normalization of PET images is defined.

Thus, the first step of the proposed method is to define the AD-specific structures based on the literature, followed by the construction of a new brain atlas with those structures accurately segmented and labeled. The glucose metabolism information is extracted from the fluoro-deoxy-glucose (FDG) PET images by two different types of normalization: spatial normalization and intensity normalization. The former is to transform the images to the common atlas space by several steps of image processing, and the latter is to adjust the range of intensity values by dividing the value with that of the less-affected area by the disease. The statistical analysis is finally performed to assess the cognitive scores and make a diagnosis for each of the experiment subjects.

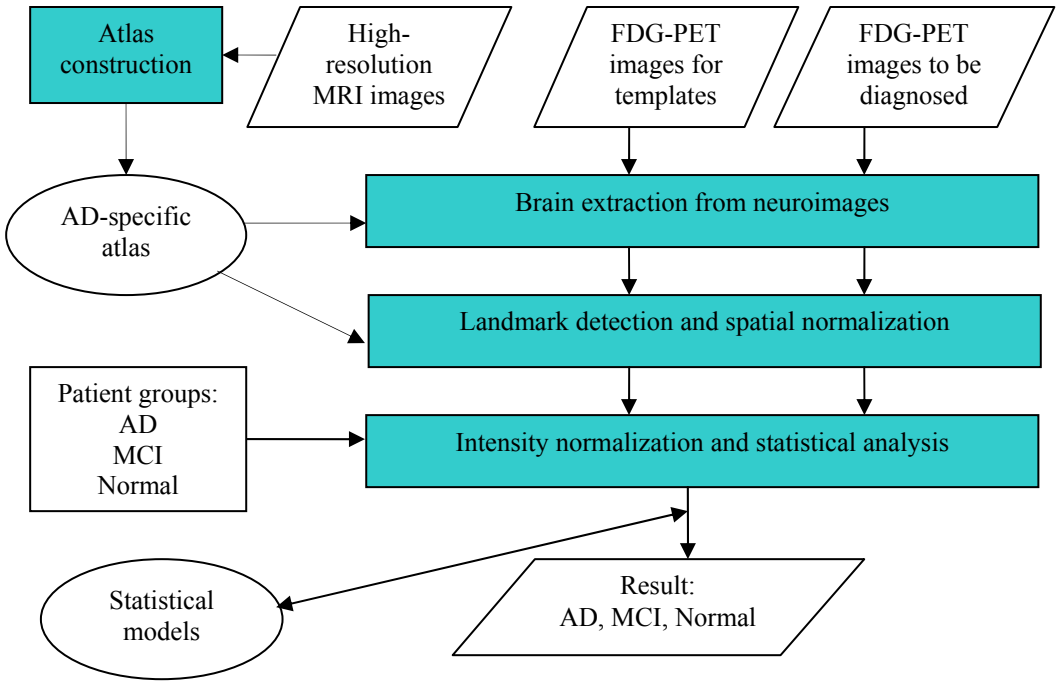

Figure 11. Flowchart of AD assessment from neuroimages
Four components are highlighted: atlas construction, brain extraction, landmark detection and spatial normalization, and intensity normalization and statistical anslysis

Figure 11 shows a flowchart of the implementation and highlights the components of the AD assessment from neuroimages. Four components are designed and implemented: 1) atlas construction, 2) brain extraction, 3) landmark detection and spatial normalization, and 4) intensity normalization and statistical analysis. All image processing algorithms were implemented in C++ programming language, and the statistical analysis was performed by Statistical Package for Social Sciences (SPSS) software.

3.1.1 Atlas Construction

To construct a digital structural brain atlas from a magnetic resonance imaging (MRI) dataset, basically there are two ways: 1) automatic generation by automated or semi-automated computer algorithms and 2) manual generation by interactive editing tools. Currently, the automated methods discussed in Chapter 2, only give the results visually alright, but incomplete or anatomically incorrect (Chapter 4 gives the examples). In this research work, a post-processing platform is developed to assist the neuroanatomy expert in accurate brain segmentation. The platform provides a set of interactive and intelligent tools to allow the user to generate high quality, accurate and correct brain volumes. It takes a high-resolution isotropic MRI volumetric scan as its input to construct a digital brain atlas with brain structures segmented and labeled accurately. The platform with several editing tools is developed with functions for interactive segmentation, contour editing, 2D-3D correlation, marching sulci, and multiple dataset synchronization. It plays an indispensable role in accurate brain extraction from volumetric MR neuroimages due to the partial volume effect, artifacts, noise, and intensity inhomogeneity. It is a useful aid for neuroanatomy experts and clinicians. Figure 12 shows an example of an original axial slice and its segmented image by the presented tool. The details of atlas construction are given in Chapter 4.

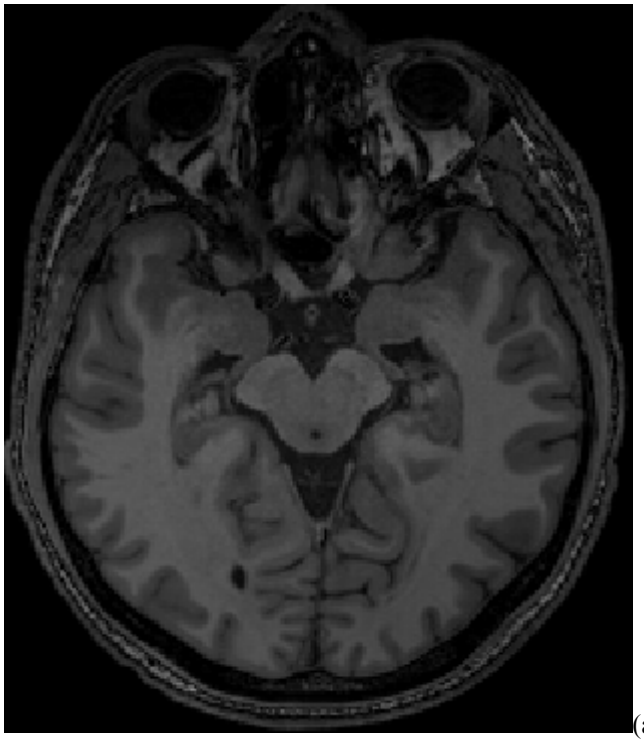

(a)

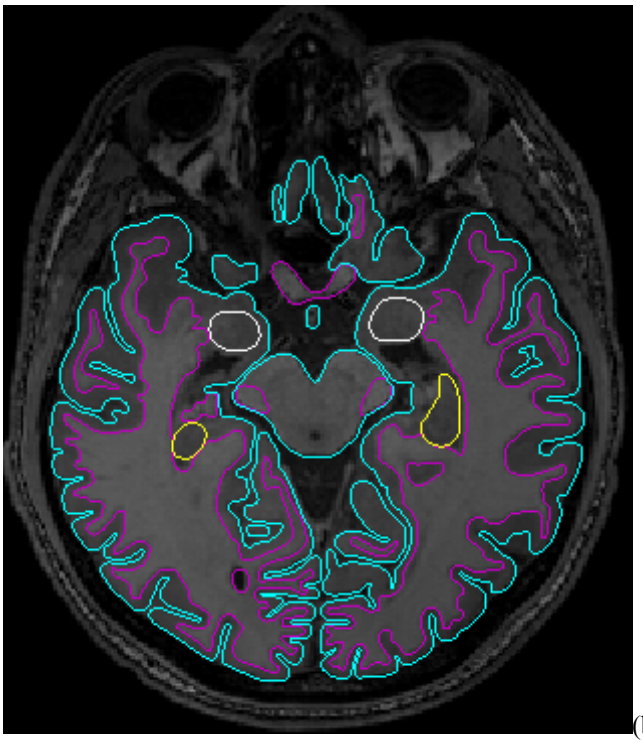

(b)

Figure 12. An example of an axial slice and its segmented result

(a) original axial slice; (b) segmentation results

3.1.2 Brain Extraction

Brain extraction is a kind of segmentation of brain areas from the whole brain volumetric images. It can be done automatically, semi-automatically, or interactively. In this thesis, the wording "brain extraction" is referred to the automated methods introduced by other researchers for comparisons and interactive method on proposed platform in Chapter 4, and to the proposed automated methods in Chapter 5.

An automated approach is presented to extract brain areas efficiently from volumetric FDG-PET scans. A threshold value is automatically calculated from the histogram graph of the brain images, followed by region growing and morphological operations to segment brain areas from these images. The approach is fully automatic (without any user intervention), efficient, and accurate. The details of the algorithm are discussed in Chapter 5.

3.1.3 Landmark Detection and Spatial Normalization

This component is to identify the landmarks including the midsagittal plane of brain, cortical bounding box, anterior and posterior commissure positions, and the most inferior position of cerebellum. Then, it transforms the PET images into the atlas space based on the detected landmarks.

A set of the Talairach landmarks is extended to include the cerebellum into the atlas space by defining the landmark of cerebellum inferior. The method, which was earlier successfully applied to extract the midsagittal plane from MR images, is extended to locate the midsagittal lines (MSL) on the axial slices of FDG-PET images. Based on MSL, the modified Talairach landmarks and cerebellum inferior are identified.

Spatial normalization is actually a registration step to warp the PET images into a standard atlas space for further analysis. There are four steps to do this by: 1) defining the landmarks in the atlas space; 2) extracting the brain from PET images automatically; 3) identifying the landmarks in the PET images automatically; and 4) transforming the PET images into the atlas space. Therefore, the brain structures from different patients are deformed to the same space by piecewise linear transformation based on the landmarks defined in the atlas space and automatically identified in the PET images. The details of landmark definition in the atlas space and landmark detection in PET images are given in Chapters 6.

3.1.4 Intensity Normalization and Statistical Analysis

Due to the variation of image scanning with different scanners and different parameters, the image intensities need to be normalized before performing the statistical analysis. Since the cerebellum is well preserved in AD, it is selected as the reference region to normalize the other areas. In addition, to reduce the partial volume effect of the connected areas of different brain structures, the pixels with the highest intensity values and the lowest intensity values are excluded to calculate the average intensity. The details of intensity normalization and calculation of average intensities are given in Chapter 7.

After normalizing the intensity values of AD-specific structures to the cerebellum for each case, this statistical analysis component consists of two parts: 1) statistical analysis with the models of stepwise regressions for cognitive assessment and discriminant classification for AD diagnosis; 2) verification of the regression equations and discriminant functions by calculating the diagnosis accuracy. The normalized average intensity values of AD-specific structures as well as the dementia severity assessment

scores like the mini mental state examination (MMSE) and clinical dementia rating (CDR) are applied to the above-mentioned statistical models to obtain the assessment scores and diagnosis result for each experiment subject. The details of the statistical analysis are given in Chapter 7.

3.2 AD-specific Structures

Table 4. AD-specific structures

Types	Structure Names	Short Names
Most-affected (C1)	hippocampus	HC
	amygdala	AM
	interior temporal gyrus	ITG
	middle temporal gyrus	MTG
	superior temporal gyrus	STG
Adjacent (C2)	angular gyrus	AG
	fusiform gyrus	FG
	insular lobe	IL
	putamen	PU
	globus pallidus lateral	GPL
	globus pallidus medial	GPM
	parahippocampal gyrus	PG
	supramarginal gyrus	SG
	thalamus	TH
Less-affected (C3)	cerebellum	CB

Based on the state-of-the-art literature discussed in Chapter 2, fifteen anatomical brain regions are selected as AD-specific structures shown in Table 4. They are divided in three different categories: C1) the most-affected structures, C2) the adjacent structures of C1, and C3) the less-affected structure by AD. Patients with AD may have characteristic

reductions in glucose metabolic measurements in the structures of C1 and C2, while C3 structure is the reference for intensity normalization.

3.3 Materials

The FDG-PET images used in this thesis are obtained from a website (www.loni.ucla.edu/ADNI) of Alzheimer's Disease Neuroimaging Initiative (ADNI) database. The below language is given by ADNI, according to the *Data Use Agreement* with ADNI.

"Data used in the preparation of this article were obtained from the Alzheimer's Disease Neuroimaging Initiative (ADNI) database (www.loni.ucla.edu\ADNI). The ADNI was launched in 2003 by the National Institute on Aging (NIA), the National Institute of Biomedical Imaging and Bioengineering (NIBIB), the Food and Drug Administration (FDA), private pharmaceutical companies and non-profit organizations, as a $60 million, 5-year public-private partnership. The primary goal of ADNI has been to test whether serial magnetic resonance imaging (MRI), positron emission tomography (PET), other biological markers, and clinical and neuropsychological assessment can be combined to measure the progression of mild cognitive impairment (MCI) and early Alzheimer's disease (AD). Determination of sensitive and specific markers of very early AD progression is intended to aid researchers and clinicians to develop new treatments and monitor their effectiveness, as well as lessen the time and cost of clinical trials."

The database collects the images from hundreds of subjects who are diagnosed as AD, mild cognitive impairment (MCI), and normal cognitive elders. All PET scans available at ADNI are acquired using one of three different protocols: 1) dynamic: a 30 minute, six

frame acquisition (6 five-minute frames), with scanning from 30 to 60 min post-FDG injection; 2) static: a single-frame 30 min acquisition with scanning 30-60 min post-injection (for Siemens PET/CT scanners that do not have dynamic scan acquisition capability); and 3) quantitative: a 60 min dynamic protocol consisting of 33 frames, with scanning beginning at injection and continuing for 60 min that can be used to compute absolute glucose metabolic rate. Since the majority of the scans in the ADNI study were acquired with the first acquisition protocol, the experiment cases in this research were scanned with the dynamic protocol. They were preprocessed by registration (the subsequent 5 frames are co-registered to the first frame), averaging of 6 frames, and transformation into a grid of 160×160×96 voxels with size 1.5×1.5×1.5 mm^3. The preprocessed images have their horizontal axis paralleled with the anterior commissure and posterior commissure [Langbaum et al., 2009].

Figure 13 shows the examples of images from a patient with MCI. Figure 13a is one slice of the original baseline images; Figure 13b is another original image co-registered with the baseline images; Figure 13c is an averaged image of 6 dynamic scans; and Figure 13d is a slice after reorientation.

A total of 400 experiment subjects were downloaded from the ADNI website. They were clinically assessed as cognitively normal (122 subject or 30.5%) or diagnosed with AD (66 subjects or 16.5%) or MCI (212 subjects or 53%). In this research, they are randomly divided into two groups. One group data are used for statistical analysis to generate a classifier for AD and MCI. The cases in the second group are used to verify the classifier to quantify the success rates of the diagnosis. Since the diagnosis results (AD, MCI, or normal) are known, they are gold standard to validate the classifier. The details of data grouping are given in Chapter 7.

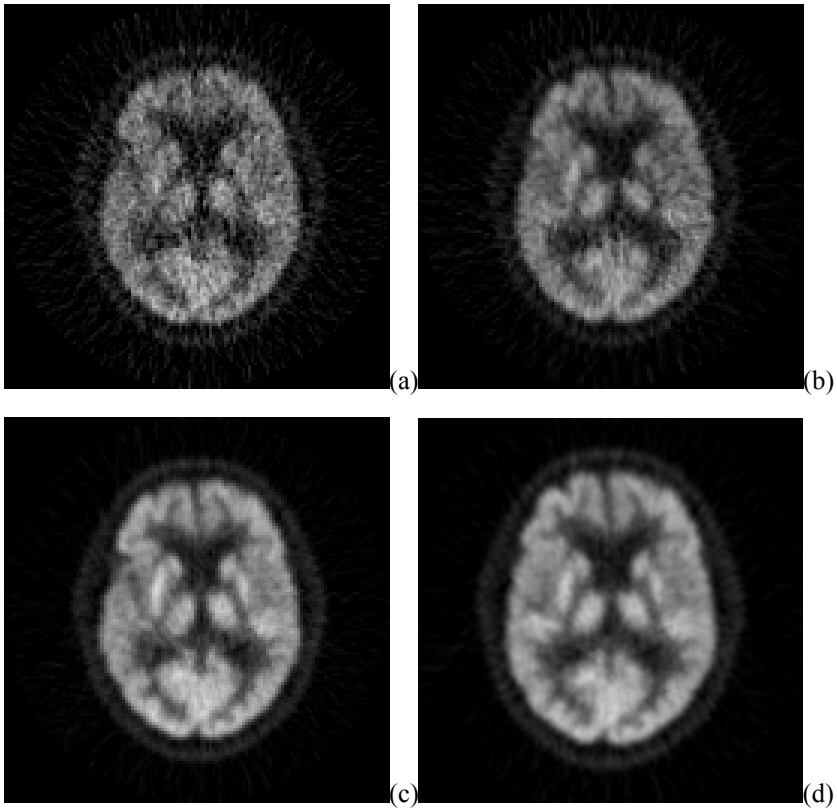

Figure 13. Examples of ADNI images
(a) a slice of original baseline image; (b) a co-registered image; (c) average image of dynamic scans; (d) reoriented image

3.4 Summary

This chapter gives an overview of the atlas-based approach and its implementation of each component, after defining the AD-specific structure. A digital brain atlas is firstly constructed by a set of powerful interactive and intelligent tools. It has AD-specific structures accurately segmented and labeled. The landmarks for spatial transformation are defined in the atlas. Thereafter, the brain areas are extracted from the PET images automatically and the landmarks are identified in PET images for spatial transformation, followed by the intensity normalization and statistical analysis.

Fifteen anatomical brain regions are selected as AD-specific structures, based on the state-of-the-art literature, followed by the introduction of the materials used in this research work.

Chapter 4

Brain Atlas Construction

This chapter presents a new digital brain atlas which includes the Alzheimer's disease (AD) specific structures to be constructed. As a brain atlas, it needs very high accuracy for each brain structure. Since the automated brain extraction methods give the results incomplete and anatomically incorrect, this chapter delivers an interactive post-processing platform with several powerful and intelligent tools for atlas construction to extract and label brain structures from volumetric neuroimages, followed by an introduction of the new brain atlas.

4.1 Brain Segmentation and Labeling

To construct a digital structural brain atlas from a high quality magnetic resonance imaging (MRI) dataset, basically there are two ways: 1) automatic generation by automated or semi-automated computer algorithms, and 2) manual generation by interactive editing tools. This section gives an example of high resolution MR images to be segmented and labeled by evaluation of automated methods and the interactive platform.

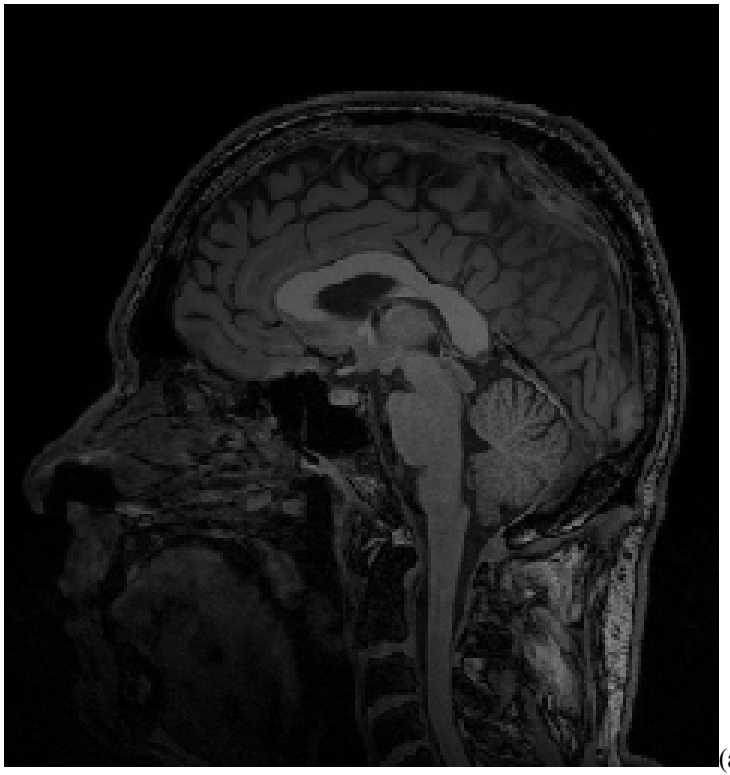

(a)

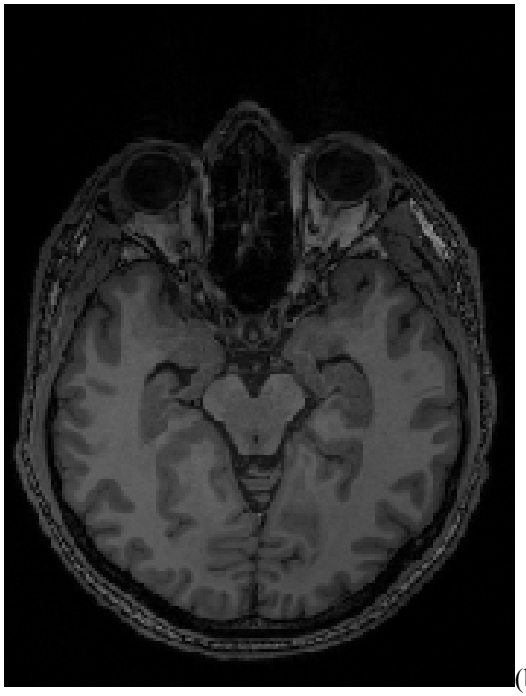

(b)

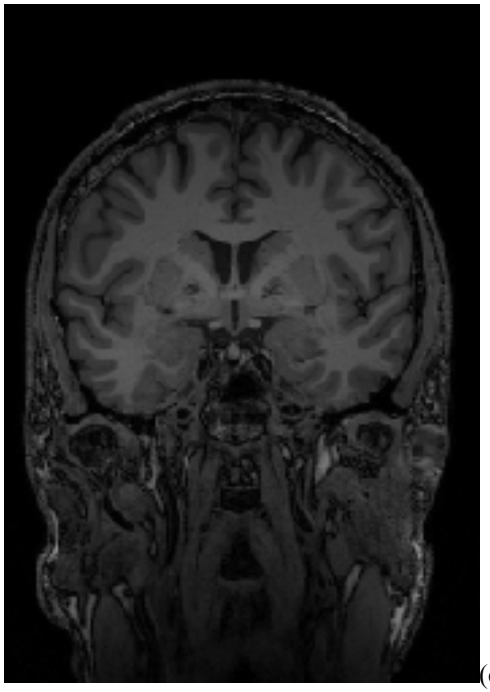

(c)

Figure 14. MRI images on planar views

(a) sagittal; (b) axial; (c) coronal orientations

4.1.1 High Resolution MR Images

The brain atlas is based on a 3-Tesla (3T) volumetric MRI dataset scanned by a SIEMENS TrioTim syngo MR B15 scanner with 32 channels. The dataset has a high resolution of 224×300×320 with its voxel size 0.8×0.8×0.8 mm^3. Figure 14 shows an original sagittal slice (Figure 14a), and the reformatted slices at axial (Figure 14b) and coronal (Figure 14c) orientations. Both the cerebrum and cerebellum are completely included.

4.1.2 Automated Segmentation Programs

As discussed in Chapter 2, the automated or semi-automated methods highly depend on assumptions and parameter settings. They may give unexpected and incorrect results if some of the assumptions are not satisfied or some of the parameters are not set correctly. Figure 15 shows a slice with segmentation results from FreeSurfer [Dale et al., 1999] (version 4.2.0), a state-of-the-art automated brain segmentation method. In order to view the original image clearly, the segmented results are converted from the color-coded image to contours. There are several segmentation problems shown in Figure 15: under-segmented grey matter (a and b), incompletely (too shallow) segmented sulci (c), and unclear cortical thickness (d). Therefore, further interactive operations are necessary to correct and enhance the results. In addition, automated methods usually generate results as bitmap images, which are very difficult to edit and need to be converted into contours to become editable on the original scans without blocking them. If the automated results are far from the expectation, the correction effort may need more manual operations and even longer time than the interactive drawing directly from the images by making use of intelligent and user friendly tools.

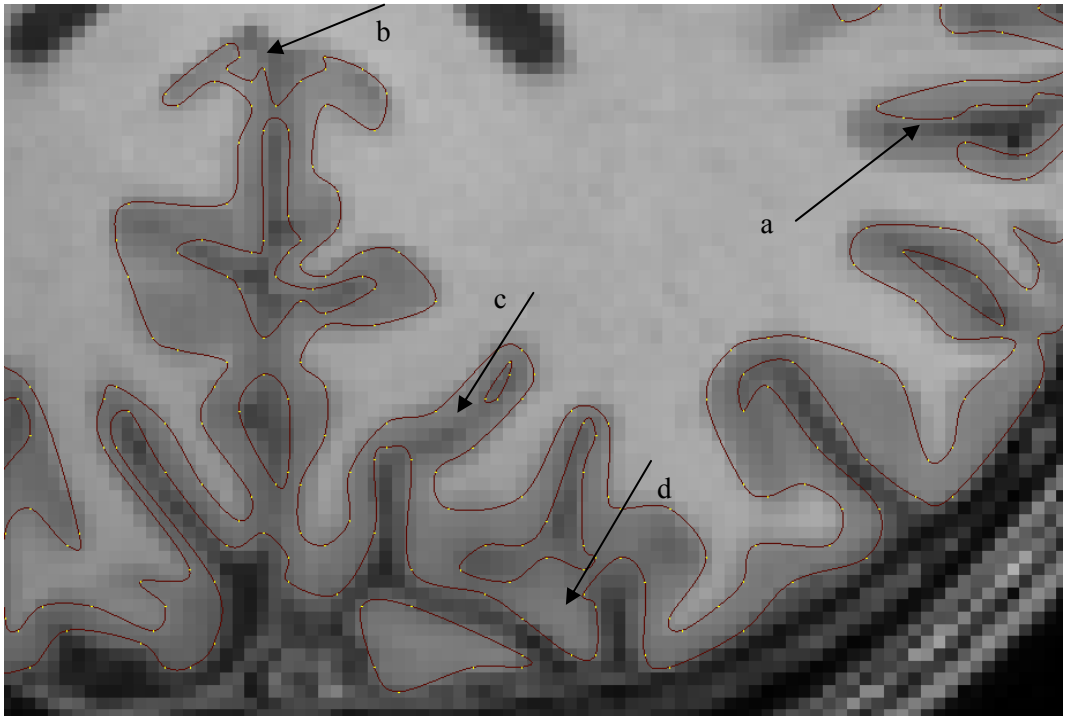

Figure 15. Problems in segmentation by using FreeSurfer
(a) (b) under-segmented grey matter regions; (c) incompletely segmented (too shallow) sulcus; (d) unclear cortical thickness

4.1.3 Intelligent and Interactive Editing Tools

An intelligent and interactive editing tool is crucial to extract the areas of interest from images in applications which require images to be accurately segmented. However, a high resolution dataset with hundreds of slices needs hours or even days to be accurately segmented manually. Inconsistency may occur even for a same neuroanatomy expert while identifying the pixels due to partial volume effects, windowing, and different lighting conditions of his or her working environment. An accurate delineation of sulci and gyri needs thorough anatomical knowledge and three-dimension (3D) visualization to resolve. Therefore, time-consuming manual segmentation can be augmented and speeded up by applying interactive and intelligent tools. The tools are also helpful to improve the

segmentation quality and reduce the manual working time, as the correction effort may need a lot of manual operations.

Interactive editing tools read the inputs from the user, and may apply them to some simple automated methods. The methods must be fast enough because the results based on these inputs should be shown to the user immediately for further enhancement. The existing interactive segmentation and editing tools are divided into two main groups: 1) edge detection and drawing on two-dimension (2D) images slice by slice, and 2) object detection and surface modification on 3D data directly. Examples of 2D image editing tools are *Adobe Photoshop*, *Microsoft Paint*, *Paint.NET*, and *TkMedit* from the FreeSurfer package. They provide pens, brushes, or even labeling to select the pixels from the images. Examples of 3D image editing tools are *Blender* and *TkSurfer* from the FreeSurfer package. They provide spline, polygon, and surface editing to extract the regions of interest.

Both groups have obvious advantages and disadvantages. The advantages of editing on 2D images are simple and precise because the editing is on the original data. The regions or even pixels are determined to be included or not by the user, slice by slice. However it is difficult to determine the correct anatomy. Also, the editing on 2D images slice by slice is very time-consuming especially for high resolution dataset with hundreds of slices. Visualization of segmented result on 2D images does not mean anatomical correctness. 3D editing is superior and efficient, though more complex than editing of 2D images. The editing of an object may affect its neighbors, even for those which are previously modified. Thus the editing task is difficult to control and unexpected results may be caused. Our approach combines the advantages of both. It is simple and precise by working on the 2D images, and makes use of the visual inspection in 3D as well.

4.2 Interactive Platform for Brain Extraction and Labeling

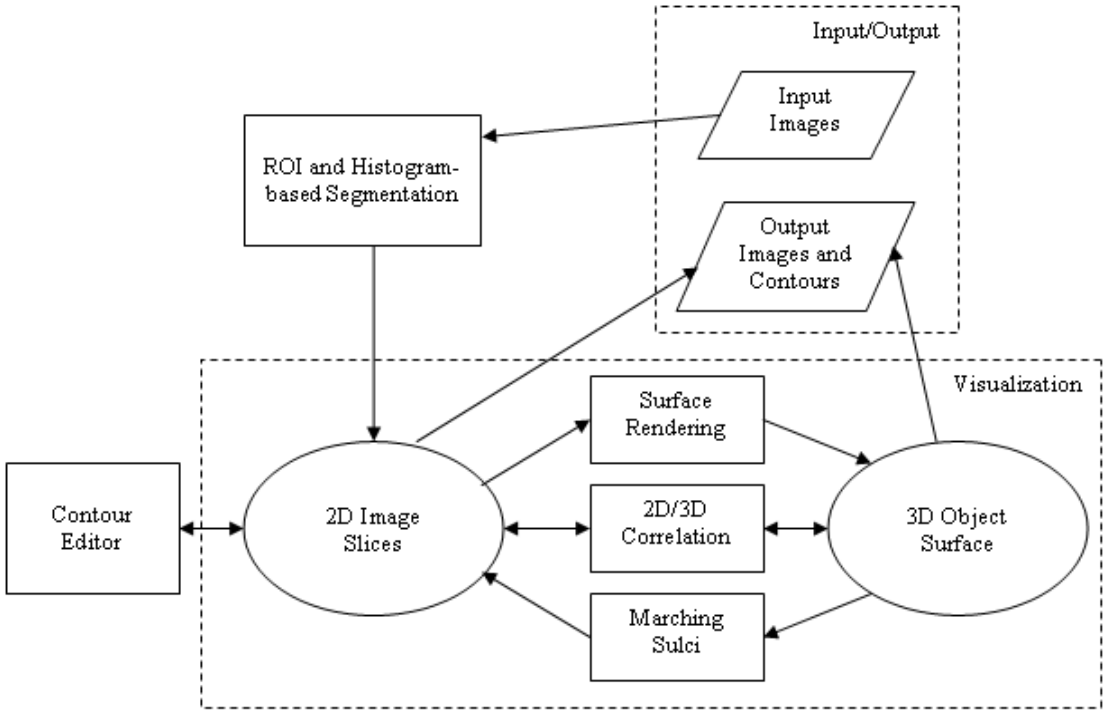

Figure 16. Intelligent and interactive platform for brain extraction and labeling

To construct a brain atlas, an interactive platform is developed to assist the neuroanatomy expert in accurate brain segmentation. The platform provides a set of interactive and intelligent tools to allow the user to generate high quality, accurate and correct brain volumes with labels of the anatomical structures including AD-specific structures. The images generated by a skull removal software (e.g. BrainSuite) are the initial input to the region-of-interest (ROI) based segmentation tool to identify the sulci. For images with segmented results or even brain structure labeling information generated by automated brain segmentation software (e.g. FreeSurfer), the contours are generated for further enhancement or fine tuning. A powerful contour editor is used instead of a

pixel editing tool for a more efficient manual editing. The 2D-3D correlation tool, marching sulci tool, and multiple dataset synchronization tools are able to assist users to easily and efficiently locate potential incorrect areas or landmarks to be edited.

Figure 16 shows the architecture of the interactive platform for brain extraction and labeling. It consists of four modules:

- *Input/Output*

  It is responsible to load or read medical images from disks and write the results back to the disks. It supports different modalities of medical images, e.g. MRI or computed tomography (CT). The results include the segmented regions, defined contours, edited pixels, and 3D surface rendering objects. It handles images, contours, 3D object files, and settings of the software.

- *Visualization*

  It includes 2D display of each slice, 3D display of object surfaces, 2D-3D correlation, and synchronization of different input images.

- *Contour Editor*

  It contains a set of functions to provide the powerful editing features for contour editing on 2D images.

- *Interactive Segmentation*

  It comprises left and right hemisphere definition, histogram, region growing algorithm, 2D-3D correlation, and 3D marching sulci.

In this section, five major tools of the modules are presented. They are 1) efficient ROI and histogram-based segmentation, 2) powerful contour editor, 3) 2D and 3D correlation, 4) marching sulci, and 5) multiple dataset synchronization.

4.2.1 ROI and Histogram-based Segmentation

The ROI and histogram-based segmentation tool provides the ROI-based histogram, and re-classifies the voxels with the threshold value selected on the histogram graph (shown in Figure 17). It basically consists of two steps: 1) draw a ROI (Figure 17a), and then its histogram is generated and displayed (Figure 17b); 2) select and adjust the threshold value on the histogram graph.

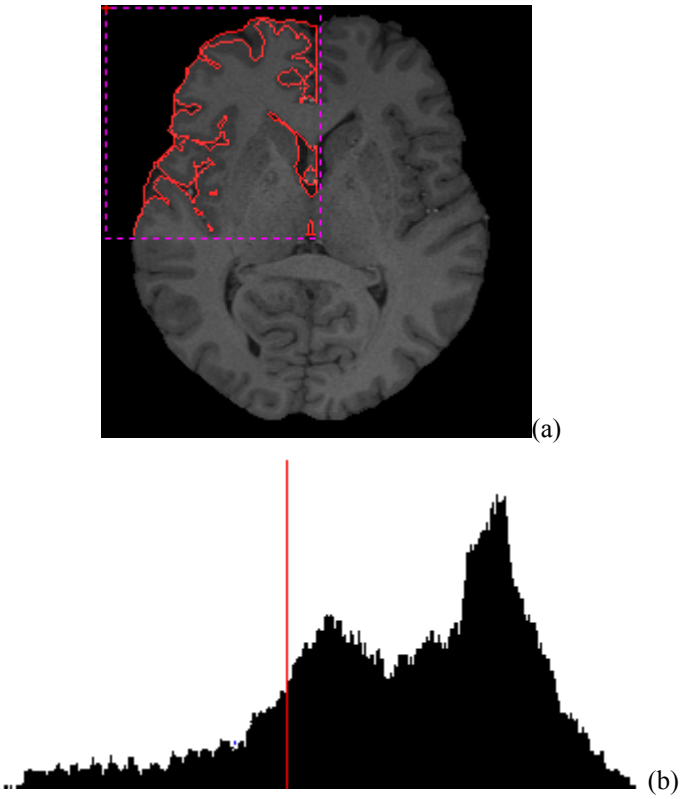

Figure 17. Region-of-interest selection and the corresponding histogram
(a) ROI drawing and the segmented results; (b) histogram of ROI and threshold selection

The segmented result is immediately displayed on the screen (Figure 17a) for the user to adjust the input. The user only needs to select a few ROIs to generate the segmented image and the tool will merge them together and generate the contours for further

enhancement. For the cases with serious intensity inhomogeneity within a single slice, the user may need to define more ROIs.

Due to the intensity inhomogeneity between slices, local threshold values for each slice or even each ROI are required. Experience shows that the definition of ROIs and their thresholds have close values with their neighboring slices. Therefore, an efficient way to estimate the local ROIs and threshold values is to remember the parameters selected by the user, and then propagate them to the neighboring slices to reduce the user intervention. The estimated values are the default threshold values of a slice, and can be easily adjusted by the user. The new adjusted values will be learnt and applied to determination of threshold values for the subsequent slices.

4.2.2 Powerful Contour Editor

The contour editor provides an efficient and flexible way for the user to enhance the contours. Besides the standard operations like creation and deletion of contours, the editor provides several powerful features. It is able to:

- add, modify, and remove control points on contours (to reshape or enhance the segmentation results);
- view original images while contouring;
- split a contour into two (very useful to deepen the sulci and cope with the partial volume effect), or join two contours into one;
- edit contours by checking 3D display;
- add labels for contours (to process simultaneously multiple objects);
- separate brain into two hemispheres (useful to edit the interhemispheric fissure region);

- copy a contour on a slice and then paste it onto its neighboring slice (to speed up editing);
- manipulate contours based on ROI (both within and outside the ROI);
- display surface of the edited object (helpful to generate anatomically correct structures, see also below 2D-3D correlation);
- duplicate contours to delineate multiple boundaries;
- display and edit contours in triplanar views of the same volumetric dataset (useful to find out and locate inaccuracy segmentation results), shown in Figure 18;
- label anatomic structures which are defined in Terminologia Anatomica, an international standard on human anatomical terminology, defined by Federative Committee on Anatomical Terminology (FCAT) [Terminology, 1999], shown in Figure 19;
- display multiple contours with different contour types;
- fill contours with colors to highlight the segmentation results;
- maintain floating point representation for more accurate coordinates;
- map contours on 3D for accuracy checking
- modify connected contours at a same time (very useful for the segmentation of adjacent structures);
- display neighboring contours.

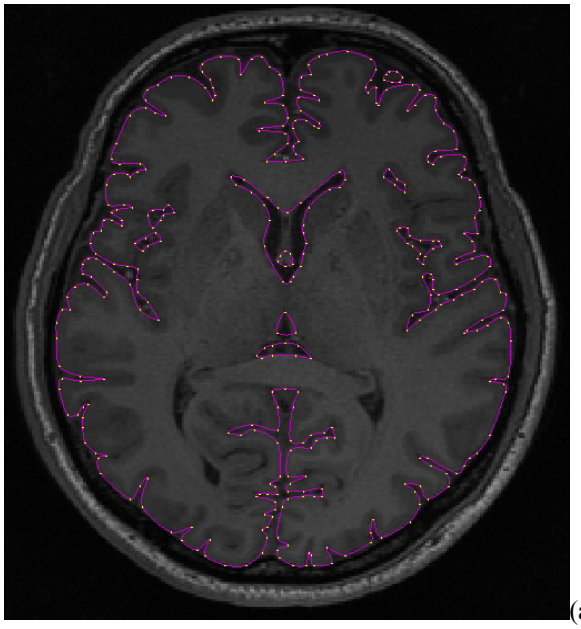

(a)

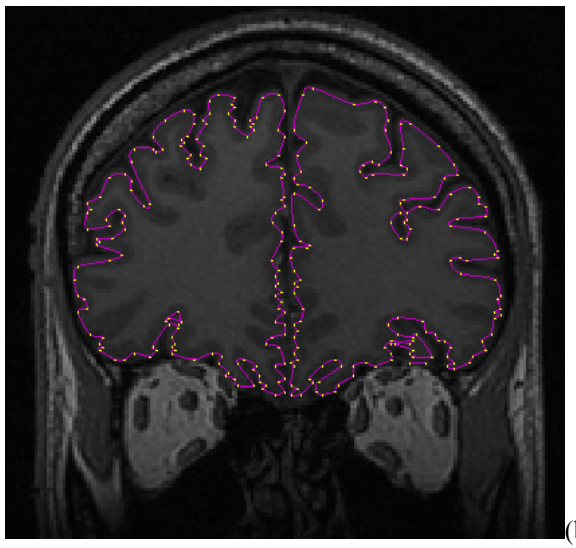

(b)

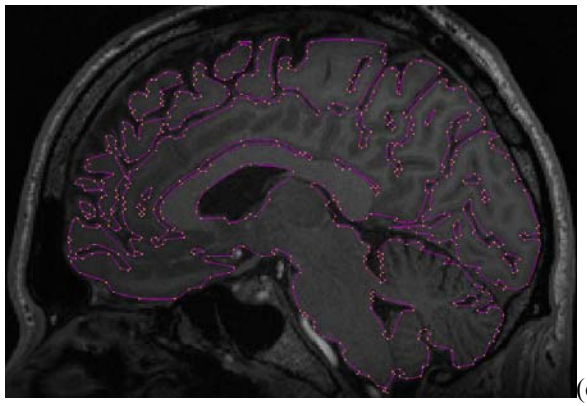

(c)

Figure 18. Contour editing on triplanar views
(a) axial view; (b) coronal view; (c) sagittal view

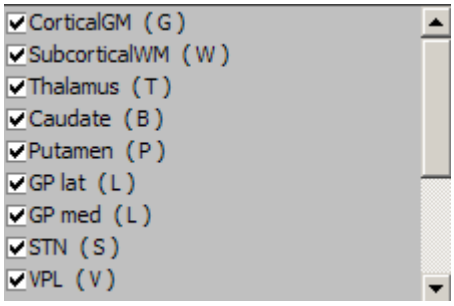

Figure 19. Anatomical index for labeling of structures.

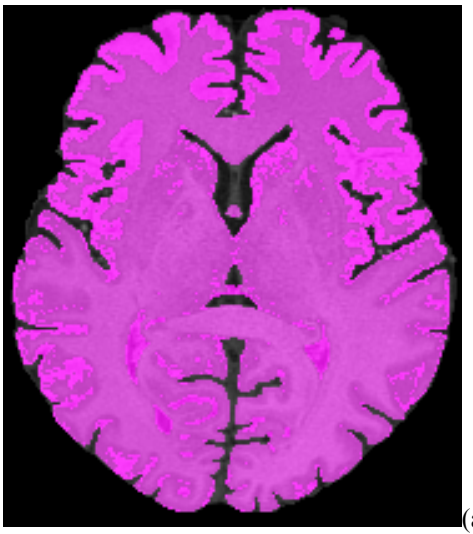

(a)

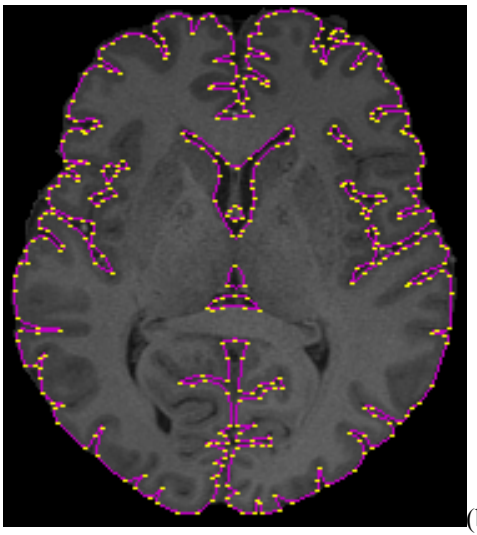

(b)

Figure 20. Examples of editing tools

(a) pixel editing; (b) contour editing

Comparing to pixel editing, which is easy to use and straightforward but has numerous limitations, the contour editor has obvious advantageous. Figure 20 gives examples of pixel editing and contour editing. For a pixel editing tool, the user is usually not able to view the original images while editing (shown in Figure 20a), and for contour editing, the original image is almost not covered by contours and the user still has a good view of the image (Figure 20b). Figure 21 gives another example. The sulcus pointed by the arrow (Figure 21a) is under-segmented and it can be easily corrected by adding a few more points (Figure 21b).

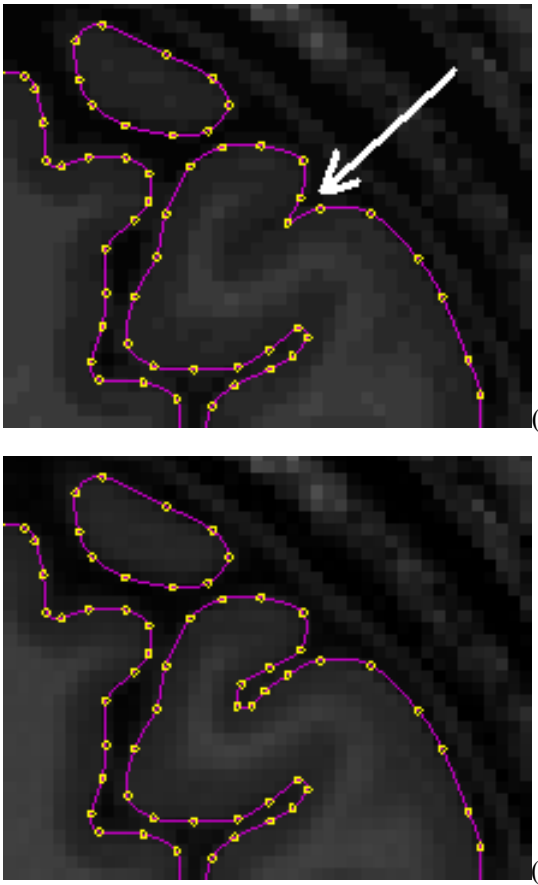

Figure 21. An example of sulcus editing
(a) under-segmented contour; (b) corrected contour

4.2.3 2D-3D Correlation

The 2D-3D correlation greatly facilitates generation of correct anatomy. In general, on 2D slices it is difficult to determine the correct anatomy, mainly due to the partial volume effect and when the cortex is lying in the editing plane. The 3D display enables identification of problems, such as unrealistic shapes, too shallow sulci, bridges between gyri, bumps and holes on the cortical surface, and missing or incomplete sulci, among others. Then, the region to be corrected is identified on the cortical surface and it is mapped on the original 2D image for editing by the contour editor. Conversely, only location on a 2D slice can be mapped on the 3D surface for inspection.

The brain surface is rendered as millions of triangles (when not decimated) lighted and shaded by OpenGL [Shreiner et al., 2005], which is widely used in 3D rendering applications. The triangles are generated by the Marching Cubes [Lorensen and Cline, 1987] which calculates whether each isotropic voxel is inside or outside the surface. The coordinates of each point on a 2D image have one by one correspondence with those of the point in the 3D space.

Usually the 3D surface rendering display is more obvious than 2D image display to show the shapes of anatomic structures, as shown in Figure 22, but the correlation from 3D display to 2D image coordinates is more complex. While mouse is clicked on a 3D display, only one point with 2D coordinates (x, y) is provided (pointed by the arrow in Figure 22a). The correlated 2D position of the point needs a few steps to be located. Firstly, the triangles which are within the mouse click are identified, and the one nearest to the user is selected. If the selected triangle is not small enough (<0.1mm of the longest edge), then it will be equally divided into 3 smaller triangles and the one within the mouse click is selected. The selected triangle will be repeatedly divided into smaller

triangles until the selected triangle is small enough. The center position of final selected triangle is considered as the coordinates of the selected point on the 3D display as well as the coordinates on 2D image. The user can focus on this position to correct segmentation as shown in Figure 22b.

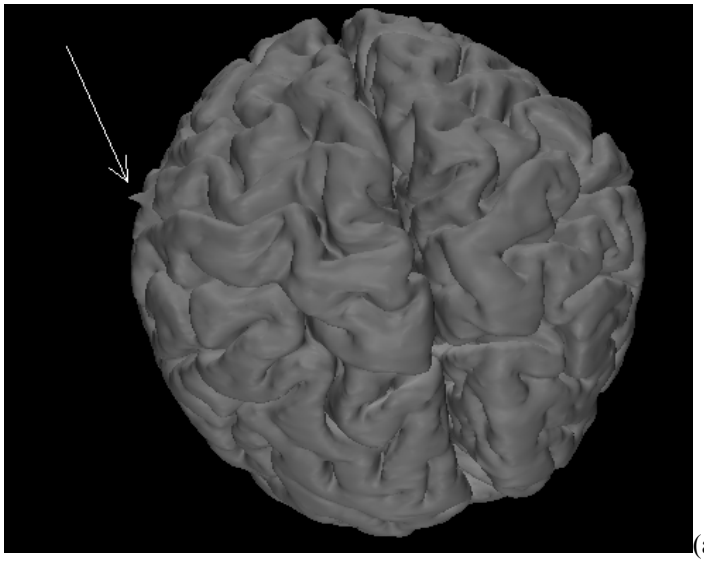

(a)

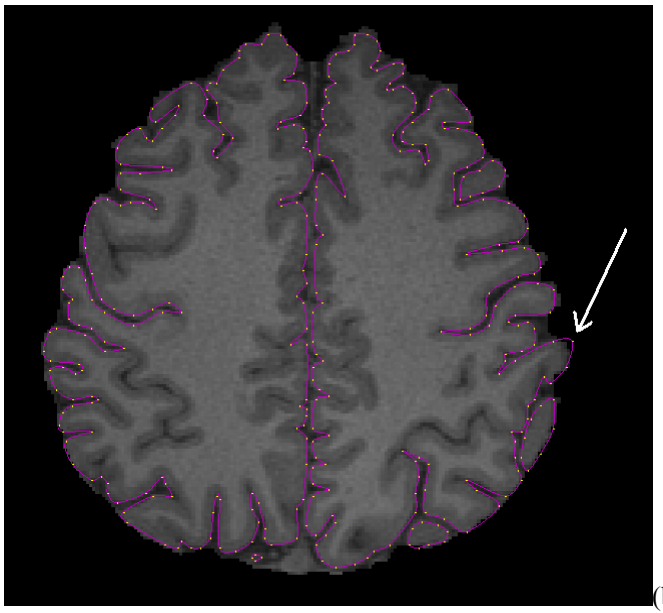

(b)

Figure 22. Spatial correlation of 3D with 2D
(a) mouse click on 3D display; (b) correlated 2D position

4.2.4 Marching Sulci

The sulcus is one of the most difficult areas to be properly determined. The slight inaccuracy is often missed, or sometimes misled by pixels with similar intensities. In order to highlight such a kind of slight inaccuracy, an interactive component is implemented to calculate the curvatures for each vertex of triangles and paint the different colors for the vertices. The mean curvatures are calculated by making use of Visualization Toolkit (VTK) [Schroeder et al., 2004] library. The calculated results are mapped to predefined colors. Figure 23 shows examples of surface curvatures.

The convex surfaces have higher curvature values (positive), while the concave surfaces have lower curvature values (negative). The flat areas have curvature values close to zero. A threshold value is selected by the user to determine curvature highlighting. Figure 23a shows an example of surface curvatures with mean curvature value 0.2. That means, the surfaces with curvature values of +0.2 (-0.2) or higher (lower) are painted with blue (red) color and the surfaces with curvature values between -0.2 and +0.2 are painted with grey color. Figure 23b gives an example with mean curvature value 2 and Figure 23c shows the zoom-in image of Figure 23b. Our experience shows that the surface areas highlighted in such a way have likely wrong segmentation.

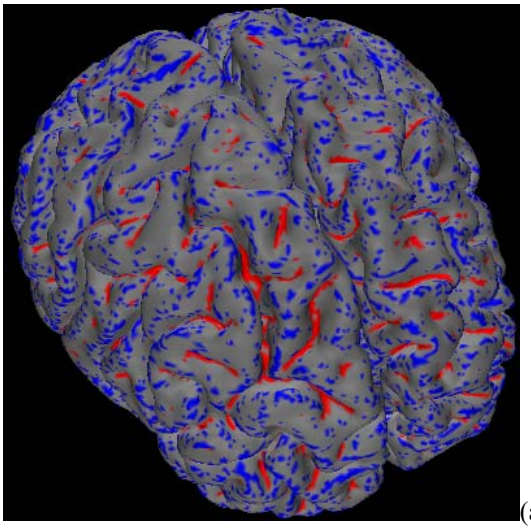

(a)

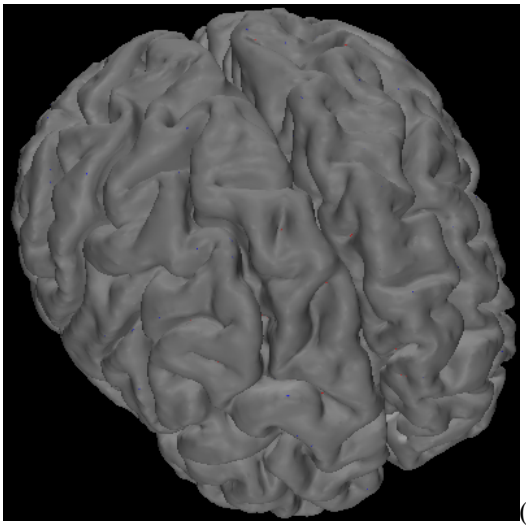

(b)

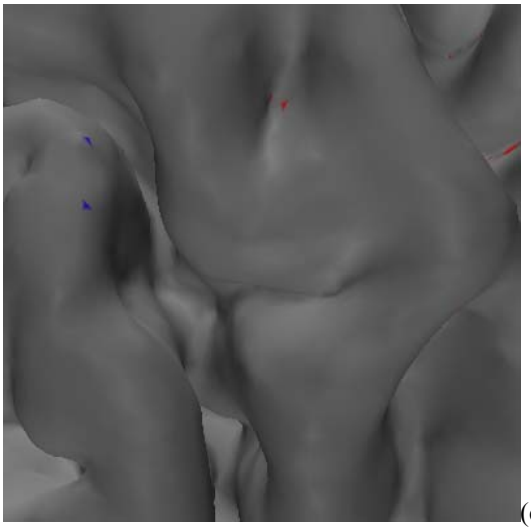

(c)

Figure 23. Examples of surface curvatures

Mean curvature value (a) 0.2; (b) 2; (c)zoom-in of (b)

4.2.5 Multiple Dataset Synchronization

Synchronization of multiple dataset display enables the user to browse through different images at the same time. If user has multiple scans of different study or different modality for a same patient, the synchronization tool allows user to display them at the same time. To assist the atlas construction with high accuracy, multiple scans from same person were acquired on 1.5T, 3T, and 7T images. Those images need to be references each other especially for the areas with partial volume effect. While user is moving an image, changing zoom, or showing different slices, another images are simultaneously changed. The user always has the same view of different images, no matter which image is being changed. Two volumetric datasets may have different volume sizes, different voxel sizes, and even different modalities.

4.3 Experiment Results and Discussion

This section gives the results of automated brain segmentation methods and interactive editing tools with a same high resolution MR images as input. The automated methods, including FMRIB Software Library (FSL), BrainSuite, Statistical Parametric Mapping (SPM), and FreeSurfer, were tested on a standard personal computer with 2.4 GHz CPU running Windows XP Professional. The interactive editing tools, including histogram generation, thresholding, 2D-3D correlation, and multiple dataset synchronization, are running and testing on the same computer. After that, the comparisons of both results are given.

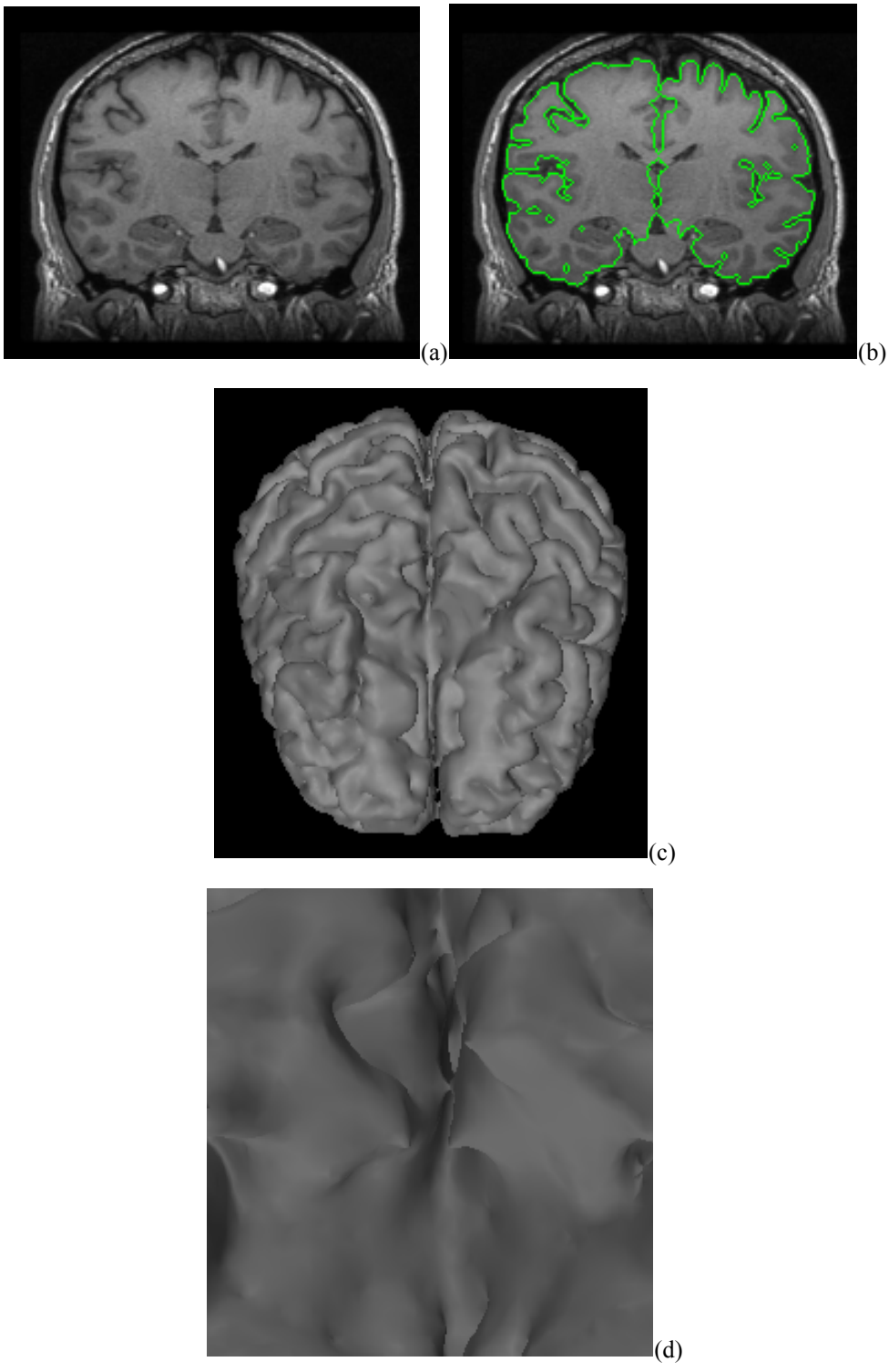

Figure 24. Segmented results of FreeSurfer

(a) original coronal slice; (b) results for 2D slice; (3) gross view 3D surface rendering; (d) close view 3D surface rendering

4.3.1 Results of Automated Methods

Figure 24 shows an original slice (Figure 24a) and the results for 2D slice (Figure 24b), gross view (Figure 24c) and close view (Figure 24d) of 3D surface rendering, from the pial surface generated by FreeSurfer in coronal orientation. FreeSurfer transformed the original images into isotropic size 256×256×256. In such case, the segmented results have to be transformed back to the space of the original images for comparison of other approaches.

Figure 25 presents the results generated by FSL (Figure 25a1-a4), BrainSuite (Figure 25b1-4), and SPM (Figure 25c1-c4). They are the results for a superior slice (a1, b1, c1), the results for an inferior slice (a2, b2, c2), gross view 3D surface rendering (a3, b3, c3), and close view 3D surface rendering (a4, b4, c4). FSL divides the brain into grey matter (GM), white matter (WM) and cerebrospinal fluid (CSF). The results shown in Figure 25a1-a4 are the combination of GM and WM. BrainSuite generates not only the results of GM, WM, and CSF, but also the partial pixels of GM/WM and GM/CSF. The results shown in Figure 25b1-b4 include the partial pixels of GM/WM but exclude the partial pixels of GM/CSF. SPM gives the probabilities of GM, WM, and CSF. The results had 90% confidence of segmented GM and WM (Figure 25c1-c4). From 2D image slices, the segmentation results are good and look roughly alright, at least the inaccuracies are not obvious, from an image processing point of view. However, 3D views show apparent incorrect anatomy, e.g. in the superior sagittal sinus.

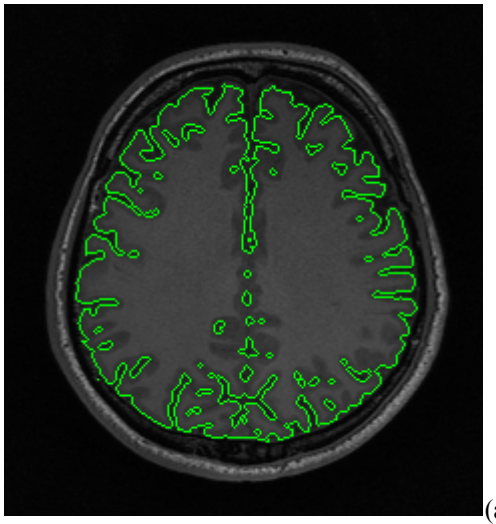
(a1)
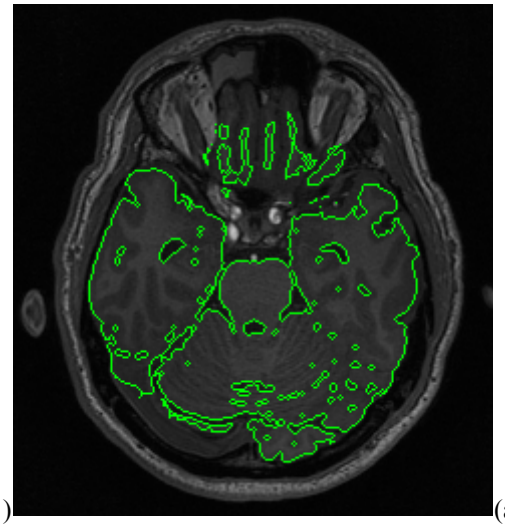
(a2)
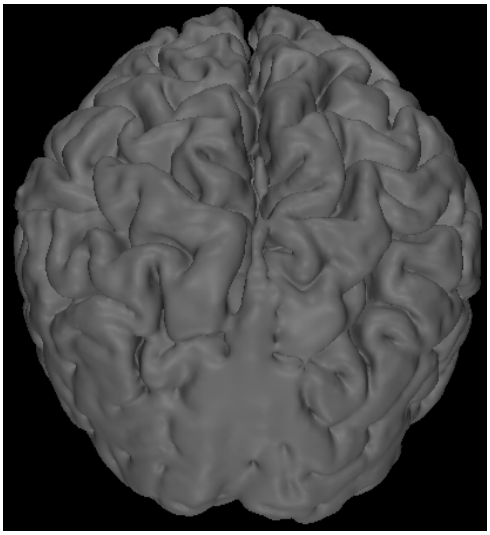
(a3)
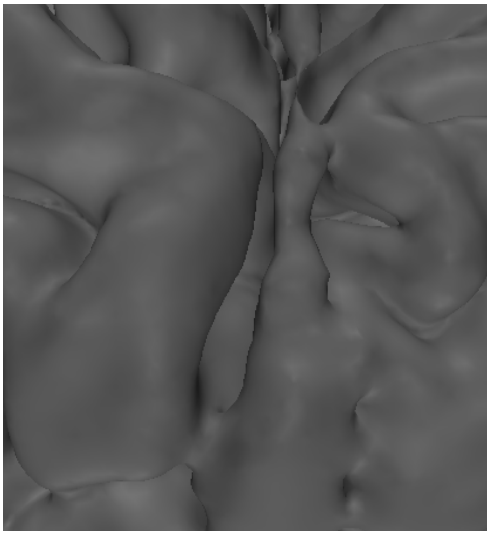
(a4)
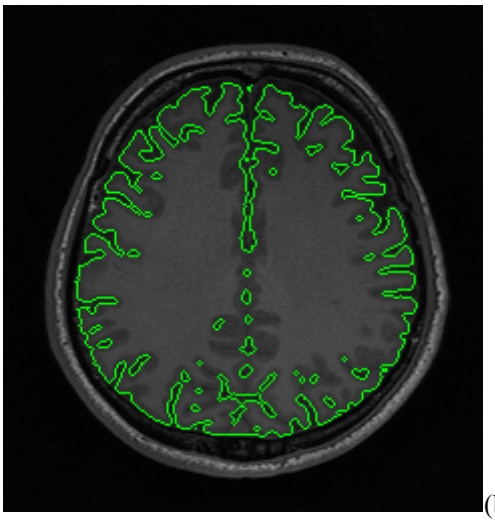
(b1)
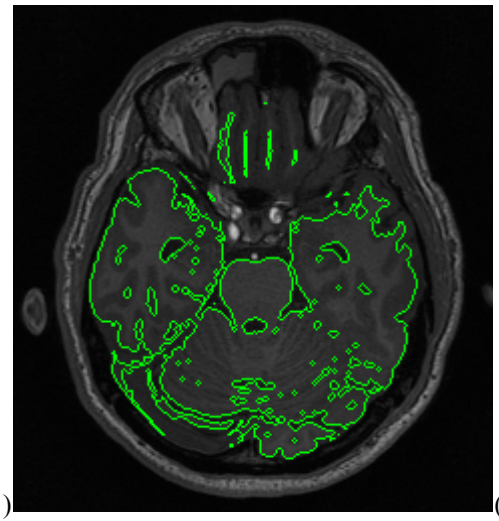
(b2)

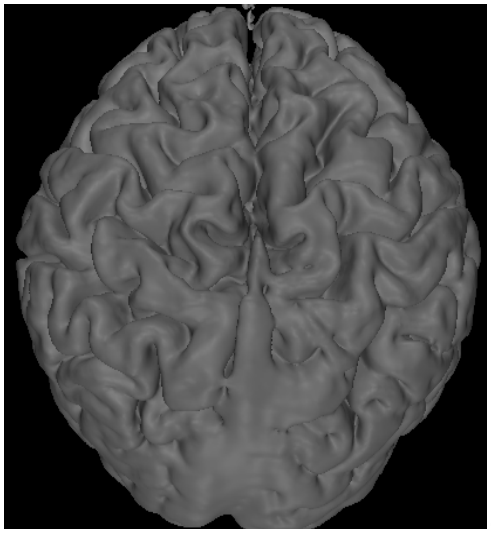
(b3)
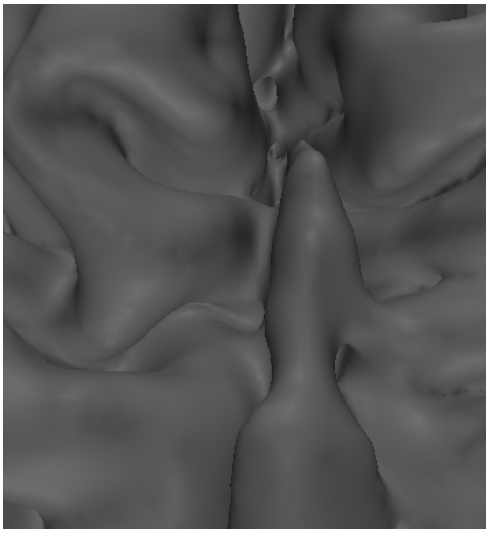
(b4)
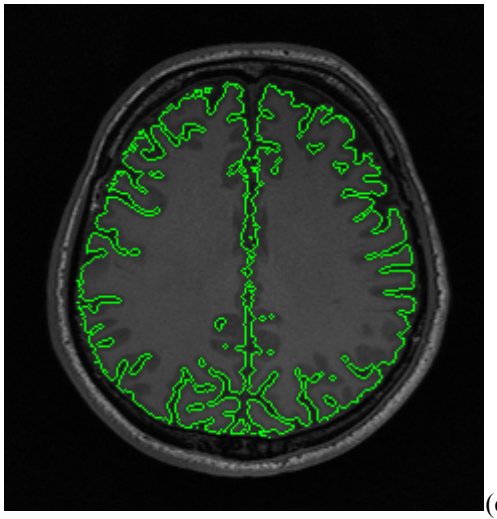
(c1)
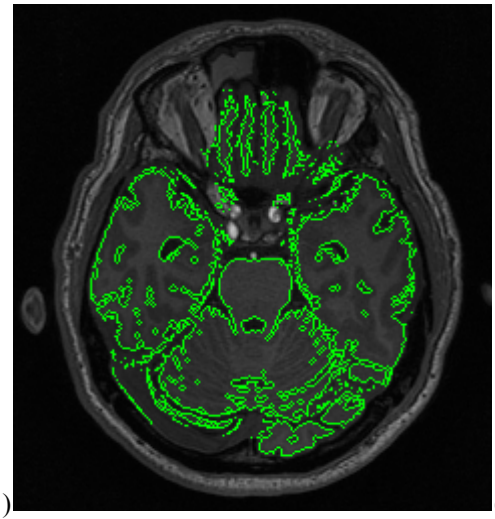
(c2)
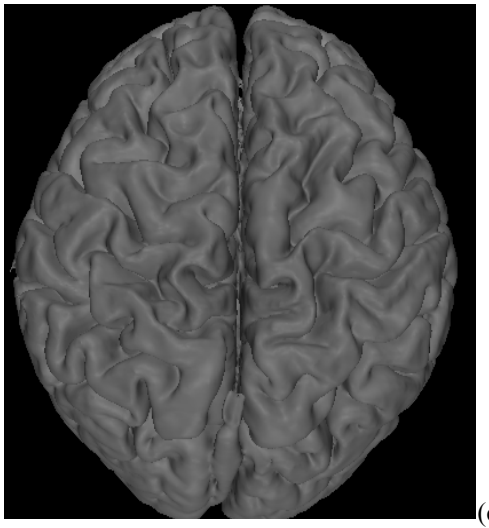
(c3)
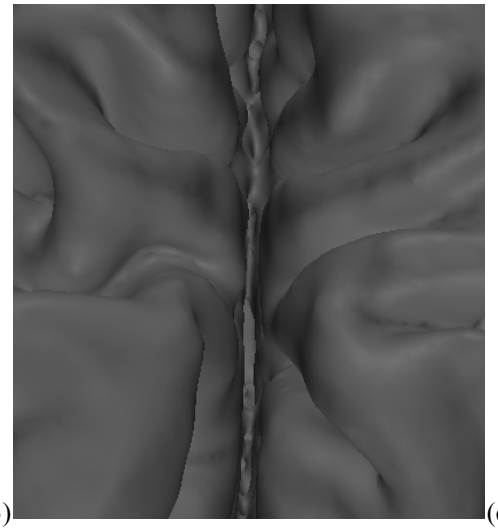
(c4)

Figure 25. Segmented results of automated algorithms

(a1) – (a4): results for FSL; (b1) – (b4): results for BrainSuite; (c1) – (c4): results for SPM

Figure 26 gives the comparison of the results from one of the automated brain extraction programs (Figure 26a) and the further gyri segmentation done by a neuro-anatomy expert working on the proposed interactive platform (Figure 26b). The first three 2D images are the superior slice, mid slice, and inferior slice. The 3D images are the outcome of surface rendering based on the segmented 2D images. Figure 27 gives the results of one hemisphere and a close view of sulci generated by the proposed interactive tools.

Table 5 compares the results from the automated brain extraction programs and the results by applying interactive tools. *Volume* is the number of voxels which were segmented from the images. *True Positive (TP)* with success rate, and *False Positive (FP)* and *False Negative (FN)* with their error rates are calculated for each automated method. In average, about 4% false positive and 10% false negative were reported.

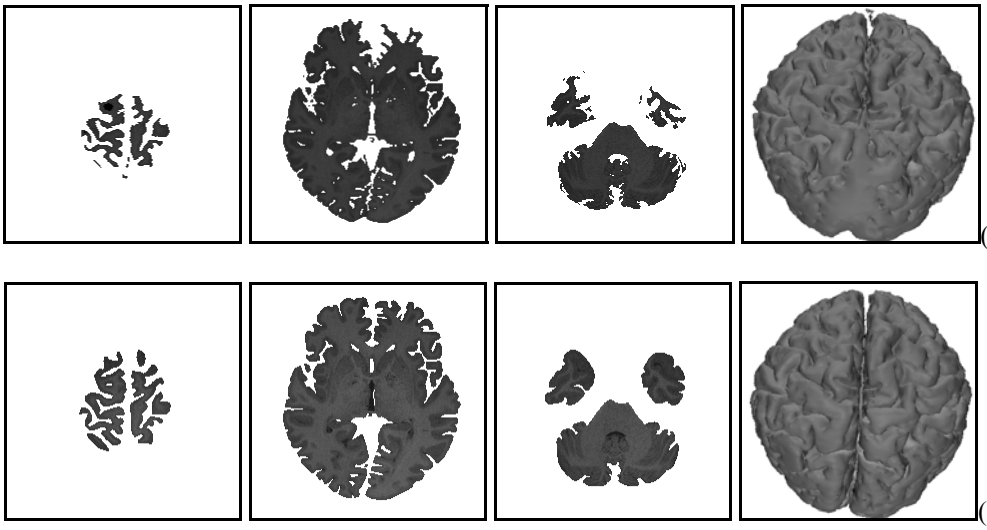

Figure 26. Results of automated brain extraction and applying interactive tools
(a) automated brain extraction; (b) interactive segmentation

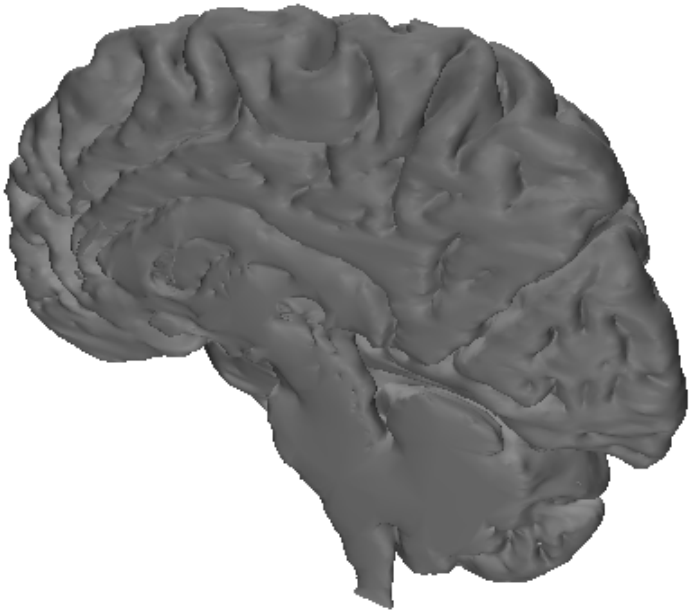

(a)

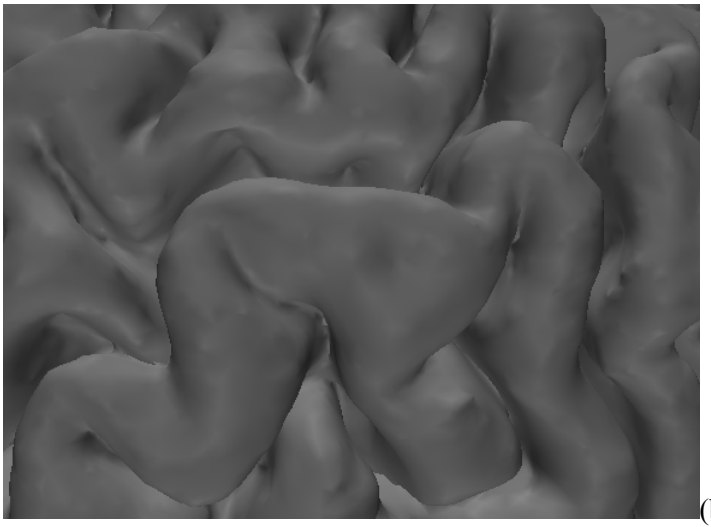

(b)

Figure 27. Segmented results in 3D view by gross and close view
(a) gross 3D view; (b) close 3D view

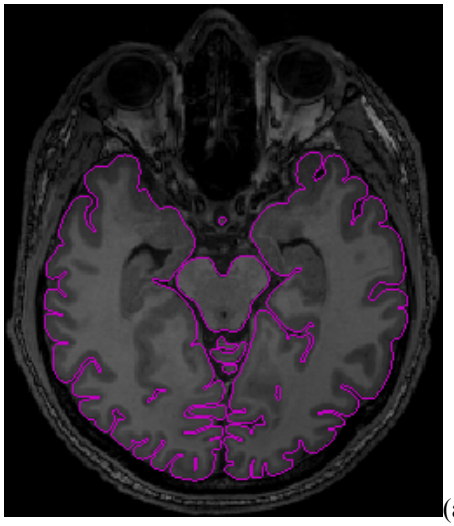

(a)

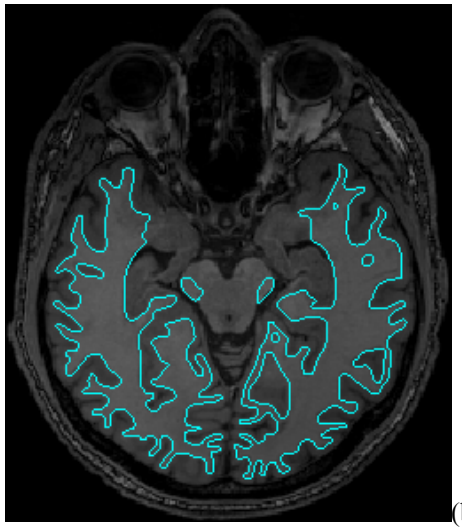

(b)

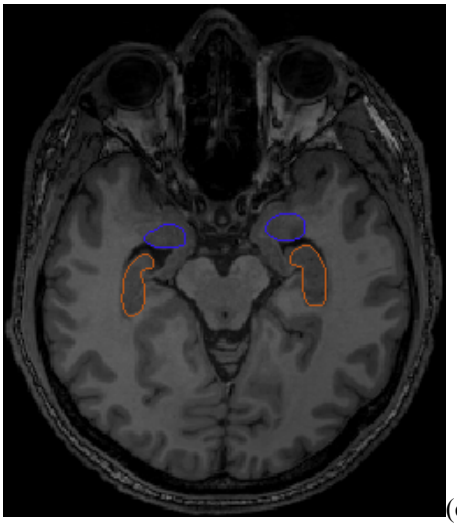

(c)

Figure 28. Segmented results in 2D view

(a) cortical GM; (b) subcortical WM; (c) amygdala and hippocampus

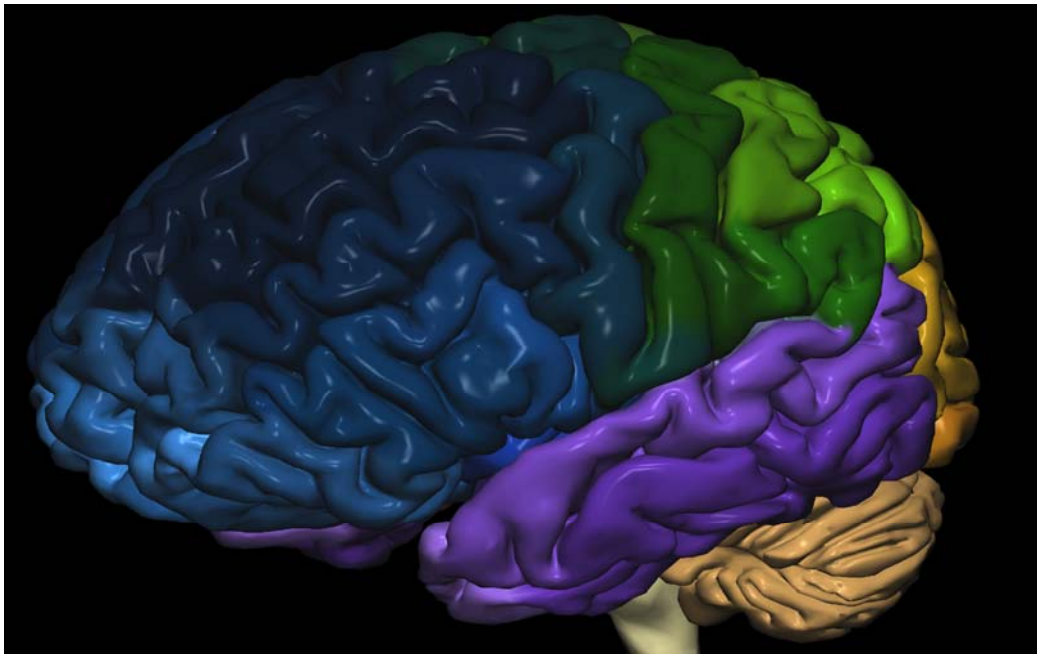

(a)

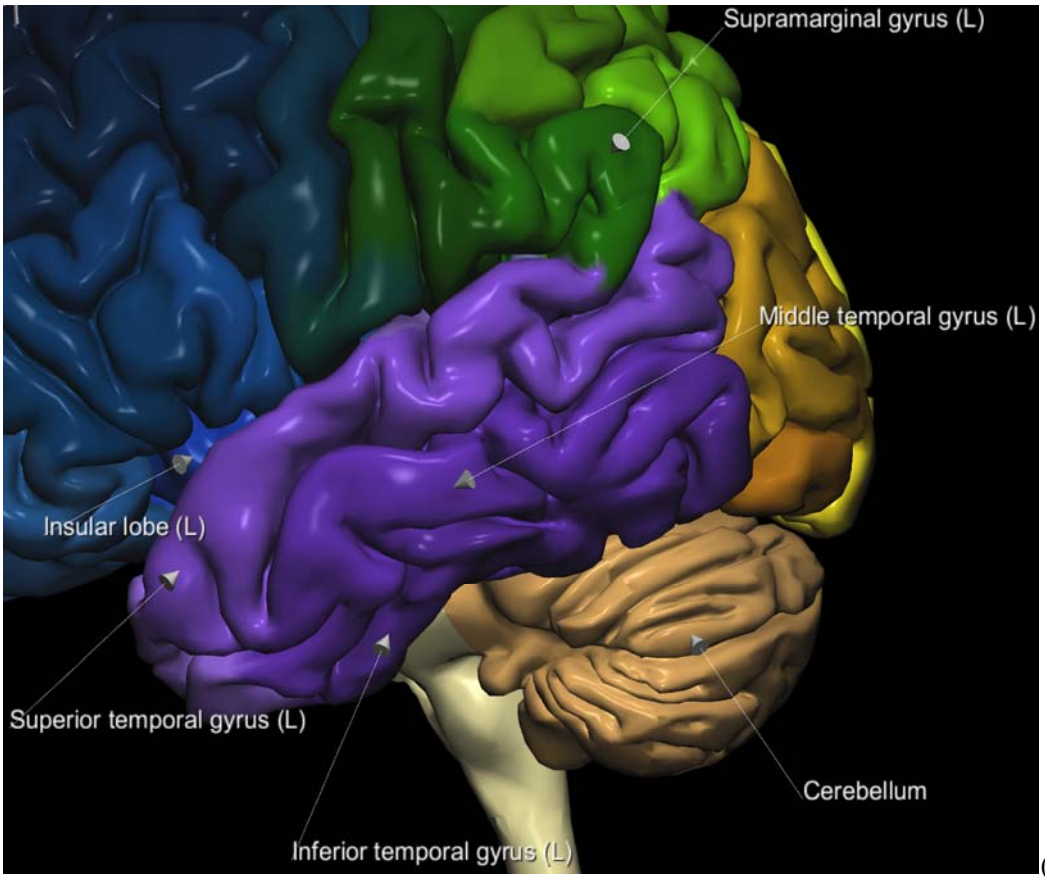
Supramarginal gyrus (L)
Middle temporal gyrus (L)
Insular lobe (L)
Superior temporal gyrus (L)
Cerebellum
Inferior temporal gyrus (L)

(b)

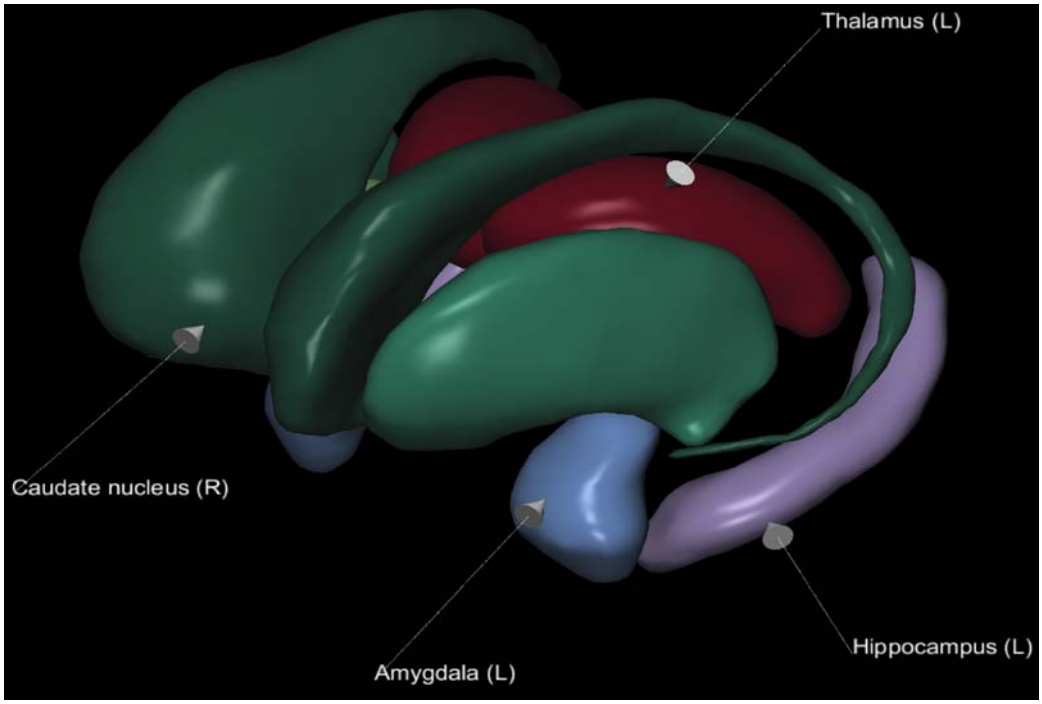

(c)

Figure 29. New brain atlas in 3D view

(a) whole brain cortex; (b) labeled brain cortex; (c) labeled sub-cortex

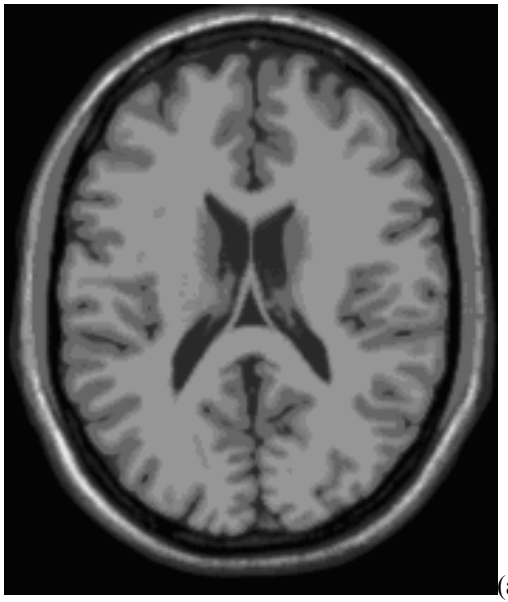
(a)
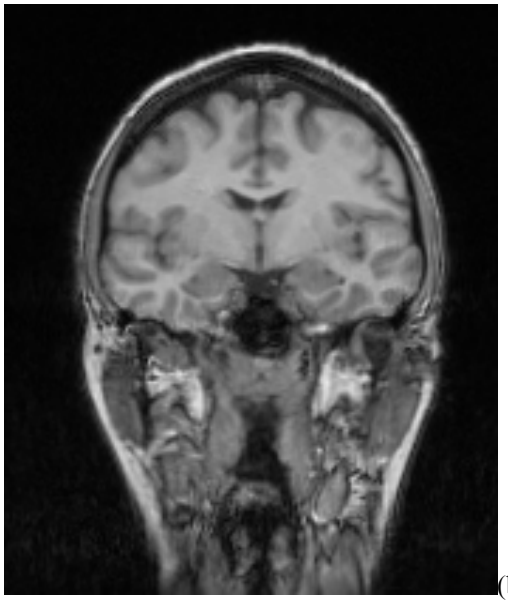
(b)

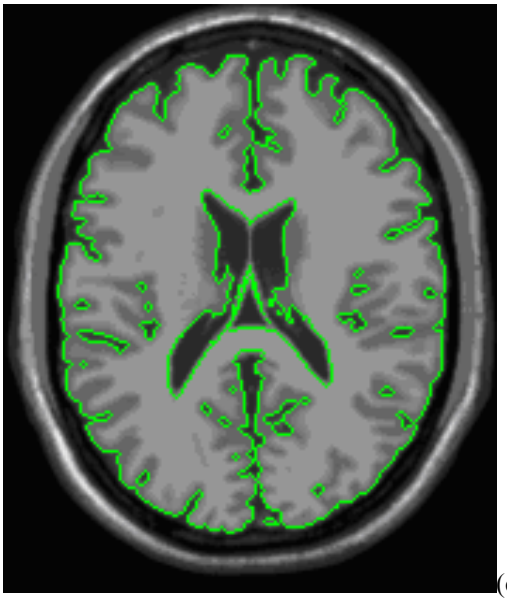
(c)
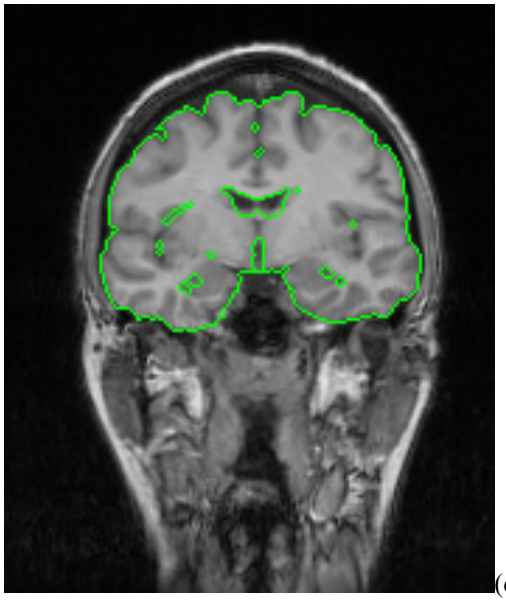
(d)
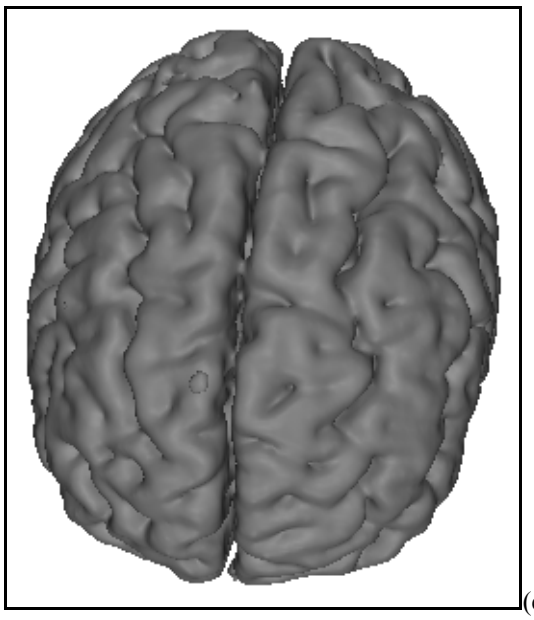
(e)
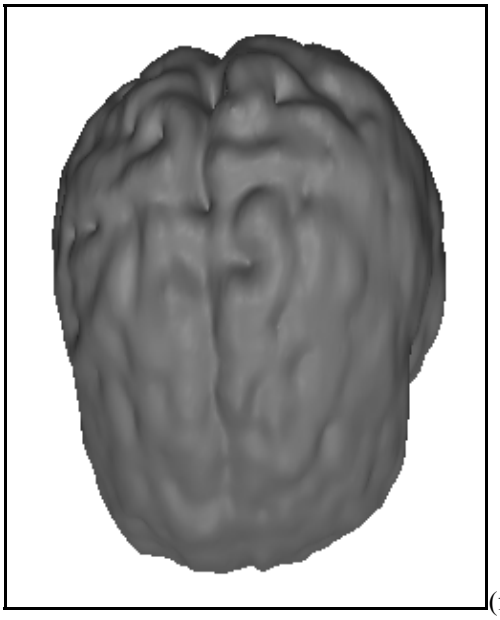
(f)

Figure 30. Ground truth from BrainWeb and IBSR

(left) BrainWeb; (right) IBSR; (a)(b) original 2D slices; (c)(d) 2D slices with segmentation ground truth; (e)(f) 3D surface display

Table 5. Comparison of results: automated methods and the interactive approach.

	FSL	BrainSuite	SPM	Interactive
Volume	2189741	2148855	2124200	1193220
(Overall rate)	96.09%	94.30%	93.22%	-
TP voxels	2090734	2054710	2055965	-
(TP rate)	91.75%	90.17%	90.22%	-
FP voxels	99007	94145	68235	-
(FP rate)	4.34%	4.13%	2.99%	-
FN voxels	187999	224023	222768	-
(FN rate)	8.25%	9.83%	9.78%	-

4.3.2 New Brain Atlas

The new brain atlas constructed by the interactive tools has labeled all AD-specific structures. It is a high resolution volumetric dataset of 512×512×211 pixel sizes with 0.32×0.32×0.6 mm^3 voxel sizes. Figure 28 gives the results of a slice with labels of cortical grey matter (Figure 28a), subcortical white matter (Figure 28b), and the structures amygdala and hippocampus (Figure 28c). Figure 29 shows the color-coded new brain atlas in 3D views of whole brain cortex (Figure 29a), labeled brain cortex (Figure 29b), and the labeled subcortical structures (Figure 29c), generated by the presented interactive tools.

4.3.3 Discussion

Currently the most automated methods reported their accuracy by comparison of segmented results with some ground truth. This is done by pixel-by-pixel comparison without applying any anatomical knowledge. Therefore, if the ground truth is only visually correct in images but not anatomically correct by knowledge, the comparison

may only make sense in pure image processing terms. Besides, in some software packages it is difficult to check the segmentation quality without mapping it to the original image size, e.g. in FreeSurfer.

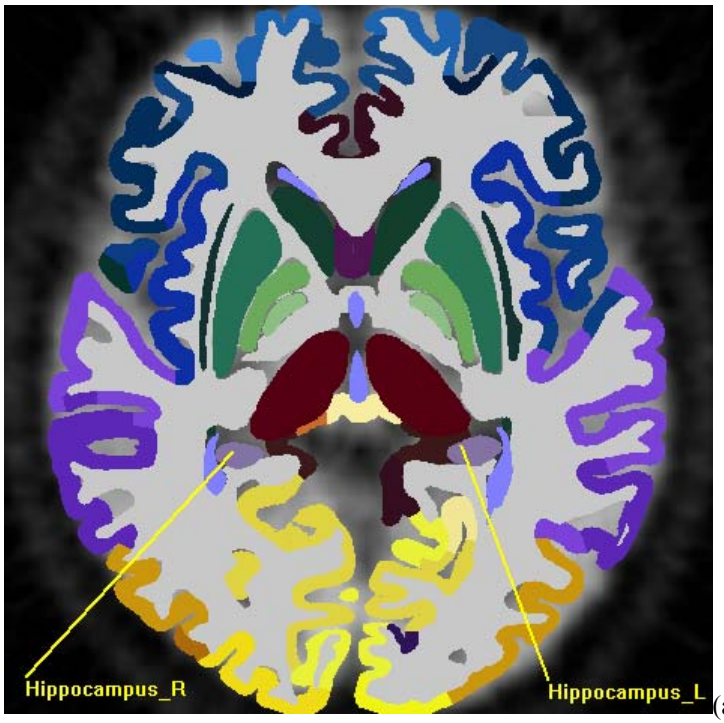

(a)

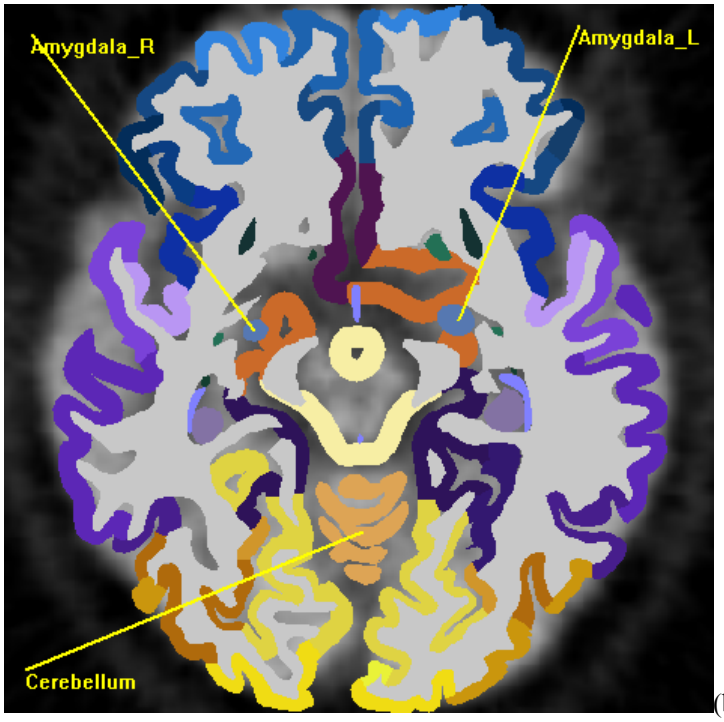

(b)

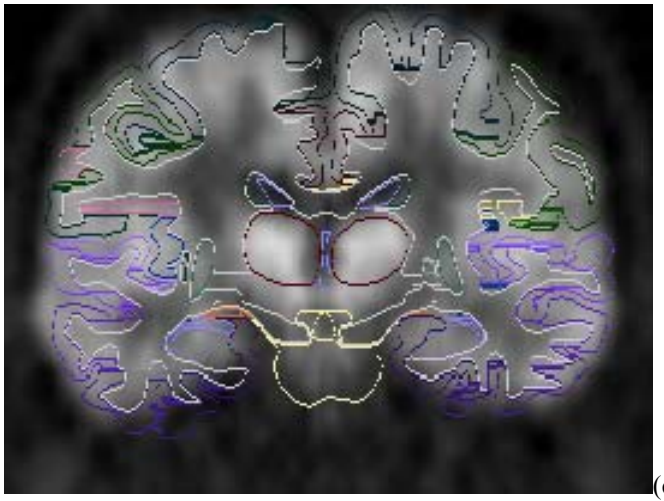
(c)

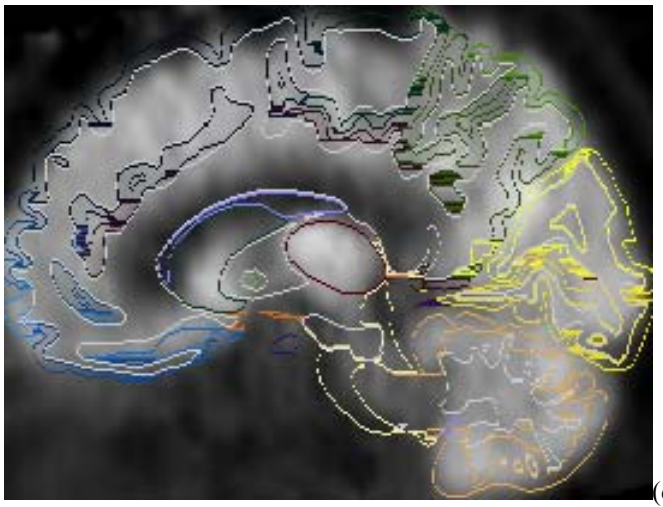
(d)

Figure 31. Atlas warping on FDG-PET images
(a)(b) atlas images warping on axial slices; (c) atlas contours warping on coronal slice; (d) atlas contours warping on sagittal slice

Figure 30 shows examples of original 2D slice, segmented 2D slice, and 3D surface rendering, from a BrainWeb phantom (modality: T1, noise level: 0%, slice thickness: 1mm, intensity non-uniformity: 0%), and IBSR (case 1_24), respectively. Each slice of the images shows the ground truth segmentation (Figure 30c and Figure 30d). However, it gives an incomplete or anatomically incorrect view by rendering the surface in 3D (Figure 30e and Figure 30f).

The sulci are usually the most difficult parts to be segmented properly by automated methods due to partial volume effect. For high resolution images, the results from these automated programs show more obvious inaccuracy, especially by a close view in 3D surface rendering. In addition, some unnecessary objects are segmented, such as the superior sagittal sinus or dura matter. Therefore, the interactive correction is absolutely necessary.

Figure 31 gives an example of the atlas-based applications, which show several images of the atlas warping on the PET images. Figure 31a and Figure 31b show the atlas images on PET axial slices with label texts, Figure 31c and Figure 31d are the merges of atlas contours on coronal and sagittal PET images, respectively.

Despite its advantages the presented platform has some limitations, such as the processing of large datasets is still time consuming, editing the surface directly on the 3D view is not available yet, combination of our contour editor with voxel editing would speed up some operations, conversion from the bitmap segmentation results into contours is still not perfect especially for the complicated structures like gyri and sulci. It needs optimization for better fitting the contours on the edges of the bitmap objects by balancing between the accuracy (requiring a higher number of control points) and time of editing (decreasing with lowering the number of control points).

4.4 Summary

The automated brain extraction methods give the results incomplete or anatomically incorrect. They need interactive correction by editing tools. The presented interactive

platform provides a way for accurate brain segmentation by making use of user friendly tools with rich features and several advantages.

A brand new digital brain atlas is constructed by the presented interactive platform. It provides the features to label the AD-specific structures to assist the atlas-based image processing and statistical analysis on these structures.

Chapter 5

Automated Brain Extraction

In order to process mass neuroimages efficiently and objectively, fully automated methods are needed to segment brain regions from neuroimages. This chapter presents the automatic approaches to extract brain structures from computed tomography (CT) images which usually have less anatomical information and from positron emission tomography (PET) images which usually have lower resolution or contrast. It ends with a summary of the chapter.

5.1 Brain Extraction from CT Images

CT is a medical imaging technique widely used for diagnosis of human brain diseases and injuries like trauma, stroke, tumor and degenerative diseases. Since magnetic resonance imaging (MRI) was introduced in the 1980s, due to higher tissue contrast and better visualization of soft tissues, MRI becomes a superior tool for brain imaging as compared to CT. However, MRI is more expensive, less available and has its limitations to be used on individuals with pacemakers or other metal medical devices. CT, on the other hand, is widely available for examination of neurological diseases due to fast imaging and high resolution.

Brain extraction or segmentation is a crucial component in neuroimage analysis systems and medical imaging applications. Typically, this is the first and essential step before further segmentation and quantification of brain structures. This section presents a new approach to extract the brain automatically from volumetric CT head images. The approach makes use of the full range of the Hounsfield scale for thresholding and region growing to select regions of interest (ROIs) automatically. Thereafter, brain candidates are selected by applying three-dimension (3D) region growing with a variable, anatomy and acquisition-dependent structuring element (SE) to the group of pixels with the Hounsfield units (HUs) of soft tissue. Non-brain areas are removed by applying CT anatomy, domain knowledge and image acquisition parameters.

5.1.1 Problems in CT Image Segmentation

Several issues need to be considered when choosing a method for segmentation of CT head images. Figure 32 gives an illustration of various situations in brain extraction. The skull could be simply extracted by thresholding, as it is clearly visible from bone windowing (shown as white areas in Figure 32). However, the posterior crania are usually surrounded by the head support, which also has high intensities (shown as a U shape region in Figure 32a). In addition, metal artifacts (shown at the left ear in Figure 32b), beam hardening artifacts (shown near the posterior crania in Figure 32c) and hemorrhage with a catheter (shown in the left hemisphere in Figure 32d) may also affect thresholding results. Although intensity thresholding is a simple and effective method, the thresholding value is usually difficult to choose automatically without human intervention.

The intracranial structures inside the skull comprise of grey matter (GM), white matter (WM) and cerebrospinal fluid (CSF). For pathological cases, normal anatomy is

unusually distorted and additional objects may be present in the scan including lesions (e.g., tumors or hemorrhages) and interventional devices (e.g., a catheter). These areas might have close intensity values to those of the skull, GM, WM, and CSF. In such cases, the clustering methods face difficulty in choosing the initial parameters automatically and user intervention may become necessary.

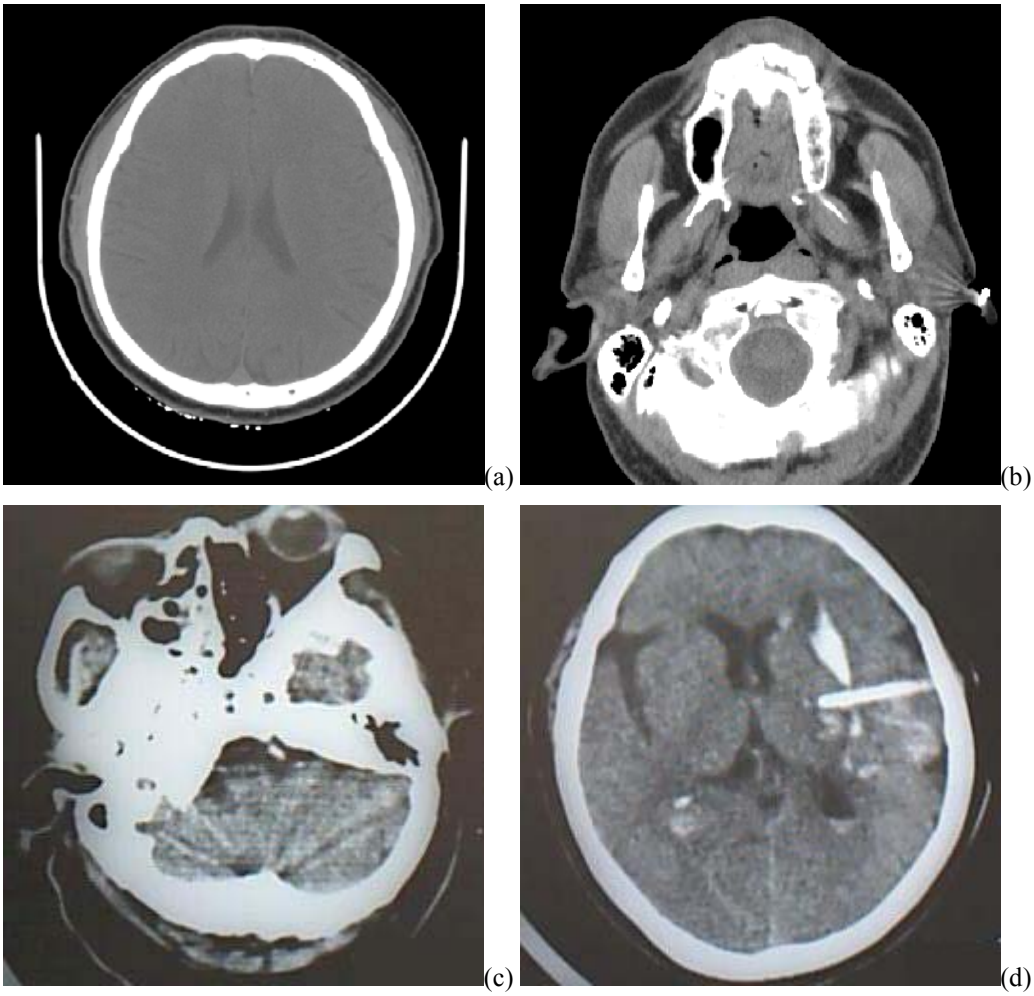

Figure 32. Illustration of various situations in CT brain extraction
(a) head support area; (b)metal artifacts; (c) beam hardening artifacts; (d) hemorrhage with a catheter

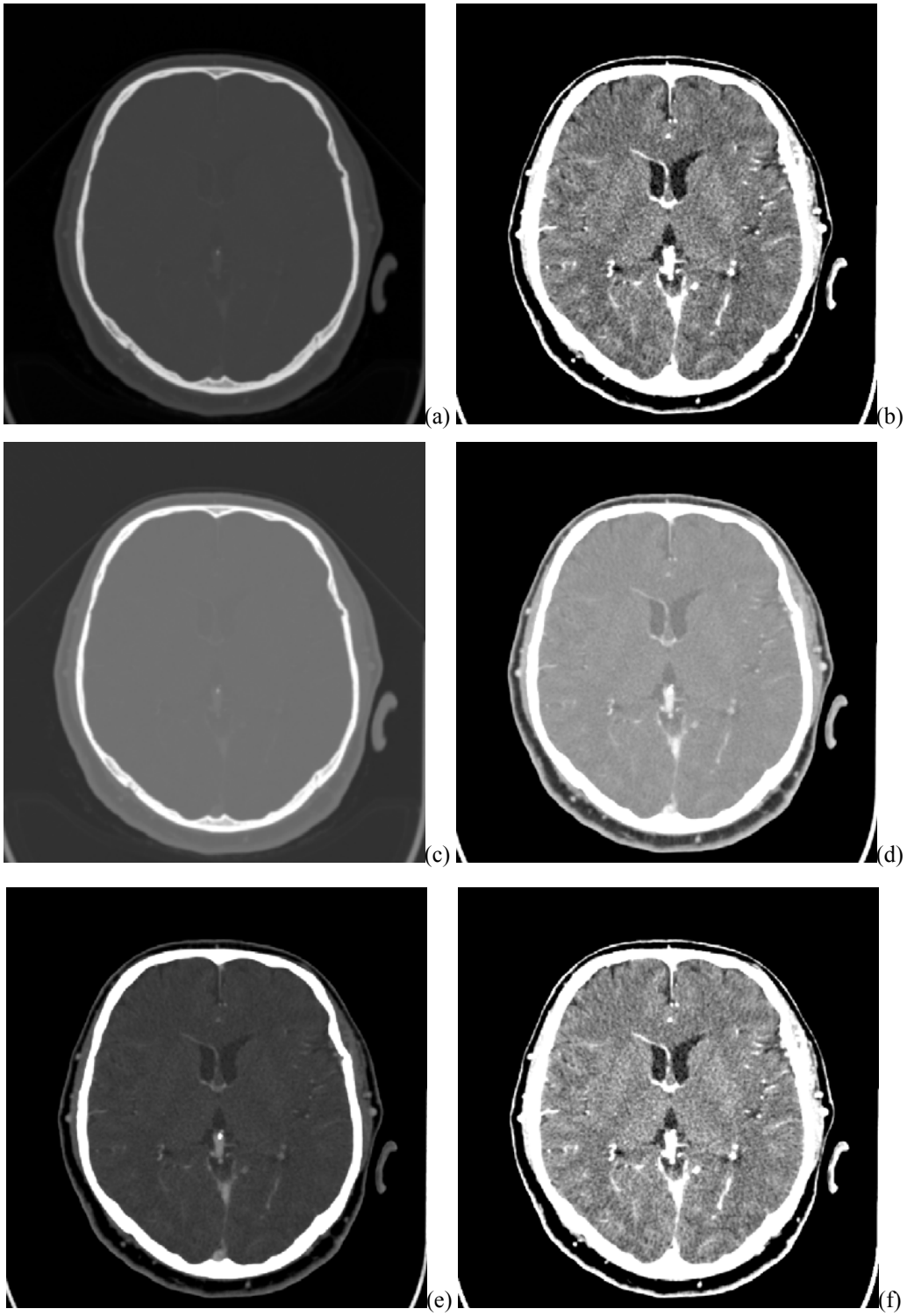

Figure 33. Multiple windowing of CT images

(a) full ranges of HUs; (b) brain window; (c) skull window; (d) soft tissue window; (e) CT angiography window; (f) routinue head window

A modern CT scanner usually acquires 12-bit 4000 or even a greater HU range, but the human eye cannot accurately distinguish the full range of grey levels. To let the physicians or radiologists to interpret the scan, a clinically useful way is the so-called 'windowing', that is to limit the number of HUs to be displayed. Some existing segmentation approaches are mainly based on displayed image intensity. This means that only limited numbers of the entire Hounsfield scale are processed. Although windowing is a practically useful way for human to interpret the CT images, however, it may not be a suitable approach for computer processing because it uses the displayed image intensities in the window instead of the full range of HUs. Figure 33 shows an example of CT slice with the full range of HUs (Figure 33a) and its multiple windowing for brain (Figure 33b), skull (Figure 33c), soft tissue (Figure 33d), CT angiography (Figure 33e) and routine head (Figure 33f). It is evident that the images by applying widowing (Figure 33b to Figure 33f) look clearer than the full range image (Figure 33a) for the human's eyes. However, for a digital computing device, the full range image has much more information than the windowing image.

Due to the absence of anatomic information, it is sometimes difficult to extract human brain areas from CT images efficiently without any user intervention, even for those advanced computer image-processing technologies. The anatomy domain knowledge may become an important hybrid information for the better results of some particular computer algorithms like brain segmentation from CT scans.

5.1.2 Materials for Experiments

Twenty-seven CT scans from different scanners including SIEMENS Sensation 10, GE HiSpeed CT/i, GE LightSpeed 16 and GE Discovery HR were acquired and tested.

The axial slices have resolution of 512 × 512 pixels. The number of slices varies from 17 to 96 and the slice thickness varies from 1.5 to 7.5 mm. They contain some examples of beam hardening artifacts, metal artifacts, partial volume artifacts, and interventional devices such as catheters.

5.1.3 Methods for Experiments

The fully automated approach to extract the intracranial tissues inside the skull makes effective use of adequate HU ranges for thresholding in all the steps. There is no initial parameter setting and no user interaction is required. The regions to be extracted include GM, WM, CSF and pathological areas. Segmentation methods of thresholding, region growing as well as domain knowledge of CT head images are applied. The approach has the following steps:

- ROI selection

  The ROIs are selected by applying the thresholding and region growing operations on bone areas. All subsequent operations are restricted inside the ROIs.

- Group selection

  The whole volume is divided into three groups: background, soft tissue and bone extracted by thresholding. The soft tissue group includes brain tissue and non-brain tissue.

- Brain candidate selection

  A 3D region growing method with a variable and anatomy-dependent SE is applied to generate a 3D connected component. The regions of this 3D component on every 2D slices are added into a list as candidates for further processing.

- Non-brain removal

  The last step is to remove the non-brain areas from the candidate list.

ROI Selection

The objective of ROI selection is to make our method more efficient by restricting the processing areas. Every slice has its own ROI, which is determined as follows.

- Step A. Get a 2D image of superior slice

  Use a very high threshold value (e.g., 800 HU) to generate a 2D binary image of a single superior slice to ensure that the selected pixels above this threshold are part of the skull (bone). The superior slice is positioned at the two-third of the numbers of slices. For example, if the CT scan has 24 slices, the 16th slice from the inferior is selected.

- Step B. Select a seed point for region growing

  Select the first point on the vertical centerline of the image from the anterior direction as the seed point for region growing. This can avoid a potential influence of the head support having a high intensity too.

- Step C. Thresholding

  Use a threshold value (e.g., 110 HU) to apply to the whole scan to generate a volume with pixels above this threshold. This volume contains all bone pixels as well as metal artifacts and interventional devices such as catheter.

- Step D. Generate the largest connected component

  Apply 3D region growing constrained the volume calculated in Step C starting from the seed point selected in Step B to generate the largest connected component. This component is considered to be the crania, connected with other bone areas and/or devices.

- Step E. Determine ROI on each slice

  Automatically set the rectangle border of the largest connected component on each slice as ROI. The subsequent steps ignore all the areas outside these ROIs. Figure 34b shows an example of ROI.

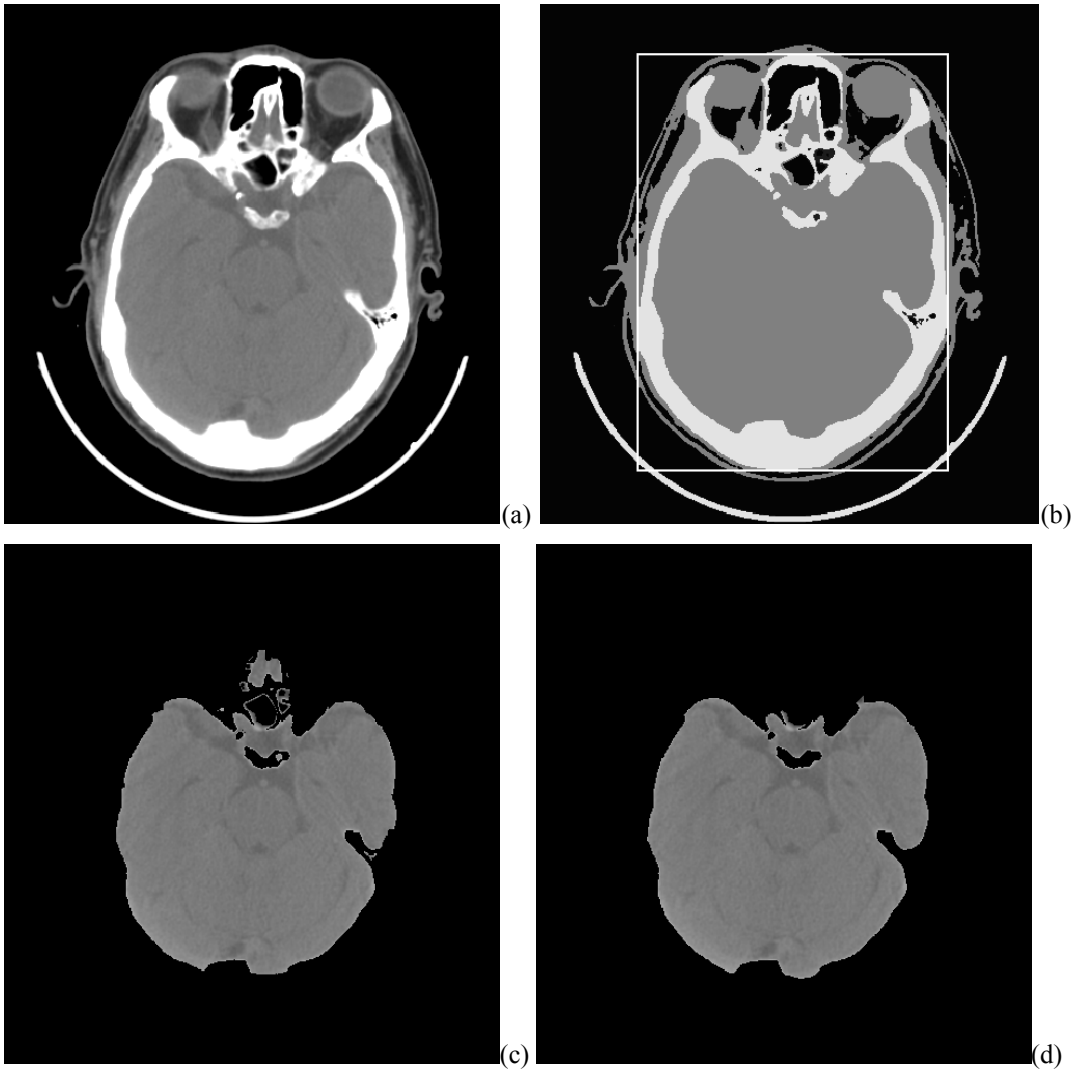

Figure 34. Brain segmentation from CT images
(a) original image with windowing display; (b) ROI selected and image divided into three regions; (c) brain candidates selected; (d) non-brain areas removed

Group Selection

The head consists of bone, soft tissue, CSF, fat and air arranged from high to low CT numbers, i.e. HU. The space inside the skull is the region to be extracted. It is straightforward to divide the whole scan into three groups (background, soft tissue and bone) by selecting two threshold values (e.g., –50 HU and 110 HU). The range between the threshold values is wide enough to contain all brain tissues like GM, WM, and CSF. However, some of non-brain tissues (e.g., fat) are also included. Brain tissues and non-brain tissues are in a same group and the non-brain areas will be removed from it in the subsequent steps. Figure 34b shows a slice after grouping (the background is shown as black, soft tissues are grey and bone is white).

Brain Candidate Selection

The intracranial tissues are anatomically connected in 3D. A 3D region growing method is applied to extract these tissues. Then, the non-brain soft tissues and fat could be possibly included, especially in the areas nearby the eyes. The SE for region growing is supposed to be large enough to let the growing stay inside the crania. We propose a variable SE based on anatomy and voxel size of the CT scan. The size of SE is sensitive especially to the slice thickness and the gap between slices. For the cases with thicker slices, the SE size is smaller. Usually, the region can easily grow outside the crania from the superior orbital fissure (SOF). The SOF is also known as sphenoidal fissure, which is a gap between the roof and lateral wall of the orbit and is bounded by the lesser and greater wings of sphenoid. The size of SOF is about 3 × 22mm [Morard et al., 1994]. For any point $p(x_p, y_p, z_p)$, its operational SE is defined as $S(p)$.

$$
\begin{aligned}
&S(p) = S(p, N_x, N_y, N_z) = S(p, N_x) \cup S(p, N_y) \cup S(p, N_z) \\
&\text{where} \quad S(p, N_x) = \{\, p(x, y_p, z_p) \mid 0 < |x - x_p| \le N_x \,\}, \quad N_x = \frac{C_x}{V_x} \\
&\qquad\qquad S(p, N_y) = \{\, p(x_p, y, z_p) \mid 0 < |y - y_p| \le N_y \,\}, \quad N_y = \frac{C_y}{V_y} \\
&\qquad\qquad S(p, N_z) = \{\, p(x_p, y_p, z) \mid 0 < |z - z_p| \le N_z \,\}, \quad N_z = \frac{C_z}{V_z}
\end{aligned}
\tag{5.1}
$$

where *Cx*, *Cy* and *Cz* are the constants to define the size of SE. As the SOF width is about 3 mm, these constants should be greater than or equal to 3, say *Cx* = *Cy* = 5 and *Cz* = 3. *Vx*, *Vy* and *Vz* are the voxel sizes (millimeter per pixel). *Nx*, *Ny* and *Nz* are the numbers of pixels in length of SE of *X*, *Y* and *Z* direction. The coordinate system (x, y, z) of a volumetric data is: *X* runs from right to left of subject, *Y* runs from anterior to posterior and *Z* runs from inferior to superior. The size of SE is computed as (2*Nx* + 1) × (2*Ny* + 1) × (2*Nz* + 1). Figure 35 shows an example of SE with the size of 7 × 5 × 3 (*Nx* = 3, *Ny* = 2 and *Nz* = 1). Figure 35a is the *XY* orientation of SE, Figure 35b and 35c are the *XZ* and *YZ* orientations. For the centre point marked with × in Figure 35, according to the above definition, its SE consists of all shaded pixels.

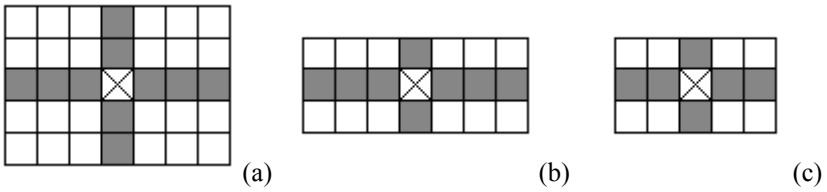

Figure 35. An example of structuring element with the size of 7×5×3
(a) XY orientation; (b) XZ orientation; (c) YZ orientation

The seed point is set on the superior slice, the same selected in the step of 'ROI selection'. The centre point of the ROI is an ideal seed point to start the region growing. The set B, which consists of the candidate regions, is growing every step as follows:

$$
\begin{aligned}
&B_0 = \{\, p_0 \,\} \\
&B_1 = B_0 \cup \{\, p \mid S(p) \subset BS,\ p \in S(p_0) \,\} \\
&B_{k+1} = B_k \cup \{\, p \mid S(p) \subset BS,\ p \in S(p'),\ p' \in B_k - B_{k-1} \,\} \\
&\text{where } k = 1,2,3\cdots\cdots
\end{aligned}
\tag{5.2}
$$

The growing operation is stopped when $B_{k+1} = B_k$. After the region growing is stopped, the set B should be expanded by SE to amend the edge.

$$B = B \cup \{ S(p) \mid p \in B \} \tag{5.3}$$

Figure 34c shows the result of brain candidates, which are calculated as follows:

1. Create a first-in-first-out list L and add seed point P_0 into it.
2. While L is not empty, do the following
   - Retrieve a point P_h from the head of L.
   - Add the point P_h to the set B.
   - Check all P_h's neighbors (Pn) within the set S(P_h) (but not belonging to set B yet). If all points of S(P_n) are in the BS group, P_n is added to L.
   - Remove P_h from L.
3. For every point p in the set B, their SE neighbors S(p) within the group BS are added into set B.
4. The areas in the set B are the candidate regions of the brain.

Non-brain Removal

In order to remove the non-brain tissue from the selected brain candidates, on each 2D slice every connected component from the brain candidate list is determined whether it is the brain or not based on its size. If the connected component is very small, i.e., the number of pixels is less than a predefined value (e.g., 10), it will be removed from the candidate list.

The morphological operation opening is applied to remove the burrs, which are usually occurred nearby the eyes and dilation operation with the SE of 5 × 5 is applied to

amend the corners, which were missed by a large SE in the step 'brain candidate selection'. Figure 34d shows the final result after removing non-brain areas.

5.1.4 Results and Discussion

The algorithmic results are analyzed by comparing to ground truth (GT) and calculating the values of sensitivity, specificity and Dice's index (DI). Sensitivity is the ratio of the total number of true positive (TP) to the total number of TP and false negative (FN). Specificity is the ratio of the total number of true negative (TN) to the total number of TN and false positive (FP). DI is the overlap between the extracted regions and ground truth

$$DI = \frac{2(S \cap G)}{|S| + |G|} \tag{5.4}$$

where S and G are the sets of segmented result and ground truth. TP is the number of voxels present in both segmented brain and GT; TN is the number of voxels present in neither in the segmented brain nor GT; FP is the number of voxels present in the segmented brain but not in GT; and FN is the number of voxels present in GT but not in the segmented brain.

The approach was implemented in C++ and validated by 27 CT scans. The processing time of extracting the brain for a CT scan with a resolution of 512 × 512 pixels varies from three to 17 seconds depending on the numbers of slices (e.g., 3–5 seconds for 17–47 slices and 16–17 seconds for 96 slices). For 5 of 27 cases, the GT has been generated by a neuroanatomy expert. The other cases were visually checked with satisfactory results. Figure 36 shows four slices (Figure 36 left) of a scan from inferior (Figure 36a) to superior (Figure 36d) and the corresponding extracted images (Figure 36 right). Figure 37 displays the 3D surfaces of the extracted brain (Figure 37a) and its GT

(Figure 37b), generated by the Marching Cubes algorithm [Lorensen and Cline, 1987]. It shows an excellent match between the extracted and ground truth surfaces (some very tiny differences are on the basal surface only). Table 6 provides sensitivity, specificity and DI of five cases.

Table 6. Test results of brain extraction from CT Images

Case	GT Volume (cm^3)	Segment Volume (cm^3)	Sensitivity	Specificity	Dice's Index
1	1103	1143	99.9%	98.7%	98.1%
2	1399	1420	99.9%	99.6%	99.1%
3	1360	1393	99.8%	99.3%	98.6%
4	1772	1758	98.7%	99.9%	99.1%
5	1345	1371	99.9%	99.5%	98.9%
Average	-	-	99.6%	99.4%	98.7%

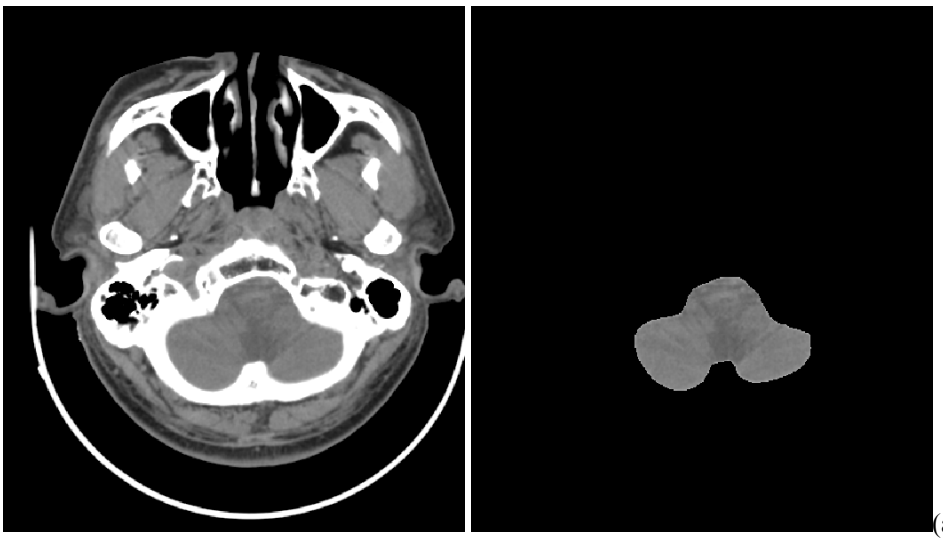
(a)

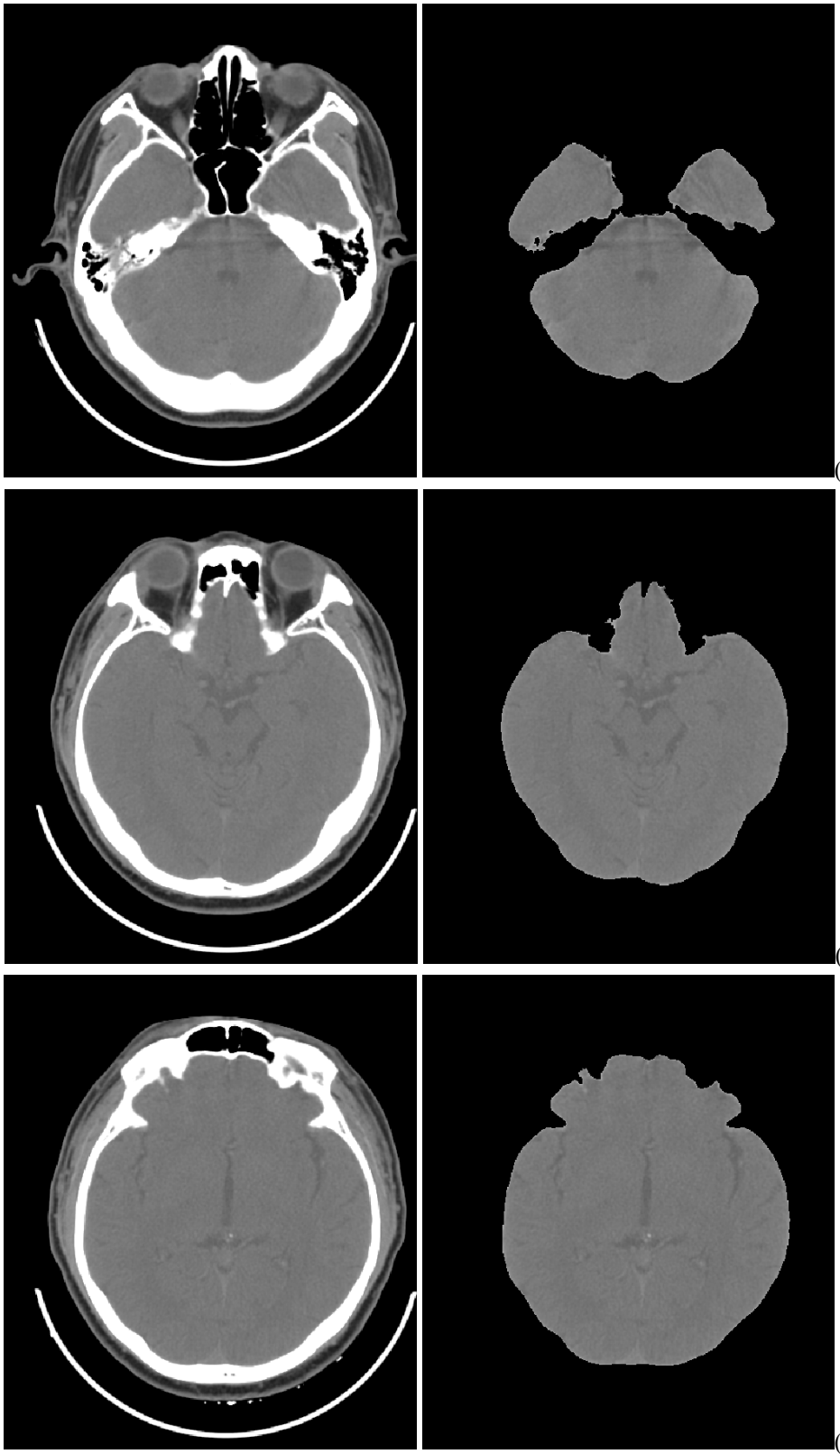

Figure 36. Examples of original slices and the corresponding extracted images

(a) – (d): slices from inferior to superior

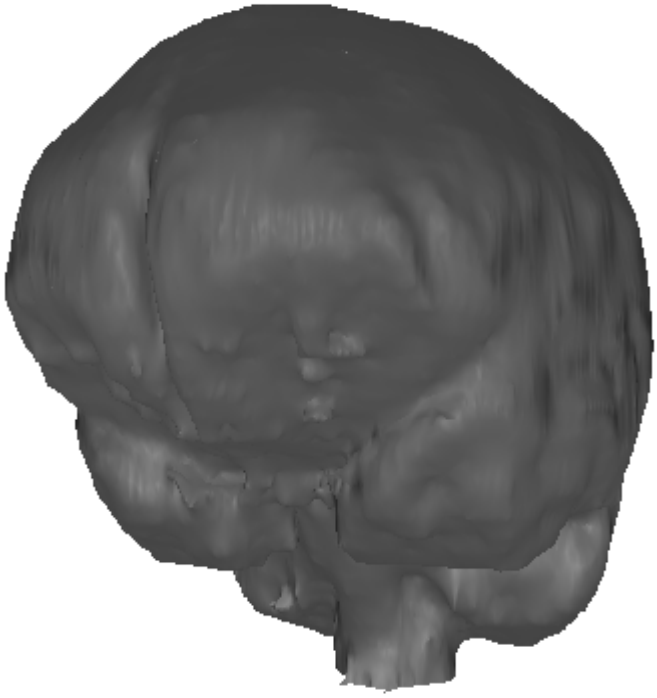

(a)

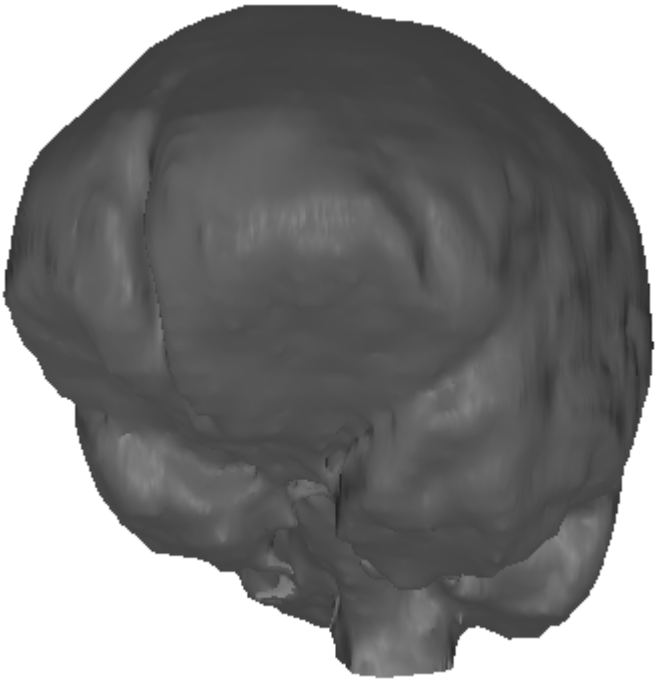

(b)

Figure 37. Three-dimension brain surfaces

(a) extracted brain; (b) ground truth (for case 4 inTable 6)

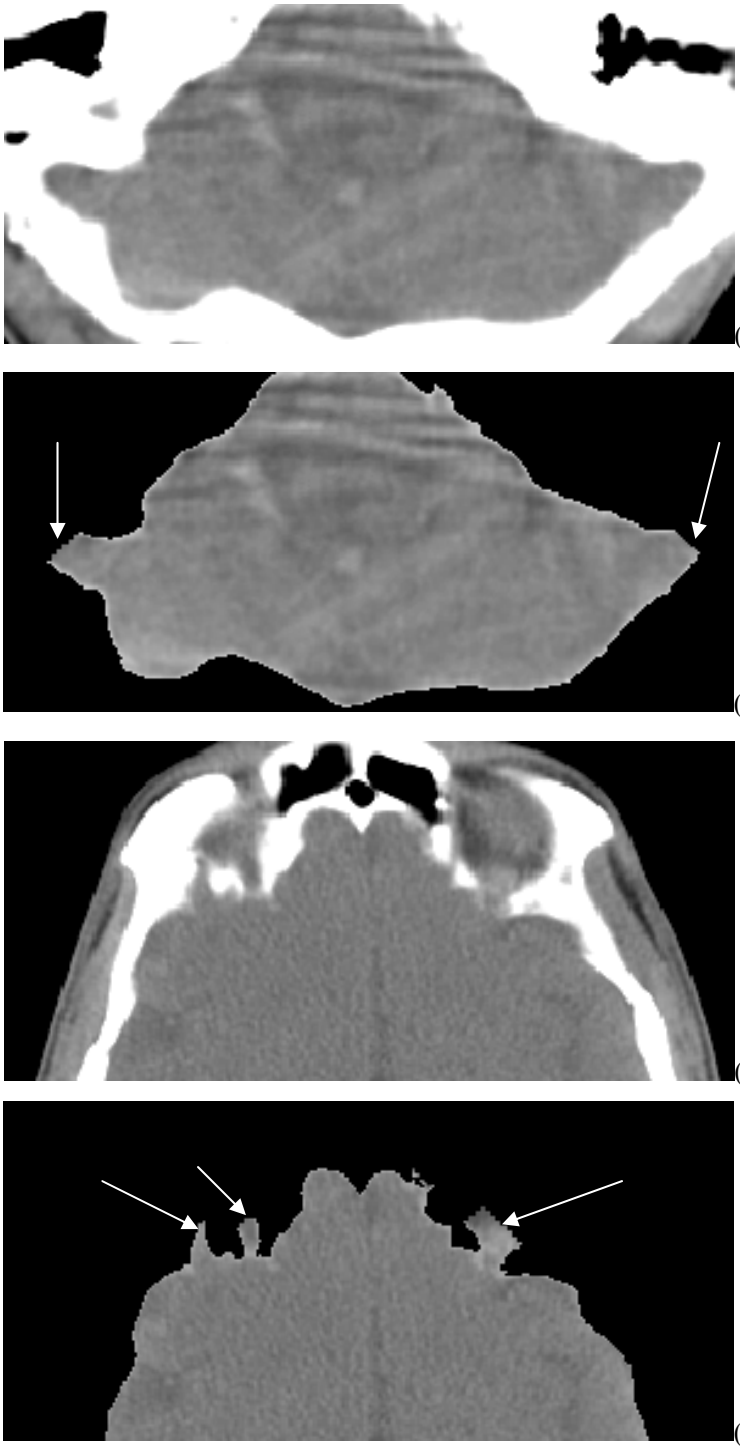

Figure 38. Cases of under-segmented and over-segmented brain areas (a and c) original CT images; (b) slight under-segmented cerebellum (pointed to by the arrow) due to a large SE; (d) over-segmented brain areas (indicated by the arrows)

For the region growing approach, the skull openings may cause growing to 'leak' outside the crania. Besides SOF, these openings include foramen magnum, foramen ovale, foramen spinosum, foramen lacerum and jugular foramen. A large SE can avoid it to happen because it can ensure the region growing to remain inside the crania. However, if the SE size is too large to reach the sharp corners of brain images, the corner areas may be under-segmented (Figure 38a and b). The morphological dilation operation could amend some of them, but the side effect is that some non-brain areas could be enclosed (Figure 38c and d). In this case, some additional rules may be applied to resolve it. Practically, there is no leakage observed and no serious under-segmented situation happened for all 27 cases tested. The SE size is well balanced based on the anatomy information such as the slice thickness and the size of SOF.

5.2 Brain Extraction from PET Images

Segmentation of the brain areas from PET images is a basis for many applications, e.g. registration with the images of other modality like MRI or CT, quantitative analysis of brain cortex and brain anatomical structures, volumetric symmetry analysis, and pathology detection, etc. Due to a limited spatial resolution and a low signal-noise ratio of FDG-PET images, automated brain extraction from those images is still a challenging task. This section presents a new approach to segment the brain regions from FDG-PET images automatically.

5.2.1 Methods for Experiments

The approach for brain extraction includes four steps. They are 1) histogram graph generation; 2) peak value selection; 3) threshold value determination; and 4) region growing.

Histogram graph generation

In FDG-PET images, the regions of the cerebrum and cerebellum have brighter intensities than the areas around or outside the crania (Figure 39a-b). The histogram graph is created by counting the number of voxels with the same intensity values in the whole volumetric images. It is a frequency distribution in which the widths are proportional to the intensities, and the heights are proportional to the frequencies of the intensity values. It is often used for density estimation. Figure 39c-d show the graphs with a smoothed histogram of the images of Figure 39a-b, by cutting off the highest peak of background for illustration purpose.

Peak values selection

There are two situations about the histogram graph by observing all the cases to be processed. The first situation is that the histogram graph has two peaks (Figure 39c), besides a highest peak of the image background. It occurs about 97% of all cases (219 of 226). The other 3% (7 of 266) has only one peak (Figure 39d).

- Two peaks on the histogram graph indicate the areas inside the crania and the areas around the crania (Figure 39e), and
- One peak to indicate the areas inside the crania (Figure 39f).

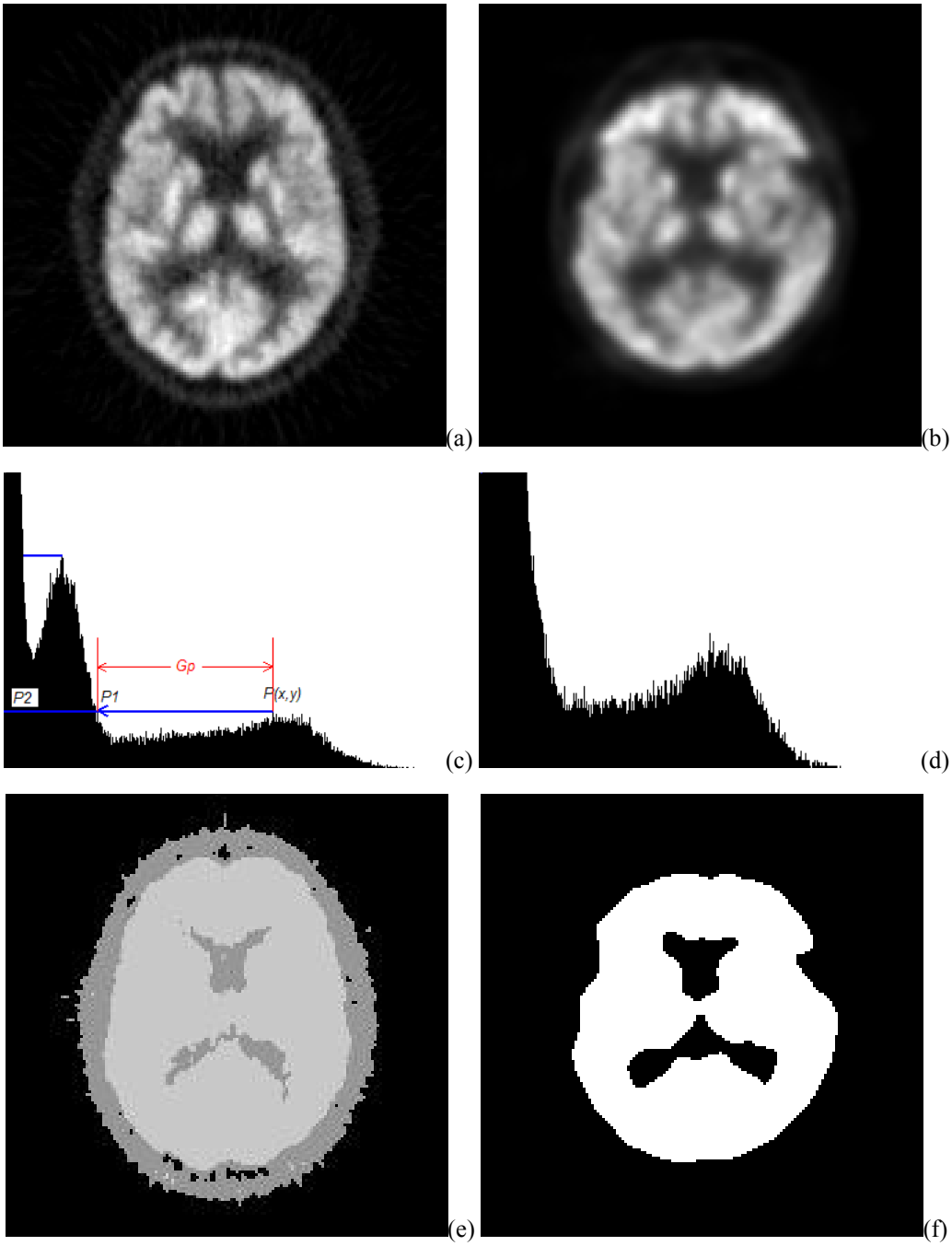

Figure 39. Histogram graphs with two peaks and one peak
(a)(b) original images; (c)(d) histogram graph; (e)(f) segmented results based on the threshold values selected on histogram graph

In either situation, the peak points are selected by calculating the intensities gap *Gp* between current point *p* and nearest point p_1 which has same number of voxels. There may be many points with same number of voxels (in Figure 39c, all the points on the line

from p_1 to p_2). In such case, the nearest point p_1 from point p is selected, and the intensity gap Gp is the difference of intensity values of p and p_1. For example at the histogram graph of Figure 39c, let us consider X as the horizontal axis of intensities and Y as the vertical axis of the number of voxels which have same intensity values. The intensity gap value Gp at position p is defined as

$$G_p = P_x - \max\left(P_{x(i)}\right), \text{ where } i < x \text{ and } P_{y(i)} = P_y \tag{5.5}$$

where i is the position on X axis, $Px(i)$ is the intensity value of i, $Py(i)$ is the vertical height of i on the histogram graph, max is to calculate the maximum value of all i values which meet the defined conditions.

After calculating the G values for all intensities, the point with the largest G values is selected as the peak point for the situation which has only one peak. For the situation which has two peaks, the point with the largest G value and the point with the second largest G value are selected as peak points. The threshold values will be determined based on these selected peak points in the subsequence step.

Threshold value determination

The peak point at the rightmost hand of the histogram graph (point p_1 in Figure 40a) indicates a class of pixels with higher intensity values, i.e. the pixels of the brain cells. Another peak point p_2 indicates the non-brain or background pixels. In order to largely segment two classes of brain and non-brain pixels, the deepest point in the valley (point p in Figure 40a) is selected as the threshold value. The point p is also the highest point of the convex (Figure 40b), as well as the longest distance towards two peak points (p_1 and p_2). To locate the highest point of convex, the orthogonal lines of the peak line ($L\ p_1\ p_2$) are drawn to have two intersection points, p and p'. The point p is the intersection with

the histogram graph, and the point p' is the intersection with $L\ p_1\ p_2$. The set of all the distances between p and p', for all the points on the line $L\ p_1\ p_2$, is defined as

$$D = \{d_i(pp'),\ \ x_1 < i < x_2,\ \ p' \in L_{p1p2}, \text{and } L_{pp'} \perp L_{p1p2}\} \tag{5.6}$$

where *di(pp')* is the distance between the points p and p', *x1* and *x2* are the x-axis positions of point *p1* and *p2*, $L\ p_1\ p_2$ and *Lpp'* are the lines of points *p1* and *p2*, and points p and p'.

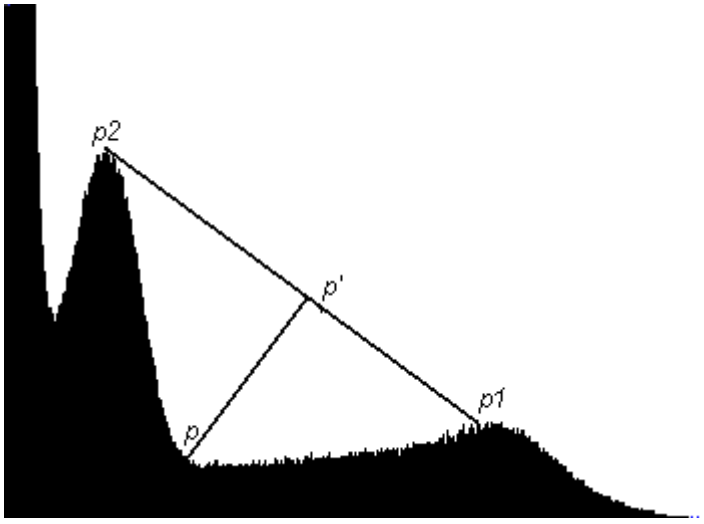

(a)

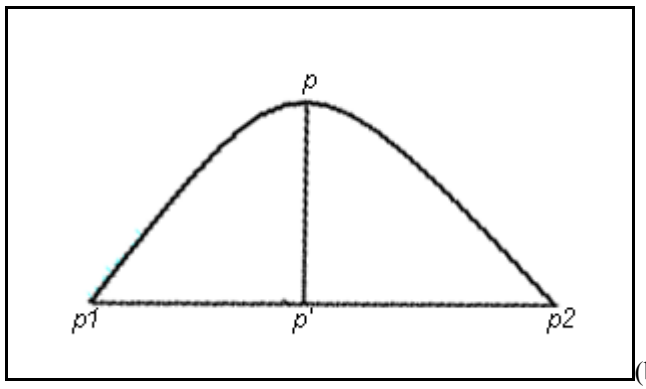

(b)

Figure 40. Selection of threshold value

(a) smoothed histogram graph; (b) highest point on the convex border

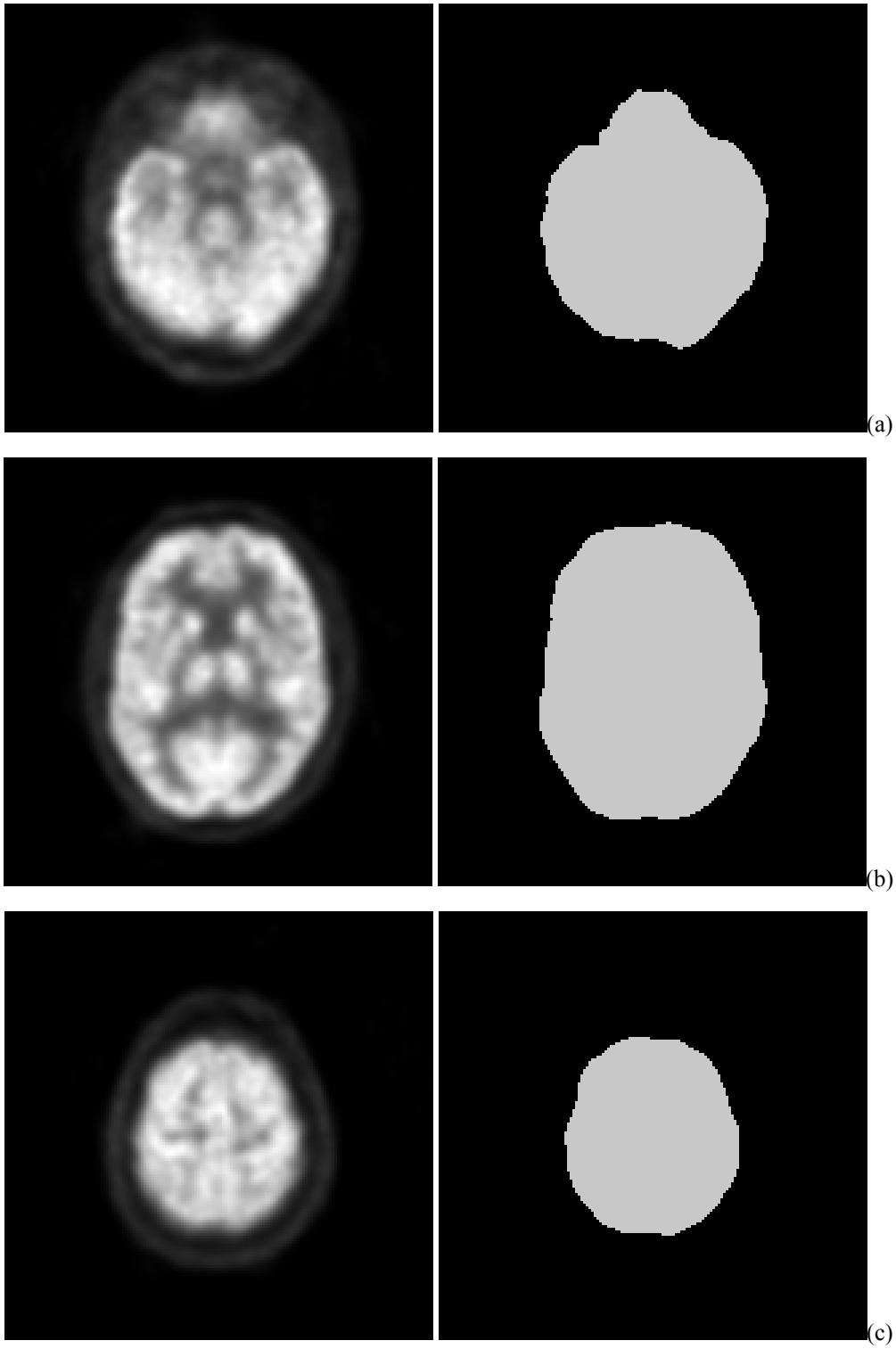

Figure 41. Examples of brain extraction from PET images
original brain images (left) and their extracted areas (right). (a) an inferior slice; (b) a middle slice; (c) a superior slice

The corresponding *x* value of the point, whose *di(pp')* value is maximum in the set *D* from equation (5.6) is the threshold value to segment the FDG-PET image into two parts: brain area and non-brain area. Based on the selected threshold value, the binary mask images are generated.

Region growing

Thresholding segmentation may leave some isolated points or small areas and may have holes inside the brain area. It is necessary to remove those isolated areas and fill those holes to complete the areas or volume inside crania. A 3D region growing algorithm is applied to do so as the brain area is considered as a largest connected component. The seed point for region growing is the center of the volume. If it happens to be the non-brain voxel, one of its brain voxel neighbors is automatically selected. The growing goes in three directions at the same time and complete until no more brain voxel added. Several large holes (non-brain areas) inside the crania like ventricles need to be also filled. Instead of locating these areas one by one, an efficient way is to apply the region growing algorithm to the non-brain area outside the crania. The seed point can be any one on background area, e.g. (0, 0, 0). Figure 41 shows the examples of three slices (left) and their extracted areas (right) from inferior slice (Figure 41a) to superior slice (Figure 41c).

5.2.2 Results and Discussion

A total of 226 cases with a resolution of 160×160×96 voxels of size 1.5 mm^3 were tested. The average processing time was 3.03 seconds per case. The approach has been validated on all the cases qualitatively and 10 cases quantitatively. The quantitative

validation cases had the brain areas manually segmented from the original FDG-PET images and had the midsagittal lines manually drawn on the images for comparison with the results of the automatic method. Table 7 provides the segmented results with sensitivity, specificity and Dice's index (DI). Due to a high cost of quantitative validation, the result section only lists 10 cases of the comparison results with the automated processing. For these 10 cases, a total of 960 images were manually drawn one by one with contours for brain area extraction.

Table 7. Test results of brain extraction from PET images

Case	Manual (cm^3)	Auto (cm^3)	Sensitivity (%)	Specificity (%)	DI (%)
1	1143.86	1316.99	99.53	98.87	96.66
2	1234.17	1393.21	99.91	97.73	93.86
3	1305.84	1488.07	99.26	97.25	92.78
4	1426.10	1709.43	99.96	95.87	90.93
5	1443.07	1503.79	94.76	98.01	92.81
6	1273.56	1402.64	99.70	98.09	94.85
7	1312.25	1446.03	99.78	98.04	94.94
8	1105.62	1151.40	98.40	99.12	96.41
9	1622.35	1374.41	82.47	99.45	89.30
10	1570.25	1635.64	98.54	98.69	96.53
Average	1343.71	1442.16	97.23	98.11	93.91

Thresholding is probably the most popular method for image segmentation. However, thresholding method usually needs a user to input some initial parameters to select the threshold values based on the histogram or clustering. For neuroimages like MRI, CT, or PET, it is still a challenging task to determine the threshold value automatically due to artifacts, partial volume effects, and inhomogeneity of the volumetric scans. Advanced or complicated segmentation methods like level set, watershed, or model-based methods usually mean a higher cost of calculation, but does not mean the higher accuracy

especially for the images with lower contrast like FDG-PET. For example, the software SPM requires several minutes to process a single PET scan. Since the results are warped into a template space, it is difficult to get the correlated information back on the original images.

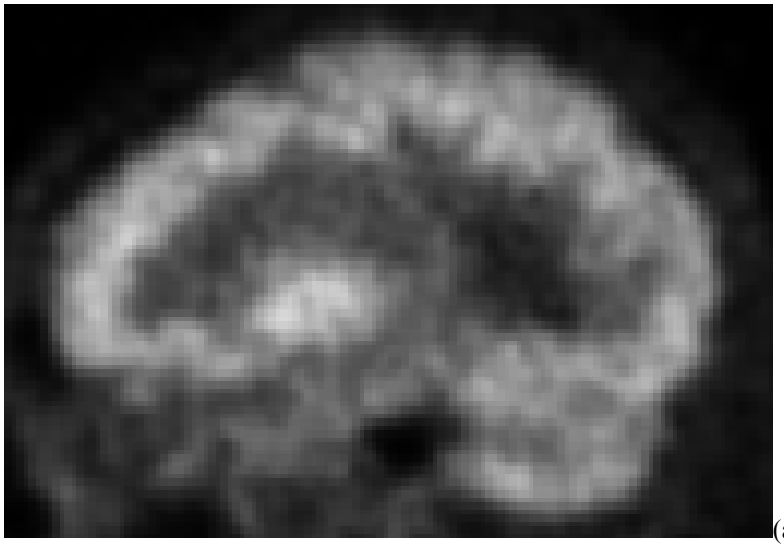

(a)

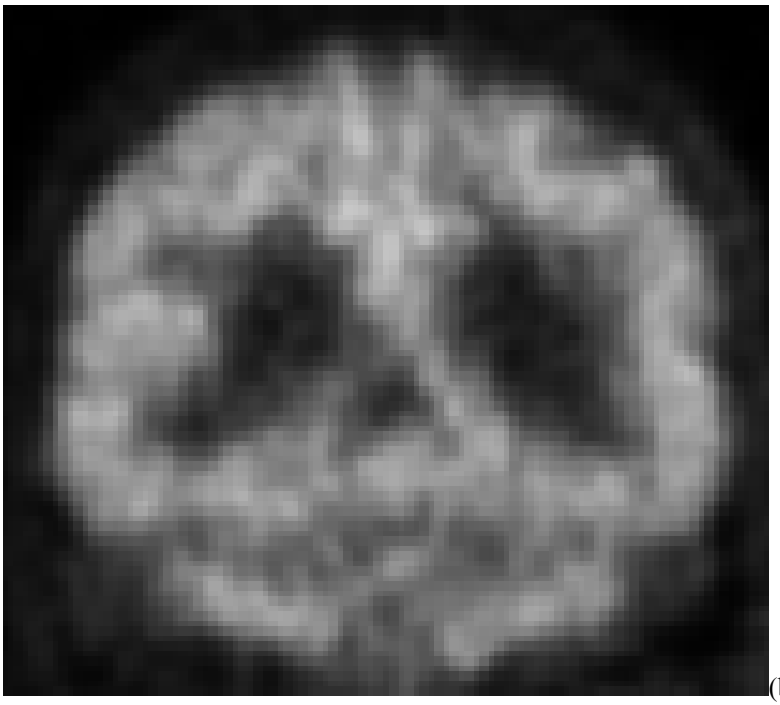

(b)

Figure 42. Examples of difficult cases for brain extraction from PET images (a) more intensive noise near the temporal lobe; (b) brainstem connected with cerebellum

Because of the properties of FDG-PET, computer programs face difficulties to distinguish several non-brain areas from the cerebrum or cerebellum. For examples, the inferior part of the brain usually has more noise near the regions of temporal lobes (Figure 42a); there is no significant difference of intensities between the brainstem and other parts of brain, and the brainstem on images is often connected with the cerebellum (Figure 42b). It is difficult not only for a computer program but also for a human without anatomical knowledge to segment them. The predefined or known anatomical information, e.g. the normal brain size, related positions of structures, etc. may play an important role for neuroimage processing.

The presented approach has several limitations. First, if the images have serious partial volume effect, those affected voxels are difficult to be classified into brain or non-brain areas. It may also face problems even for an experienced expert to manually segment the low resolution images like FDG-PET. Second, to speed up the processing time, the approach makes use of the histogram of the whole volume. However, for the cases with serious inhomogeneity between the slices, this method may cause false segmentation results. In such cases, the histogram of each slice may be helpful.

5.3 Summary

Two automated brain extraction algorithms are presented in this chapter for structural CT images and functional PET images, respectively. They are usually the initial step of image processing for subsequent components about further analysis and data interpretation. For CT head images, thresholding and region growing are applied to select seed point and generate binary images. A 3D region growing with a variable, anatomy

and acquisition-dependent structuring element size is used to generate brain candidates. Prior domain knowledge such as Hounsfield unit ranges, image position (superior slice or inferior slice), size of orbital/nerves canals, slice thickness information, and morphological operations are applied. For PET head images, histogram graph, thresholding, region growing, and morphological operations are applied to extract the brain from a volumetric FDG-PET dataset.

Chapter 6

Landmark Extension and Detection

The accuracy of scan-to-atlas registration highly depends on the number of landmarks and the precision of landmark identification. This chapter presents an extension to the modified Talairach landmarks. It starts with the definition of the extended landmark, followed by the methods to detect the landmarks on positron emission tomography (PET) images. It ends with a summary of the chapter.

6.1 Landmark Extension

This section gives the objective of the landmark extension and the definition of new landmark, the cerebellum inferior.

6.1.1 Objective of Landmark Extension

The Talairach transformation is one of the most commonly used methods to normalize human brains based on the Talairach landmarks. As fluoro-deoxy-glucose (FDG) PET images are difficult to detect the brain structures automatically or even manually, landmarks on the images play an important role for the accuracy of data

normalization and localization analysis. Since the cerebellum is the structure less affected by Alzheimer's disease (AD), it is an ideal reference region to normalize the other structures, e.g. the hippocampus and amygdala, which may be seriously affected by the disease. However, a problem with the Talairach approach is that the second largest structure of the brain, the cerebellum which is located at the metencephalon within the cranial cavity, is not well-defined in the Talairach space. Part of the cerebellum is inside the 3D proportional grid system, but the inferior of the cerebellum is outside and no landmark is defined for cerebellar in the Talairach space. Therefore, applications which need to operate on cerebellar images or transform scan images into an atlas space may need a new landmark of cerebellum for the higher accuracy. The additional landmark can increase the degree of freedom for the Talairach transformation, and brain warping techniques with high degrees of freedom may naturally provide much better results.

6.1.2 Cerebellum Inferior

The most inferior point of the cerebellum, as shown in Figure 43, is defined as a new landmark: Cerebellum Inferior (CBI). It is the point of intersection of three planes: 1) the midsagittal plane, 2) the coronal plane passing through the most superior (most dorsal) point of the cerebellum, and 3) the axial plane passing through the most inferior (most ventral) point of the cerebellar cortex. By adding the CBI landmark, both the cerebrum and cerebellum are included into the Talairach space as shown in Figure 44. The Talairach grid system is increased to 18 cuboids by 9 landmarks (as opposed to the original 12 cuboids by 8 landmarks).

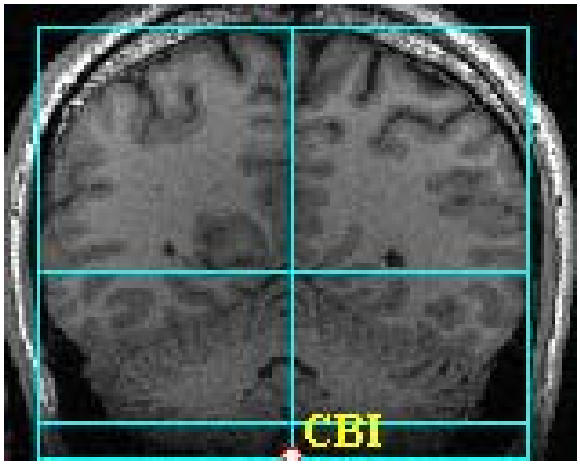

Figure 43. Cerebellum inferior on a coronal slice

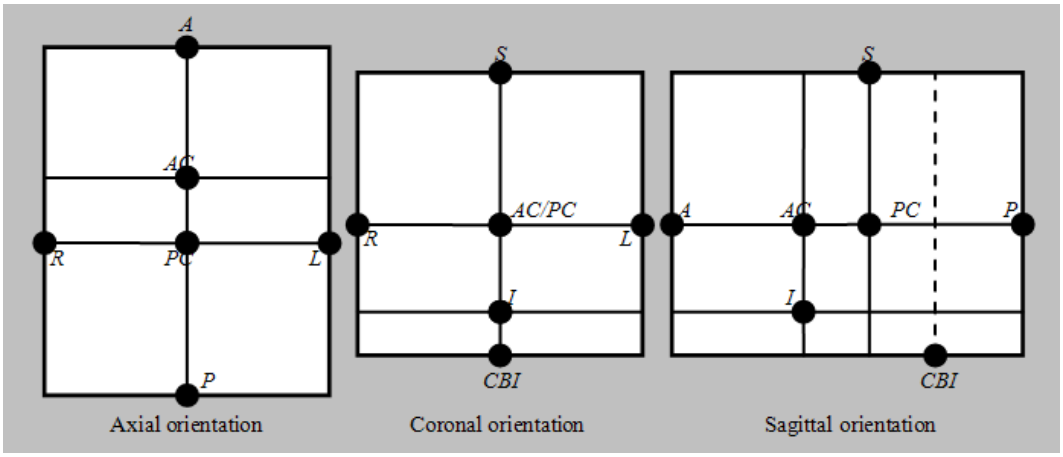

Figure 44. New grid system with landmarks

6.2 Midsagittal Lines Identification

The midsagittal line (MSL) on an axial slice is the separating line of left and right brain hemispheres. A symmetry index [Hu and Nowinski, 2003], which was successfully applied to magnetic resonance imaging (MRI) for midsagittal plane (MSP) detection, needs to be modified and extended to calculate the symmetry of brain cortex of FDG-PET images rather than the areas near the interhemispheric fissure, in order to avoid the areas

which have less glucose uptake than brain cells (e.g. ventricles). There are three steps to detect the MSL on an axial slice:

- MSL candidate selection
- Symmetry Index calculation
- MSL determination.

6.2.1 MSL Candidate Selection

MSL is supposed to be an almost vertical line, with some rotations if the images are rotated while scanning, or some shifted from the center if the images are shifted during scanning. The range of rotations or shifts has their limits, e.g. the rotation not more than 40º. The candidates are chosen and the number of MSL candidates (*Nc*) is calculated by the following steps (Figure 45a):

- The middle vertical line is the first candidate (*Nc*=1);
- The middle line is shifted to the left by λ pixels, e.g. $\lambda = 1$, for *Ns* times, e.g. *Ns* = 10;
- The middle line is shifted to the right by λ pixels for *Ns* times (*Nc*=1+*Ns*×2);
- Every vertical line is rotated to the left by θ degrees, e.g. $\theta = 2$, for *Nr* times, e.g. *Nr* = 10;
- Every vertical line is rotated to the right by θ degrees for *Nr* times (*Nc*=(1+*Ns*×2) ×(1+*Nr*×2)).

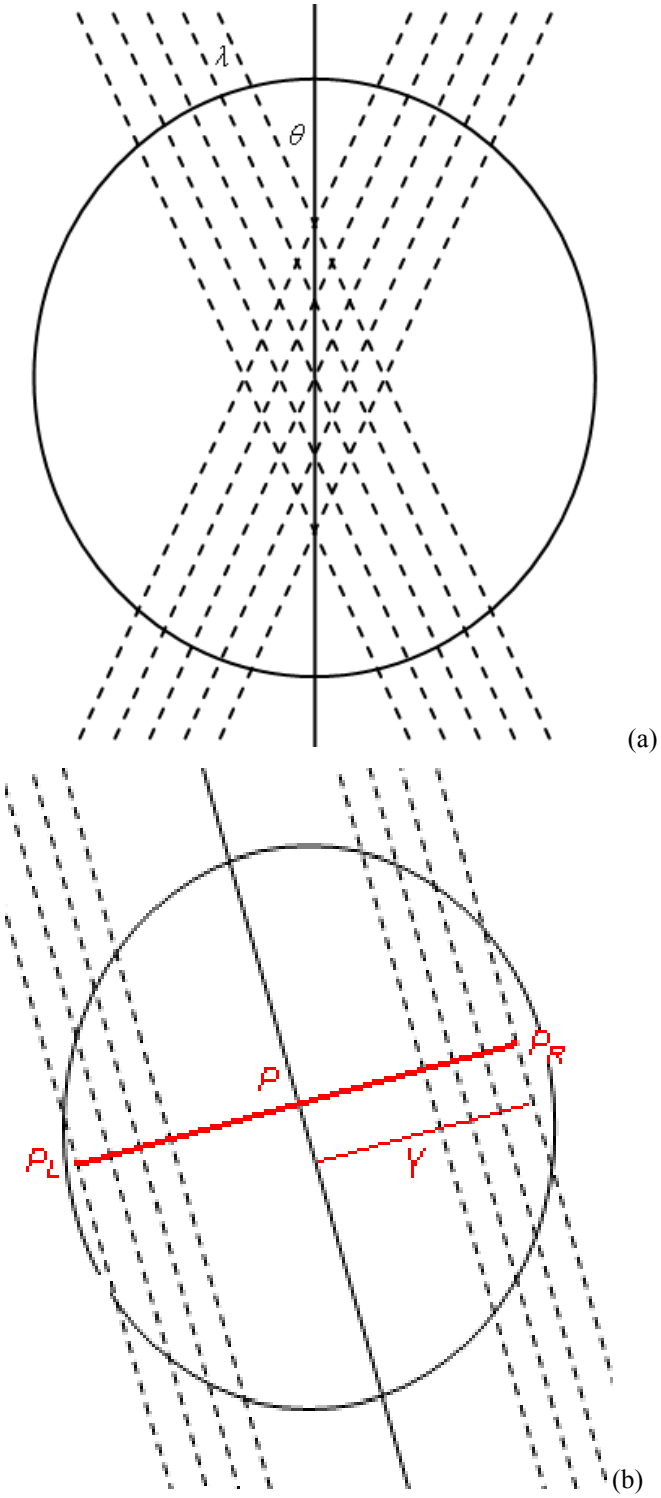

Figure 45. Midsagittal line detection

the candidate lines; (b) calculation of symmetry index

6.2.2 Symmetry Index Calculation

A total number of *Nc* candidates are chosen to calculate their symmetry index (*SI*) values. For each candidate line (*CL*), *SI* is defined as an average of the sum of the difference between the left and the right of the *CL*. The calculation of *SI* is defined as,

$$SI(\theta,\gamma)=\frac{\sum_{1}^{H}\sum_{1}^{Np}\left|V(P_L)-V(P_R)\right|}{(Np\times H)} \tag{6.1}$$

where *H* is the height of the image, *Np* (e.g. *Np* = 4) is the number of pairs of the parallel lines which have same distance (γ) to the *CL*. $V(P_L)$ and $V(P_R)$ are the intensity values of the mirrored points P_L and P_R on the parallel lines (Figure 45b). Their coordinates are defined as

$$P_{L,R}(x,y)=(Px\mp\gamma\cos\theta, Py\mp\gamma\sin\theta) \tag{6.2}$$

6.2.3 MSL Determination

The line with minimum SI from a group of candidates is selected as the MSL. The results of brain extraction and MSLs are shown on an inferior slice (Figure 46a), a middle slice (Figure 46b), and a superior slice (Figure 46c).

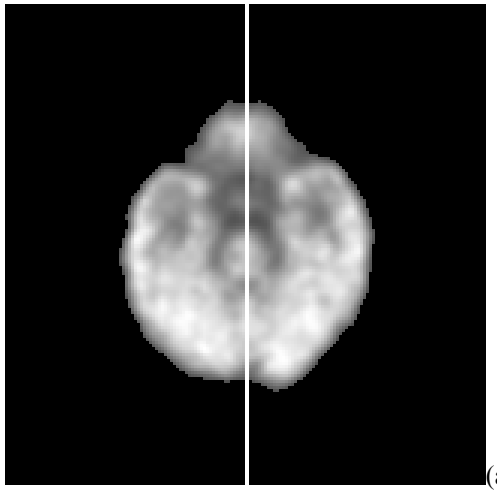

(a)

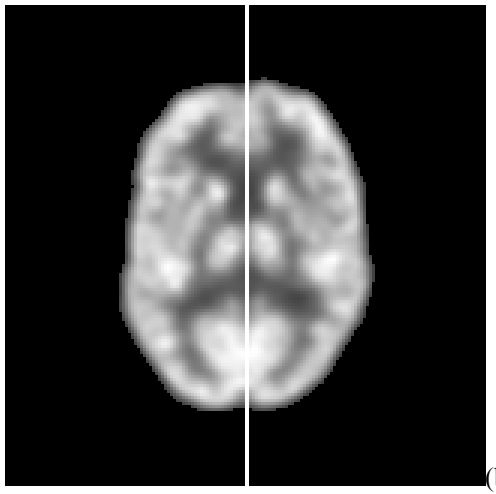

(b)

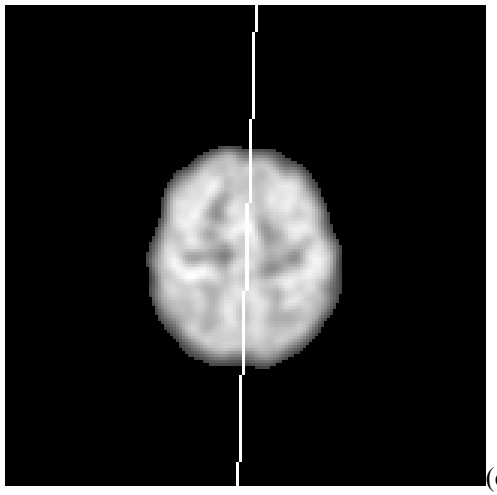

(c)

Figure 46. Midsagittal lines on the selected axial slices
(a) inferior slice; (b) middle slice; (c) superior slice

6.3 Landmark Detection

This section comprises two parts of the landmark detection, including 1) the modified Talairach landmarks identification and 2) the CBI placement, on FDG-PET images.

6.3.1 Modified Talairach Landmark Detection

The modified Talairach landmarks are detected by four steps. They are: 1) detection of the AC-PC line (APL) on MSP; b) determination of L, R, A, P landmarks on the AC-PC plane; c) determination of the AC position and the I landmark on the coronal plane passing through AC; and d) determination of PC position and the S landmark on the coronal plane passing through PC.

Detect AC-PC line on MSP

The APL is an intersection line of MSP and AC-PC plane, which is a perpendicular plane to MSP and passes through both the AC and PC. The detection of the APL is the first and important step to extract the AC-PC plane and affect the results of the subsequent steps to detect all the landmarks. Since FDG-PET images lack structural information, it is difficult to detect the anterior commissure and posterior commissure structure on the images directly, as well as the AC and PC landmarks. An alternative way to estimate the APL from MSP is to detect the longest line from anterior to posterior (Figure 47) on the MSP image with the skull removed. Even though the exact positions of the AC and PC are still uncertain, they are determined later by the inferior and superior landmarks according to the modified Talairach space.

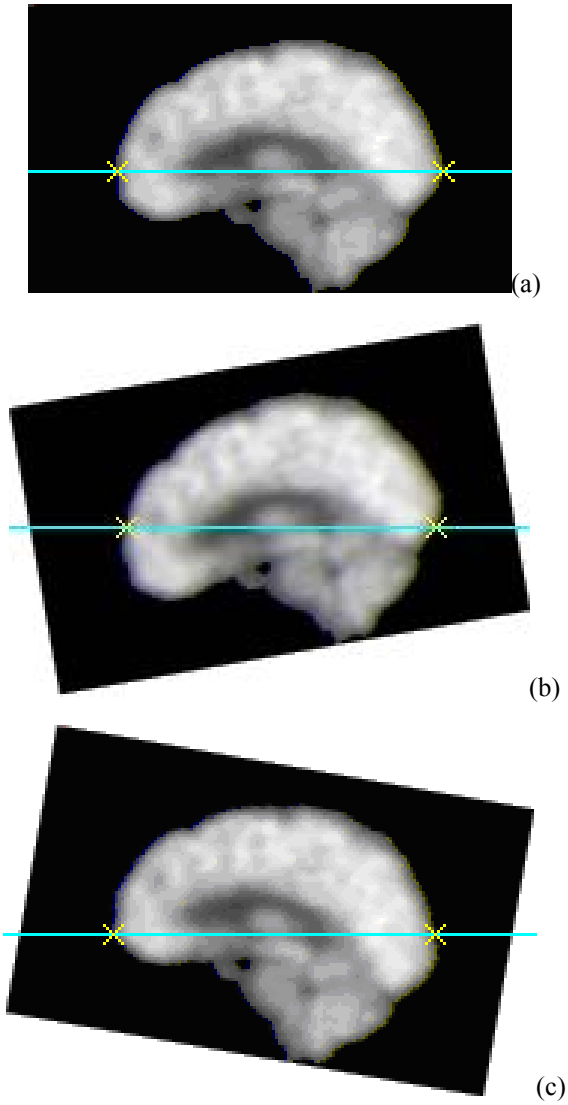

Figure 47. AC-PC line on MSP and rotated MSP images
(a) MSP; (b) MSP with 10º counterclockwise rotation; (c) MSP with 10º clockwise rotation

The algorithm of detecting the longest line from MSP is to search the projections from both anterior and posterior directions. On a 2D image of the MSP (Figure 47), the searching is from both the left and the right of the image. Since the APL has its anatomical position within human brain, the proportional scaling in the Talairach space (e.g. the distance between A and P is 174mm, the distance between S and the APL is 74mm, and the distance between I and the APL is 43mm) is applied to the search

algorithm. After the detection of the longest horizontal line, the MSP image needs to be rotated through a degree of λ (e.g. 10º) to find out the longest line from non-horizontal direction. It can be done by a loop of rotating the image from – λ to + λ. Figure 47b is the rotated image of Figure 47a with 10º counterclockwise, and Figure 47c is the image of 10º clockwise rotation.

Determine L, R, A, P on AC-PC plane

The AC-PC plane (Figure 48) is extracted from volumetric data based on APL and the skull-removed brain of previous work (refer to Chapter 5 for the details). The algorithm to determine the L and R landmarks is to select the extreme left point and extreme right point as L and R landmarks by searching the lines parallel to the MSP. Similarly, to determine the A and P landmarks, the extreme anterior point and extreme posterior point are selected by searching the lines perpendicular to the MSP. Figure 48 shows an AC-PC plane with L, R, A, P landmarks identified.

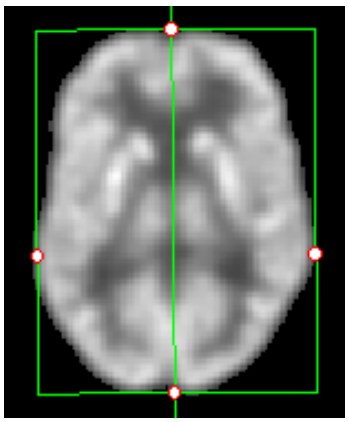

Figure 48. AC-PC plane with L, R, A, P landmarks

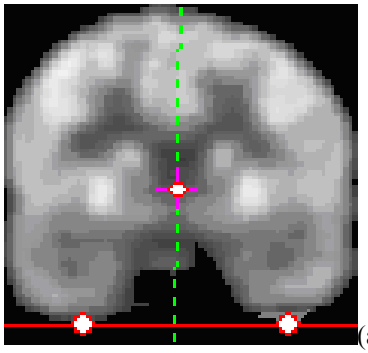
(a)

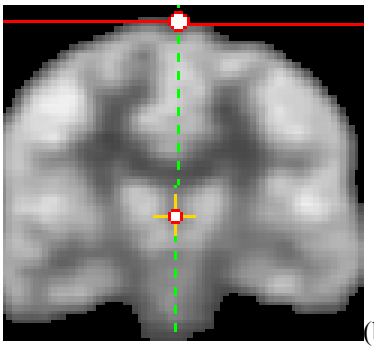
(b)

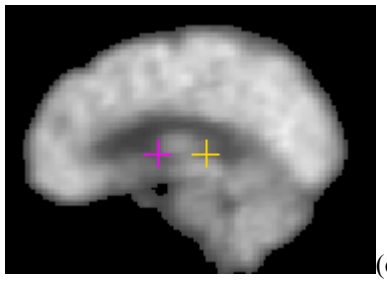
(c)

Figure 49. I, S, AC and PC landmarks on PET images
(a) I landmark on VAC; (b) S landmark on VPC; (c) AC and PC on MSP

Determine I and AC

In the Talairach space, the length from anterior to posterior is 174mm. The distances from anterior to AC and PC are 70mm and 94mm, respectively. According to the definition of the Talairach space and the positions of A and P, the AC and PC positions are estimated by proportional scaling. They are marked as eAC and ePC. The coronal slices near eAC (e.g. ± 5mm) are selected as the candidates of VAC. By calculating the most inferior point on all VAC candidates, the VAC is identified and the AC is also determined at the same time. Figure 49a shows an example of I on VAC.

Determine S and PC

Similarly, the coronal slices near ePC (e.g. ± 5mm) are selected as the candidates of VPC. By calculating the most superior point on all VPC candidates, the VPC is identified and the PC is also determined at the same time. Figure 49b shows an example of S on VPC, and Figure 49c shows the AC and PC on the MSP.

6.3.2 Extended Landmark Detection

A coronal slice passing through the most superior point of the cerebellum is called VCB. The extended landmark CBI will be located by the following steps: a) estimate the position of VCB (eVCB) and select the candidates of VCB; and b) Locate CBI from the candidates of VCB.

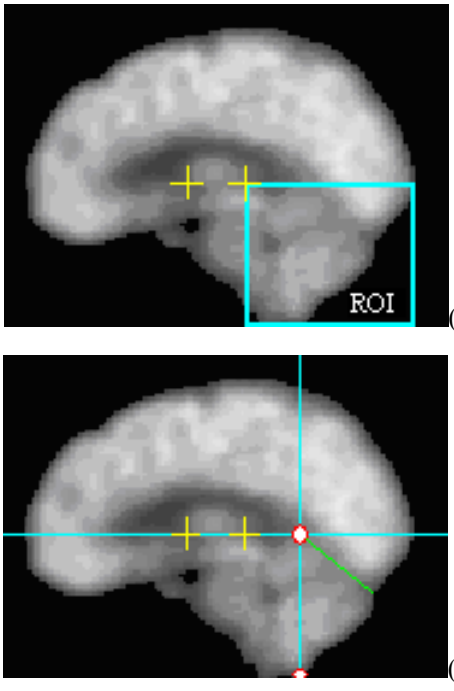

Figure 50. Estimated VCB plane
(a) definition of ROI; (b) calculation of GCL

Estimate the eVCB and select the candidates of VCB

In order to estimate the position of VCB, a transverse fissure cerebellar tentorium, is detected first. It is located between cerebrum and cerebellum [Van De Graaff, 2001]. According to the FDG-PET image property of that the cerebrum and cerebellum have a much greater glucose uptake values than the other fissures [Wang et al., 2007; Zincirkeser et al., 2007], the fissure between the cerebrum and cerebellum is detected by the following steps:

1) Define a region-of-interest (ROI) for faster detection of cerebellar tentorium. The ROI of X-axis starts from PC and ends at P. The ROI of Y-axis starts from the APL and ends at the bottom of MSP image. All the processing and calculation below are restricted within this ROI (Figure 50a).

2) Define a glucose consumption line (GCL), starting from the top edge of ROI, ending at the cortical surface of brain.

$$y = tg\theta \times (x - x_0) \tag{6.3}$$

where θ is the angle between GCL and X-axis, and x0 is the position on AC-PC line.

3) Calculate the sum of glucose consumption on GCL.

$$S(x_0, \theta) = \sum GCL(x, y, x_0, \theta) \tag{6.4}$$

where x and y are the coordinates of GCL on the MSP image.

4) Locate a GCL with the minimum sum of glucose consumption GCLmin.

The estimated point for VCB (eVCB) is identified as the cross point of GCLmin and APL (Figure 50b). The coronal slices passing through and nearby eVCB (e.g. 3mm) are selected as the candidates of VCB.

Locate CBI from the candidates of VCB

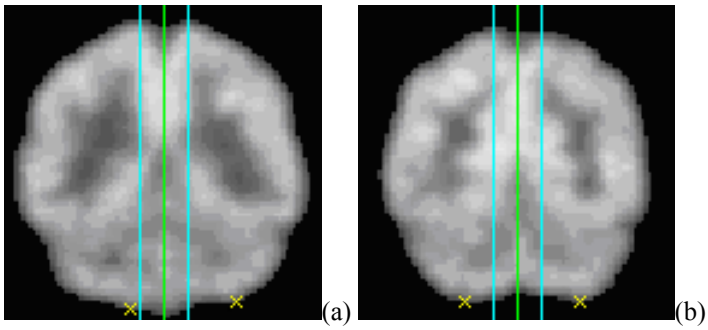

Figure 51. Areas of brainstem and vermis
(a) brainstem area excluded; (b) vermis area excluded

The cerebellum has two hemispheres connected by the vermis. There are two conditions need to be considered while calculating the lowest part on coronal images, as shown in Figure 51. The most inferior bottom points of cerebellum are lower than the vermis and higher than the brainstem. As the size of brainstem is wider than that of vermis, the width about 7mm is excluded from both hemisphere sides for calculation of the cerebellum bottom. Figure 51a shows an example of coronal slice with brainstem which is lower than the cerebella bottom, and Figure 51b shows the example of coronal slice with vermis which is higher than the cerebellum bottom. The CBI is located by performing the following steps:

- Exclude the areas which may contain the brainstem and vermis from the coronal images.
- Detect the lowest part on both hemispheres and calculate the average.
- Find out a slice with lowest average value of the cerebellar hemispheres. The slice is VCB, and the most inferior point on VCB is the landmark CBI.

6.4 Experiment Results and Discussion

For MSL detection, a total of 226 cases with a resolution of 160×160×96 voxels of size 1.5 mm^3 were applied to validate the algorithm qualitatively, and 10 of them were validated quantitatively. The quantitative validation cases had the MSLs manually drawn on the images for comparison with the results of the automatic method.

Table 8. Test results of MSL detection

Case	Angular difference (°)	Center displacement (mm)
1	1.09 ± 0.87	0.43 ± 0.01
2	1.25 ± 0.89	0.41 ± 0.01
3	0.87 ± 0.48	0.23 ± 0.01
4	0.95 ± 0.93	0.58 ± 0.15
5	1.47 ± 1.12	0.05 ± 0.03
6	1.12 ± 0.95	0.70 ± 0.26
7	0.39 ± 0.74	0.10 ± 0.04
8	0.71 ± 0.89	0.20 ± 0.07
9	1.17 ± 1.74	0.29 ± 0.11
10	0.29 ± 1.02	0.00 ± 0.00

Table 8 provides the mean values and the standard deviations of the angular difference (Da) and the center displacements (Dc) of comparing the automated MSL detection and the manual method. No significant statistical difference was observed. The Da is defined as the angle between two lines L and L′ (Equation 6.5). L (ax+by+c=0) is the MSL line detected automatically, and L′ (a'x+b'y+c'=0) the line manually drawn. The Dc is defined as the distance of the center points of lines L and L′ (Equation 6.5).

$$\begin{aligned} Da &= \left| arc\cot\left(-\frac{b}{a}\right) - arc\cot\left(-\frac{b'}{a'}\right)\right| \times 180 \div \pi \\ Dc &= \left| \frac{b \times H + 2 \times c}{2 \times a} - \frac{b' \times H + 2 \times c'}{2 \times a'} \right| \end{aligned} \tag{6.5}$$

where $a \neq 0$, $a' \neq 0$, and H is the height of the image.

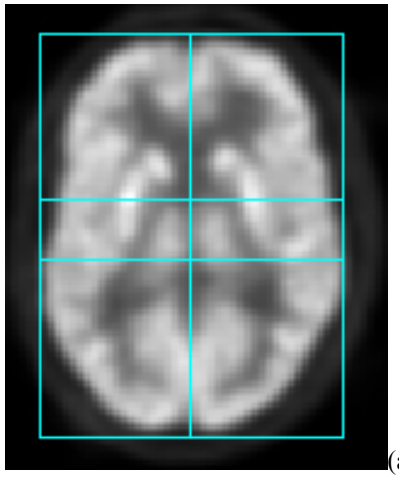
(a)

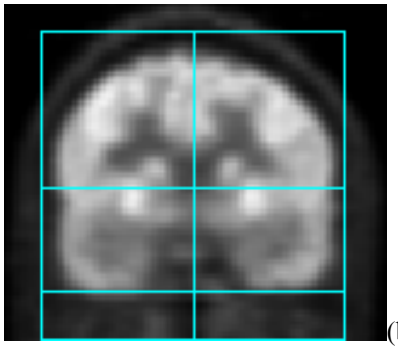
(b)

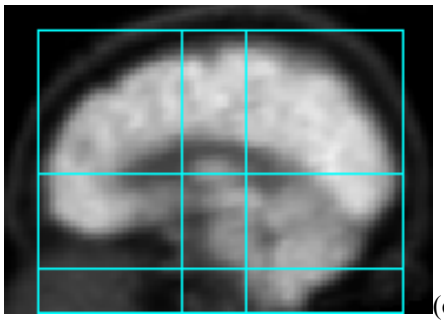
(c)

Figure 52. An example of FDG-PET images with landmark grid
(a) grid on axial slice; (b) grid on coronal slice; (c) grid on sagittal slice

For landmark detection, a total of 49 cases were applied to validate the algorithm. The average processing time of landmark detection was 2.78 seconds per case running on a standard personal computer with 2.4 GHz CPU. Fifteen of those cases have the landmarks manually placed by a neuroanatomy expert for comparison with the results of the automatic method. Figure 52 gives an example of grid by detected landmarks on three

orientations of FDG-PET images. The other cases were visually checked with satisfactory results.

Table 9. Test results of landmark misplacement (mm)

Case	AC	PC	L	R	A	P	S	I	CBI
1	1.15	2.53	1.25	0.43	0.75	1.14	0.82	1.14	3.36
2	2.09	2.45	0.98	0.89	0.67	0.17	0	1.12	0.09
3	0.8	0.8	0.58	0.24	0.39	0.22	0	2.66	0.71
4	0.32	2.01	0	0	1.73	0.94	1.5	1.53	0.23
5	0.8	0.8	1.92	0.25	1.65	0.47	1.13	0.38	1.69
6	2.56	3.31	0.7	0.04	0.66	0	0.5	1.49	2.23
7	1.73	2.48	2.27	2.07	0.11	0.3	0	0.75	0.62
8	1.15	1.55	0	0	0	0	0.5	1.49	1.73
9	1.45	1.44	0	0.96	0	0	2.09	1.82	0.99
10	1.36	0.55	0.26	1.15	0.57	0.54	0.13	1.11	0.73
11	1.17	1.17	0.99	0	1.25	1.38	1.13	2.89	0
12	1.45	2.37	0.51	0	0.53	0	1.33	1.08	1.12
13	1.66	1.45	0	0	0	0	0.09	2.55	0.49
14	0.74	0.47	0.74	0.59	0.36	0.03	0	5.72	2.38
15	0.94	1.31	0.57	0	0	0.44	0.46	1.49	1.12
min	0.32	0.47	0	0	0	0	0	0.38	0
max	2.56	3.31	2.27	2.07	1.73	1.38	2.09	5.72	3.36
μ	1.29	1.65	0.72	0.44	0.58	0.38	0.65	1.81	1.17
σ	0.32	0.71	0.47	0.36	0.33	0.2	0.44	1.66	0.9

Table 9 lists the differences of 15 cases, and their minimum and maximum values, mean (μ) and the standard deviations (σ) of the displacements of comparing the automated landmark identification and the manual method for the modified Talairach landmarks AC, PC, L, R, A, P, S, I, and CBI. The differences of the AC and PC are calculated by:

$$D = \sqrt{(Xa - Xm)^2 + (Ya - Ym)^2 + (Za - Zm)^2} \tag{6.6}$$

where (*Xa*, *Ya*, *Za*) and (*Xm*, *Ym*, *Zm*) are AC or PC coordinates of automated approach and the ground truth values, respectively. The differences of other landmarks are the absolute difference value of ground truth and automatic approach. From the result table, no significant statistical difference was observed.

The Talairach transformation is probably the most prevalent method for spatial normalization of neuroimages. It is a 3D piecewise linear operation which accuracy may not be good as non-linear registration or transformation methods such as iterative methods and boundary-based methods. However, the non-linear transformation methods have their own limitations and difficulties to be accepted by clinical applications. The major practical limitation is a prohibitive price of computational time. Comparing to the Talairach transformation, which can be in real time performed on a standard personal computer without additional memory or other accelerators, the non-linear transformation methods are not acceptable to process a large number of cases in a fully automatic way. Therefore, the Talairach transformation is still playing an important role in data-atlas registration because of its conceptual simplicity and anatomic nature, especially for the PET images.

Since the accuracy of the Talairach transformation is generally inferior to those non-linear transformation methods, it is helpful to improve it by adding more landmarks. The Talairach space is well-defined for the human cerebrum. If the additional landmark is within the cerebrum, the improvement may be limited too. Otherwise, if the additional landmark is outside the cerebrum, e.g. cerebellum, it is helpful for the applications which need the cerebellum scanned and processed. Theoretically speaking, if there are enough landmarks for linear transformation, the accuracy is close to that of non-linear methods.

Because of the properties of FDG-PET, computer programs face difficulties to identify the actual or exact positions of landmarks. They may make use of the predefined or known anatomical information, e.g. the normal brain size, related positions of AC and PC, etc. to guess or estimate the positions of landmarks. The landmarks which are robust to be identified are usually detected earlier than those are difficult to be determined. The experience shows, in FDG-PET images, the AC-PC line (APL) and superior landmark S are more robust to be identified than the inferior landmark and the cerebellum landmark due to the more noise near the regions of temporal lobes and the join of cerebellum and brainstem. Based on the robust-identified landmarks and anatomical information, other landmarks are able to be estimated to reduce the search ranges.

The presented methods have several limitations. For MSL detection component, if the MSL is far away from the searching areas, e.g. rotated more than 40º from the vertical line or shifted more than 20 pixels from the image center, the algorithm may fail or give an inaccuracy results. For landmark detection, it is sensitive to the results of brain extraction and MSP detection from FDG-PET images. If the non-brain tissues are included into the brain areas, six subcortical landmarks may become farther from the image center. In addition, the dependency of landmarks may cause failure of other landmark identification. For example, if the APL is wrongly or inaccurately detected, the subsequent steps for AC, PC, S, I landmark detection may cause unexpected results. The presented method works only on the completed scan images of whole brain. If the cerebellum is not scanned and included, the CBI landmark may possible be wrongly identified superior to the landmark I, which means the failure of CBI detection.

6.5 Summary

A set of the Talairach landmarks is extended to include the cerebellum into the Talairach space and grid system. This chapter presents a fast and fully automatic approach to identify those landmarks from FDG-PET images. The algorithm has been applied to all the cases and shown promising results. Based on these landmarks, a fast Talairach piecewise linear transformation is applied to warp the PET images into the standard Talairach space for further statistical analysis.

Chapter 7

Automatic Alzheimer's Disease Assessment

This chapter addresses the process and techniques of statistical analysis including the stepwise regressions to assess the cognitive scores and discriminant classification to categorize the subjects into different groups automatically. It starts with an introduction of the correlation between Alzheimer's disease (AD) diagnoses and the cognitive score systems as well as the functional changes on neuroimages. It explains the materials of experiment subjects including the normal subjects and patients with AD and mild cognitive impairment (MCI). Thereafter, it presents the methods to assess the cognitive scores of the patients and classify them with AD or MCI from normal subjects based on the neuroimages by statistical analysis. The chapter ends with a discussion and summary of the presented methods.

7.1 Problems in Automatic AD Assessment

As discussed in Chapter 2, currently the cognitive score systems like the mini mental state examination (MMSE) and clinical dementia rating (CDR) are conventional tools for

cognitive assessment and diagnose AD or MCI. The diagnosis is time-consuming and subjective, and needs professional knowledge as well. Many research papers demonstrated that the scores are correlated with the changes on structural and functional neuroimages of AD-specific structures or regions. Neuroimaging techniques provide the possibility to investigate the human brains in vivo by visual inspection or quantitative analysis of brain structures with computer technologies. Computed tomography (CT) and magnetic resonance imaging (MRI) are widely used imaging tools to discover and compare the structural changes and assist disease diagnosis. However, for neurodegenerative diseases like AD, the structural changes of an affected brain are too subtle to be visible or detected on the CT or MRI images at the initial stage of the disease. Positron emission tomography (PET) provides the information about blood flow or metabolism during the scanning in any part of the brain. The hypometabolism is observed in several regions of the brain in AD or MCI.

It is a challenging task to build a relationship quantitatively between the changes on neuroimages and the cognitive scores, due to the multiple impacts of cognitive scores such as language, orientation, etc. as well as the multiple factors of neurological changes of the brain such as structure atrophy, brain cell hypometabolism, etc., shown in Figure 53. For instance, the atrophy of the hippocampus may cause memory problem of a patient and have lower MMSE scores than those of normal subjects. But it is difficult to determine which factors in the MMSE score system and how many percent of the scores are affected. For a large number of cases which have both cognitive scores and the changes on neuroimages, statistical analysis is a feasible solution to build the correlation and establish the relationship between them by constructing several equations or functions. In the next sections, the methods of automatic cognitive assessment and diagnosis classification are presented. The regression equations were constructed from the

stepwise regressions to assess the cognitive scores, and the discriminant functions were generated from the step of the discriminant classification to diagnose AD or MCI.

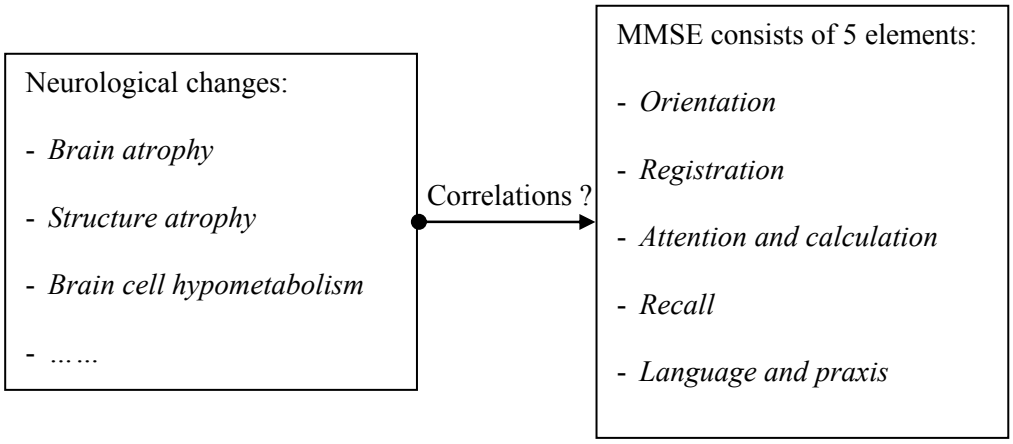

Figure 53. Correlations between cognitive scores and neurological changes

7.2 Experiment Subjects

The proposed methods are evaluated with a total of 400 experiment subjects introduced in Chapter 3. Each case consists of four parts of information: 1) personal information, 2) cognitive scores, 3) assessment or diagnosis result, and 4) FDG-PET volumetric images.

Personal Information

The personal information contains the patient identity (ID), date of birth, date of study, gender, etc. Only the information of gender and age is included in our study. There are 274 males and 126 females; their average age at study day is 76.9 years old, and the standard deviation of the ages is 6.5 years old, i.e. 76.9 ± 6.5.

Cognitive Scores

Most of the subjects were evaluated with several cognitive score systems including MMSE, CDR, functional assessment questionnaire (FAQ), and neuropsychiatric inventory (NPI). The MMSE scores (26.3 ± 3.5) and CDR scores (0.5 ± 0.4) are included into our study because of their widespread use in clinical diagnosis of AD and MCI.

Assessment or Diagnosis Results

All of the subjects had been clinically assessed as cognitively normal (122 subjects or 30.5%) or diagnosed with AD (66 subjects or 16.5%) or MCI (212 subjects or 53%). The evaluation of the proposed methods is based on these assessment and diagnosis results as gold standard.

FDG-PET Images

The FDG-PET images have a grid of 160×160×96 voxels with the voxel size 1.5×1.5×1.5 mm^3. The preprocessed images have their horizontal axis paralleled with the anterior commissure and posterior commissure (refer to Chapter 3 for more details of the FDG-PET images).

7.3 Automatic AD Assessment Methods

Figure 54 shows the flowchart of the proposed approach. It is an atlas-assisted region-of-interest (ROI) approach to automatically extract the AD-specific structures from brain images for statistical analysis by making use of the FDG-PET images and the AD-specific brain atlas. It consists of the following components: grouping of template cases

and validation cases, atlas-based image data processing, and statistical analysis including correlation validation, cognitive score regression, and diagnosis classification.

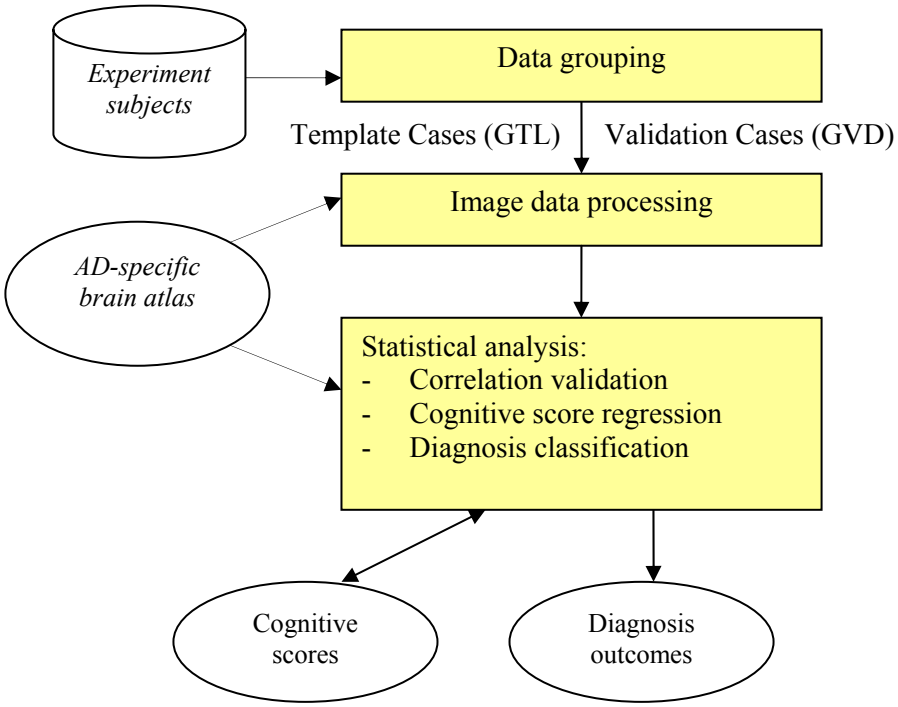

Figure 54. Flowchart of cognitive assessment and AD/MCI diagnosis

7.3.1 Data Grouping

All cases are randomly divided into two groups: template (GTL) and validation (GVD), as listed in Table 10. The GTL cases are used to generate the regression equations for MMSE and CDR by the statistical model of stepwise regression based on the glucose metabolism values extracted from the AD-specific structures of FDG-PET images. In addition, the GTL cases are also applied to generate the discriminant functions by the statistical model of discriminant classification based on the score values of MMSE or CDR. The functions are calculated on each case for the classification of the groups:

AD, MCI, or Normal (NL). The GVD cases are for testing purpose only to verify the regression equations and discriminant functions.

Table 10. Groups of template and validation cases

	Total*	AD**	MCI**	NL**
GTL	250	38 (15.2%)	133 (53.2%)	79 (31.6%)
GVD	150	28 (18.7%)	79 (52.7%)	43 (28.7%)
Total	400	66 (30.5 %)	212 (53%)	122 (16.5%)

** The number of cases in the data groups GTL and GVD*

*** The number of cases in the diagnostic groups with percentages*

7.3.2 Image Data Processing

This component is to extract the glucose metabolism information from the brain images for statistical analysis. It has two steps: spatial normalization and intensity normalization. Based on the algorithms introduced in Chapter 5 and Chapter 6, the spatial normalization is done by three sub-steps: 1) the brain areas are segmented from the PET images by a threshold which is selected by a histogram graph automatically (refer to Chapter 5); 2) the set of landmarks is accurately defined in the atlas space and automatically detected on PET images (refer to Chapter 6); and 3) the brain is divided into 18 cubic regions based on the landmarks, and a piecewise linear transformation is applied to generate a new volumetric image data fitting into the atlas space (refer to Chapter 4). Figure 55 shows an example of the results of spatial normalization. Figure 55a is an original axial slice for example; Figure 55b shows the landmarks identified and marked on the axial slice of Figure 55a; Figure 55c is the result of transformation of images into the atlas space; and Figure 55d is a merged view of the PET image and warped atlas image.

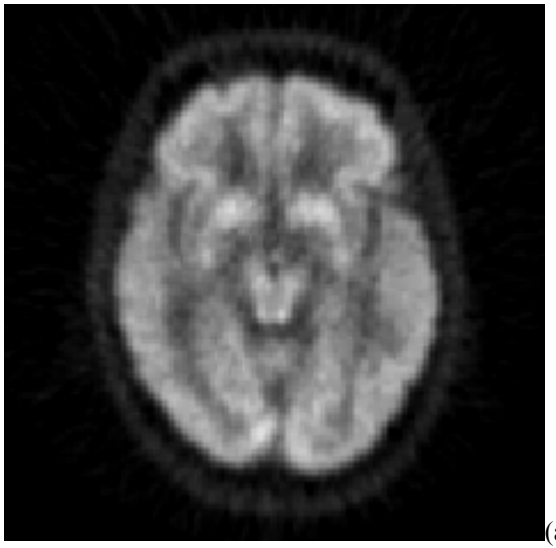

(a)

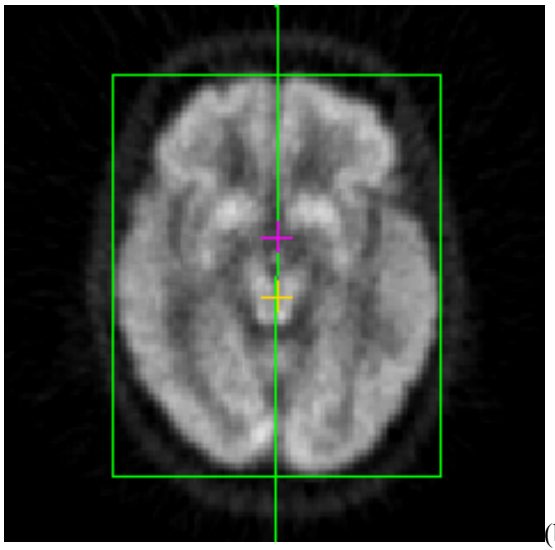

(b)

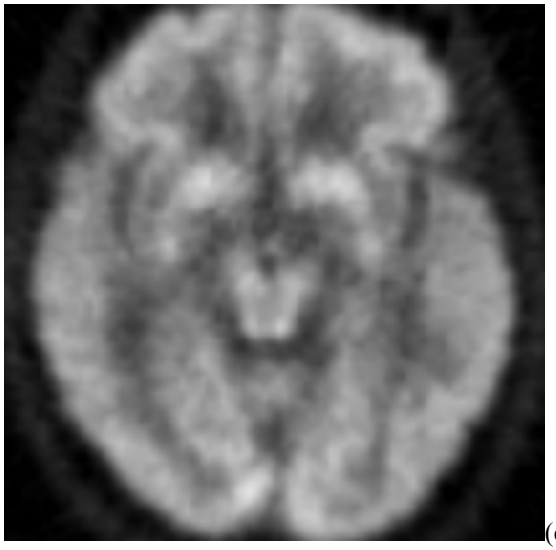

(c)

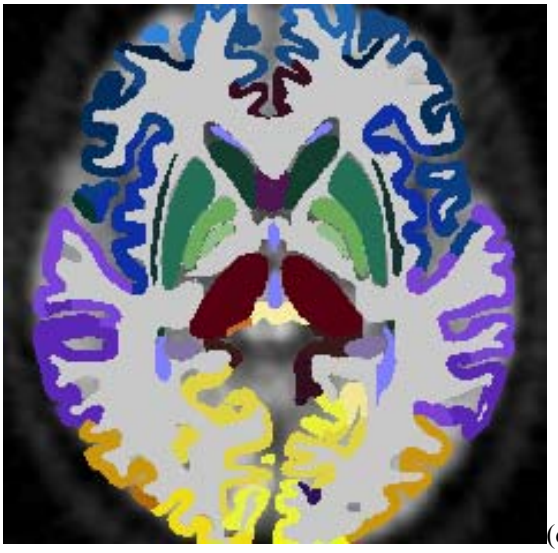 (d)

Figure 55. An example of spatial normalization steps
(a) original axial slice; (b) slice with landmarks identified and marked; (c) slice transformed to the atlas space; (d) transformed slice with atlas warped

For the intensity normalization, since the cerebellum is well preserved in AD, it is selected as the reference region to normalize the other areas including the hippocampus, amygdala, and their adjacent structures. To reduce the partial volume effect of the connected areas of different brain structures, the pixels with the highest and lowest 25% intensity values are excluded to calculate the average intensity.

A total of 400 cases with a resolution of 160×160×96 voxels of size 1.5 mm^3 were processed. The average processing time was 12.4 seconds per case. Table 11 lists the results of image data processing, including the normalized glucose metabolism values for all 14 AD-specific structures (the cerebellum is excluded due to its role of reference for normalization). The mean values with the standard deviations (SD) are shown for different groups AD, MCI, and NL, respectively. Based on *t-test* of independent samples, there are significant differences in several variables, e.g. the amygdala (AM), between the groups of AD/MCI, MCI/NL, and AD/NL, shown in Table 11. Also, several variables

like the globus pallidus medial (GPM) do not have significant differences between the groups of AD/MCI, even though the significant differences are shown between the groups of MCI/NL and AD/NL.

Table 11. Normalized average glucose metabolism of AD-specific structures

AD-specific structures	Normalized average values (mean ± SD)			Significances (*p*)		
	AD	MCI	NL	AD/MCI	MCI/NL	AD/NL
AM	0.68 ± 0.10	0.76 ± 0.10	0.87 ± 0.11	< 0.001	< 0.001	< 0.001
AG	0.81 ± 0.19	0.96 ± 0.17	1.05 ± 0.19	< 0.001	< 0.001	< 0.001
FG	0.80 ± 0.09	0.82 ± 0.11	0.88 ± 0.11	0.333	< 0.001	< 0.001
GPL	0.77 ± 0.09	0.77 ± 0.10	0.83 ± 0.19	0.061	< 0.001	< 0.001
GPM	0.80 ± 0.10	0.83 ± 0.13	0.90 ± 0.20	0.896	< 0.001	0.009
HC	0.71 ± 0.14	0.81 ±0.12	0.90 ± 0.14	< 0.001	< 0.001	< 0.001
ITG	0.58 ± 0.19	0.60 ±0.19	0.71 ± 0.21	0.655	< 0.001	< 0.001
IL	0.91 ± 0.08	0.94 ± 0.09	1.07 ± 0.13	0.002	< 0.001	< 0.001
MTG	0.80 ± 0.15	0.88 ± 0.11	0.98 ± 0.12	< 0.001	< 0.001	< 0.001
PG	0.56 ± 0.09	0.60 ± 0.10	0.72 ± 0.11	0.002	< 0.001	< 0.001
PU	1.11 ± 0.15	1.14 ± 0.15	1.23 ± 0.21	0.075	< 0.001	< 0.001
STG	0.85 ± 0.09	0.89 ± 0.09	0.96 ± 0.10	0.001	< 0.001	< 0.001
SG	0.84 ± 0.16	0.94 ± 0.15	0.99 ± 0.17	< 0.001	0.007	< 0.001
TH	0.82 ± 0.21	0.91 ± 0.19	0.99 ± 0.19	0.001	0.001	< 0.001

7.3.3 Statistical Analysis

The statistical analysis is performed on the GTL cases. It is based on the personal information, cognitive scores, clinical diagnosis result, and the glucose metabolism data extracted from the AD-specific structures (refer to Chapter 3 for the definition). It includes: 1) the correlation validation of cognitive scores with the AD-specific structures as well as the other variables like age and gender; 2) the stepwise regressions of cognitive scores based on the variables with top correlative values; and 3) discriminant classification of AD, MCI, and NL. The above statistical models are calculated by the

Statistical Package for Social Sciences (SPSS), version 16.0. The regression equations and classification functions are validated with the GVD cases by substituting the normalized average values of AD-specific structures into them to calculate the regressed cognitive scores and classified results.

Data Table

A data table is created to include all relevant information together for easier calculation by SPSS. The variables in the table consist of four types: 1) personal information including case ID, gender, and age; 2) cognitive scores including MMSE and CDR; 3) diagnosis results; and 4) the normalized average glucose metabolism of all AD-specific structures. An example of AD case is shown at the right-most column of Table 12. It is also used as an example for illustration of cognitive assessment and diagnosis classification in the subsequent sections. This 69.7 years old man was diagnosed as AD patient (diagnosis value is 1) at the day of study. His MMSE score was only 15 (< 17, refer to Appendix A) and his CDR score was as high as 2 (> 1, refer to Appendix B) at that day. The glucose consumption values of several structures such as the PG, AM, and HC have obvious reduction comparing to those of other structures like the PU (see Table 12 for abbreviations).

Table 12. Data table with descriptions and example

Variable Types	Variables Names	Short Names	Descriptions	Example
Personal Information	CaseID		Unique ID for each subject	104005
	Gender		Male (1) or Female (2)	1
	Age		Age at the day of study	69.7
Cognitive Scores	MMSE		Score at the day of study	15
	CDR		Score at the day of study	2
Diagnosis	Diagnosis		AD (1), MCI (2), or NL (3)	1
Average Glucose Metabolism	Amygdala	AM	Normalized average intensity values to the cerebellum	0.58
	Angular gyrus	AG		0.65
	Fusiform gyrus	FG		0.71
	Globus pallidus lateral	GPL		0.86
	Globus pallidus medial	GPM		0.84
	Hippocampus	HC		0.58
	Inferior temporal gyrus	ITG		0.64
	Insular lobe	IL		0.87
	Middle temporal gyrus	MTG		0.78
	Parahippocampal gyrus	PG		0.50
	Putamen	PU		1.19
	Superior temporal gyrus	STG		0.79
	Supramarginal gyrus	SG		0.71
	Thalamus	TH		0.63

Correlation Validation

The correlation test of all variables in Table 12 is based on bivariate correlation by calculating the Pearson's product-moment correlation coefficient. It is widely used in testing the linear dependence between two variables by giving a value between -1 and +1, and typically denoted by *R*.

$$R = \frac{\sum_{i=1}^{n}\left(x_i - \bar{x}\right)\left(y_i - \bar{y}\right)}{\sqrt{\sum_{i=1}^{n}\left(x_i - \bar{x}\right)^2}\sqrt{\sum_{i=1}^{n}\left(y_i - \bar{y}\right)^2}} \tag{7.1}$$

where x_i and y_i are the sample values of two testing variables, $\bar{x}$ and $\bar{y}$ are the mean values of the variables.

It is defined as the covariance of the two variables divided by the product of their standard deviations. The variables with higher R values, and also significant to the MMSE and CDR ($p < 0.01$), are selected as the independent variables for the stepwise regressions for MMSE and CDR.

Table 13. Correlation test between cognitive scores and independent variables

Variables	MMSE		Variables	CDR	
	R	*p*		*R*	*p*
AM	0.608	< 0.001	AM	-0.591	< 0.001
MTG	0.596	< 0.001	MTG	-0.566	< 0.001
HC	0.578	< 0.001	IL	-0.555	< 0.001
AG	0.547	< 0.001	HC	-0.497	< 0.001
STG	0.543	< 0.001	PG	-0.496	< 0.001
IL	0.491	< 0.001	STG	-0.490	< 0.001
SG	0.472	< 0.001	AG	-0.457	< 0.001
PG	0.445	< 0.001	SG	-0.406	< 0.001
TH	0.437	< 0.001	TH	-0.356	< 0.001
PU	0.328	< 0.001	FG	-0.329	< 0.001
GPM	0.243	< 0.001	PU	-0.328	< 0.001
FG	0.238	< 0.001	ITG	-0.308	< 0.001
ITG	0.238	< 0.001	GPM	-0.235	< 0.001
GPL	0.110	0.083	GPL	-0.212	0.001
Gender	-0.087	0.170	Age	0.110	0.083
Age	-0.124	0.05	Gender	0.031	0.629

In order to validate the correlations between the change of brain structures and the cognitive scores, Table 13 lists the Pearson correlation (R) and significant (p) values for both MMSE and CDR by descending sort of R. It shows that the variables gender and age are not significantly correlated with the cognitive scores; and the other variables of brain structures are more or less correlated with the scores. For a more detailed analysis, the top eight common variables of both MMSE and CDR in Table 13 are chosen as the most correlated brain structures with cognitive scores MMSE and CDR. They are the AM, MTG, HC, AG, STG, IL, SG, and PG.

Regressions of Cognitive Scores

In statistics, linear regression refers to an approach to modeling the relationship between one dependent variable y and one or more independent variables X $(x_1, x_2, \ldots x_n)$, by linearly estimating the unknown parameters from the sample data. This approximate relationship is modeled through a y-intercept constant C that adds adjustment to the linear relationship between the dependent variable y and independent variables X.

$$y = p_1x_1 + p_2x_2 + \ldots + p_nx_n + C \tag{7.2}$$

where $(p_1, p_2, \ldots p_n)$ are the unknown parameters to be estimated from the a set of sample data.

Linear regression is used extensively in many practical applications such as prediction. It can be used to fit a predictive model to an observed data set of y and X values. After developing such a model, if an additional value of X is then given without its accompanying value of y, the fitted model can be used to make a prediction of the value of y.

In our research, it is a prediction model to predict the MMSE or CDR scores by using the glucose metabolism values extracted from the PET images. The purpose of stepwise regressions of MMSE and CDR is to generate the regression equations, which would be used to estimate the cognitive scores for any existing or new case(s). The regression operation in SPSS needs to define one dependent variable and several independent variables. The dependent variable for MMSE regression is the MMSE score, and the dependent variable for CDR regression is the CDR score. The independent variables (also called "predict variables") are those most correlated structures selected from the AD-specific structures by the previous step "Correlation Validation".

The stepwise regression repeatedly chooses the predict variables (one or more of correlated structures) automatically to generate the regression equations by taking a sequence of analysis of variance (ANOVA) test for the equation and *t*-test for the independent variables. The outcome of the stepwise regression is a list of coefficients corresponding to the predict variables, and a constant as well. Those coefficients and the constant construct a linear equation for MMSE, if the dependent variable is the MMSE score. The CDR regression equation can be generated in the same way.

Table 14. Stepwise regressions of MMSE and CDR

	Steps	R^2	Adjusted R^2	F	Significant (*p*)
MMSE	1	0.370	0.368	145.775	< 0.001
	2	0.474	0.469	111.110	< 0.001
	3	0.526	0.520	90.924	< 0.001
	4	0.543	0.535	72.699	< 0.001
	5	0.554	0.545	60.712	< 0.001
CDR	1	0.349	0.347	133.208	< 0.001
	2	0.438	0.433	96.070	< 0.001
	3	0.456	0.449	68.647	< 0.001
	4	0.474	0.465	55.170	< 0.001

The stepwise regressions for MMSE and CDR are shown in Table 14. Their progresses are stopped after five and four steps of regressions for MMSR and CDR, respectively. This means the stepwise regressions have five/four steps to enter one predicting variable by each step. In Table 14, R^2 is simply the square of the sample correlation coefficient between the outcomes and their predicted values. Adjusted R^2 is a modification of R^2 that adjusts for the number of explanatory terms in a model. Unlike R^2, the adjusted R^2 increases only if the new term improves the model more than would be expected by chance. The adjusted R^2 can be negative, and will always be less than or equal to R^2.

Table 15. Stepwise regression equation coefficients for MMSE and CDR

	Predictive Variables	Coefficients*	t-values	Significances (*p*)
MMSE	AM	11.57	6.097	< 0.001
	MTG	13.53	7.742	< 0.001
	AG	7.67	6.485	< 0.001
	STG	-8.14	-2.745	0.007
	IL	-5.33	-2.525	0.012
	(Constant)**	10.22	6.788	< 0.001
CDR	AM	-1.34	-5.973	< 0.001
	MTG	-1.46	-6.573	< 0.001
	AG	-0.61	-3.961	< 0.001
	STG	1.14	2.912	0.004
	(Constant)**	2.39	12.681	< 0.001

** The coefficients of each predictive variable in linear equations*

*** The constant values in linear equations*

Table 15 lists the coefficients for each predict variable as well as the constants of regression equations. For example, the MMSE regressions have five predict variables: *AM*, *MTG*, *AG*, *STG*, and *IL*. The linear regression equation for calculation of cognitive MMSE scores (R_m) is constructed from these coefficients and the constant.

$$R_m = 11.57 \times AM + 13.53 \times MTG + 7.67 \times AG - 8.14 \times STG - 5.33 \times IL + 10.22 \quad (7.3)$$

For CDR, the linear regression equation for calculation of CDR scores (R_c) is similarly constructed from four coefficients of predict variables *AM*, *MT*, *AG*, and *ST*.

$$R_c = -1.34 \times AM - 1.46 \times MTG - 0.61 \times AG + 1.14 \times STG + 2.39 \quad (7.4)$$

For the example in Table 12, *AM*=0.58, *MTG*=0.78, *AG*=0.65, *STG*=0.79, and *IL*=0.87, the calculation results of regressed MMSE (R_m) and regressed CDR (R_c) are 21.41 and 0.97 by equation (7.3) and (7.4), respectively.

Classification of AD, MCI and NL

Classification is a machine learning procedure in which individual items are placed into groups based on quantitative information on one or more characteristics of the items. The goal of classification is to build a set of models that can correctly predict the class of the different objects. The classification methods such as discriminant analysis and artificial neural network have the advantages over the clustering methods such as k-mean and fuzzy c-mean. The key advantage is that they have an explicit knowledge of the classes the different objects belong to. Those algorithms can perform an effective feature selection and lead to better prediction accuracy.

Classifier performance depends on the characteristics of the data to be classified. There is no single classifier that works best on all given problems. The commonly used classification algorithms include logistic regression, artificial neural networks, discriminant analysis, etc. Logistic regression is used for prediction of the probability of occurrence of an event by fitting data to a logistic curve. It is a generalized linear model used for binomial regression. Artificial neural networks are parallel computing devices consisting of many interconnected simple processors. Each processor in the network is simple and only for a single task. However, the whole network becomes quite

complicated for computation and difficult to setup to produce good results [Harper, 2005]. Discriminant analysis builds a predictive model for group membership. The model is composed of discriminant functions based on linear combinations of the predictor variables that provide the best discrimination between the groups. The functions are generated from a sample of cases for which the group membership is known. The functions can then be applied to new cases that have measurements for the predictor variables but have an unknown group membership. The Fisher's linear discriminant analysis model is matched well to our requirements to predict the group membership of experiment subjects.

To classify the experiment cases into the groups of AD, MCI, and NL, the Fisher's linear discriminant analysis is applied to generate the discriminant functions by calculating the Fisher's coefficients of all predict variables. For discriminant classification in SPSS, the grouping variable is the diagnosis results, i.e. AD, MCI, and NL. In order to determine whether the most-affected structures by AD are supposed to be included as the predict variables for Fisher's linear discriminant analysis, two situations are considered: 1) only use the cognitive scores as a single input (Method A); and 2) use both the cognitive scores and the normalized average intensity values of the correlated structures as the input (Method B). The outcome of discriminant classification analysis contains several discriminant function coefficients that can be used directly for classification. As the grouping variable has three values (AD, MCI, and NL), three sets of coefficients of predict variables are obtained for each group. The testing case is assigned to the group for which it has the largest discriminant score.

There is only one predict variable for Method A. It is regressed MMSE (R_m) or regressed CDR (R_c) for MMSE scores or CDR scores as shown in Table 16. For Method

B, there are two additional predict variables *IL* and *PG* for MMSE scores and three additional predict variables *AG*, *IL*, and *PG* for CDR scores. Each variable has its coefficient to construct discriminant functions with a constant for each function. The coefficients of the predict variables and the constants are listed in Table 16. For each method, there are three functions to discriminate one group from others. For example, the functions of MMSE for Method A are described by equation (7.5), and the functions for Method B are described by equation (7.6).

$$\begin{aligned} MA_{AD} &= 6.528 \times Rm - 76.945 \\ MA_{MCI} &= 7.256 \times Rm - 94.790 \\ MA_{NL} &= 8.01 \times Rm - 115.272 \end{aligned} \tag{7.5}$$

$$\begin{aligned} MB_{AD} &= 5.251 \times Rm + 51.914 \times IL + 8.356 \times PG - 87.634 \\ MB_{MCI} &= 6.004 \times Rm + 49.968 \times IL + 9.544 \times PG - 105.019 \\ MB_{NL} &= 6.483 \times Rm + 57.139 \times IL + 17.599 \times PG - 130.517 \end{aligned} \tag{7.6}$$

The functions of CDR for Method A are described by equation (7.7), and the functions for Method B are described by equation (7.8).

$$\begin{aligned} CA_{AD} &= 18.549 \times Rc - 8.484 \\ CA_{MCI} &= 12{,}431 \times Rc - 4.415 \\ CA_{NL} &= 4.648 \times Rc - 1.562 \end{aligned} \tag{7.7}$$

$$\begin{aligned} CB_{AD} &= 126.267 \times Rc + 112.512 \times AG + 125.354 \times IL + 165.203 \times PG - 198.006 \\ CB_{MCI} &= 121.667 \times Rc + 119.104 \times AG + 117.531 \times IL + 171.385 \times PG - 197.103 \\ CB_{NL} &= 117.299 \times Rc + 120.618 \times AG + 122.058 \times IL + 179.793 \times PG - 207.104 \end{aligned} \tag{7.8}$$

For the case in Table 12 *IL* is 0.87, *PG* is 0.50, and *Rm* is 21.41, equation (7.6) gives the results of Method B: MB_{AD}=74.19, MB_{MCI}=71.77, and MB_{NL}=61.65. As the maximum value of three variables is MB_{AD}, the subject is classified as a patient with AD.

Table 16. Discriminant function coefficients for classification

Scores	Methods	Variables	AD*	MCI*	NL*
MMSE	A	*Rm*	6.528	7.256	8.010
		(Constant)**	-76.945	-94.790	-115.272
	B	*Rm*	5.251	6.004	6.483
		IL	51.914	49.968	57.139
		PG	8.356	9.544	17.599
		(Constant)**	-87.634	-105.019	-130.517
CDR	A	*Rc*	18.549	12.431	4.648
		(Constant)**	-8.484	-4.415	-1.562
	B	*Rc*	126.267	121.667	117.299
		AG	112.512	119.104	120.618
		IL	125.354	117.531	122.058
		PG	165.203	171.385	179.793
		(Constant)**	-198.006	-197.103	-207.104

** The coefficients of each predictive variable in linear equations*

*** The constant values in linear equations*

Success Rate

Before verification of the results, a variable named success rate is defined to quantitatively measure the degree of the successful diagnosis. The success rate is defined as a ratio of the number of successful classified cases automatically by the number of cases clinically diagnosed in that category.

$$\text{SuccessRate}(m,c,s) = \frac{\text{A}(m,\ c,\ s)}{\text{N}(c)} \tag{7.9}$$

where m is the method used (Method A or Method B), c is the subject category (AD, MCI, or NL), s is the score system (MMSE or CDR), A(m,c,s) is the number of cases which are classified as the category c by the method m with score system s. N(c) is the number of cases which are clinically classified as the category c. For example, if there are 38 AD

cases in the group GTL, and the number of cases which were classified as AD by Method A is 29, the success rate of Method A for AD diagnosis is 29/38, i.e. 76.3%.

Result Verification

The regression equations and discriminant functions obtained by the statistical models need to be verified by all the GTL cases as well as the GVD cases. It is done by substituting the normalized average values of AD-specific structures into the regression equations to calculate the regressed cognitive scores, and into the discriminant functions to classify the testing cases into different diagnosis groups of AD, MCI, and NL.

For each testing case, the normalized average intensity values of AD-specific structures are the input for both stepwise regression and discriminant classification. They are applied to calculate the regressed values of MMSE and CDR first for cognitive assessment. Thereafter, the discriminant values are computed based on the regressed values of MMSE and CDR. To measure the accuracy of the classification methods, a success rate is defined to quantify for each statistical method, each group of cases, and each category of subjects.

The final classification results are given in Table 17 and Table 18, including 250 GTL cases and 150 GVD cases. For GTL cases, the average success rates of Method A are 62.8% and 62.4% by the regressed-MMSE and regressed-CDR, respectively; the average success rates of Method B are 65.6% and 69.2% correspondingly. For GVD cases, the success rates of Method A are 52% and 56.7%, and those of Method B are 61.3% and 60.7% by the regressed-MMSE and regressed-CDR.

There are several observations on the classification results of Table 17 and Table 18. More discussions are given in the next section.

- The success rates of Method B are higher than those of Method A for both MMSE and CDR scores and for both groups of GTL and GVD as well. However, the sensitivity (SN), specificity (SP), and Dice's index (DI) in Table 18 shows no major difference between two methods.
- The success rates of MCI patients are much lower than those of AD patients and NL subjects in each method and each group of cases. The sensitivities of MCI patients are also much lower than those of AD patients and NL subjects for GTL cases.
- The success rates as well as the sensitivities of GVD cases are lower than those of GTL cases.
- The success rates of different score systems show no major difference. In other words, both MMSE and CDR are appropriate to present the cognition impairment

Table 17. Classification results with success rate

Groups	Scores	Methods	AD (%)*	MCI (%)*	NL (%)*	Total (%)*
GTL	Number of Cases**		38	133	79	250
	MMSE	A	29 (76.3)	64 (48.1)	64 (81.0)	157 (62.8)
		B	28 (73.7)	73 (54.9)	63 (79.7)	164 (65.6)
	CDR	A	28 (73.7)	64 (48.1)	64 (81.0)	156 (62.4)
		B	32 (84.2)	77 (57.9)	64 (81.0)	173 (69.2)
GVD	Number of Cases**		28	79	43	150
	MMSE	A	19 (67.9)	35 (44.3)	24 (55.8)	78 (52.0)
		B	19 (67.9)	47 (59.5)	26 (60.5)	92 (61.3)
	CDR	A	20 (71.4)	42 (53.2)	23 (53.5)	85 (56.7)
		B	19 (67.9)	47 (59.5)	25 (58.1)	91 (60.7)

** The number of successful diagnostic cases with success rates by proposed approach*

*** The number of diagnostic cases clinically (as gold standard)*

Table 18. Classification results with sensitivity, specificity and Dice's index

Score		MMSE						CDR					
Category		AD		MCI		NL		AD		MCI		NL	
Method		A*	B*	A*	B*	A*	B*	A*	B*	A*	B*	A*	B*
GTL	SN	76.3	73.7	48.1	54.9	81.0	79.7	73.7	84.2	48.1	57.9	81.0	81.0
	SP	81.6	81.6	80.3	78.6	81.9	87.1	81.6	84.0	78.6	82.9	82.5	86.5
	DI	54.7	53.3	58.2	63.2	73.6	76.8	53.3	61.5	57.7	67.0	74.0	77.1
GVD	SN	67.9	67.9	44.3	59.5	55.8	60.5	71.4	67.9	53.2	59.5	53.5	58.1
	SP	83.8	82.0	67.6	71.8	72.9	85.0	84.4	81.1	64.8	70.4	80.4	86.0
	DI	56.7	55.1	51.1	64.4	50.0	61.2	59.7	54.3	57.5	63.9	52.9	60.2

** Percentages of sensitivities, specificities, and Dice's indices*

7.4 Discussion

Numerous algorithms of medical image segmentation were implemented and presented for both structural medical images like MRI or CT, and functional medical images like PET. However, the segmentation of ROIs from PET neuroimages faces more difficulties due to the absence of boundary information in these images. Accurate segmentation of a particular structure from PET images automatically is almost not possible. Therefore, atlas-based methods have their advantages to identify several landmarks instead of the identification of the boundaries. The accuracy of atlas-based methods highly depends on that of landmark identification. The inaccurate landmark identification causes the inaccurate information extracted from the ROI, i.e. the measurement of average glucose metabolism in our research work. It is a very time-consuming task to ensure the accuracy of the landmark identification by visual inspection case by case by neurological or radiological experts.

After the fast and automatic data transformation of PET images into the atlas space, the information extracted from the ROIs of hundreds of cases is performed by several

statistical models such as correlation validation, stepwise regression, and discriminant classification. There are several observations on the statistical results.

Method B is superior to Method A

In average, the success rates of Method B are higher than those of Method A. That means the correlated structures are also the important factors for the discriminant classification even through the regressed cognitive scores are already based on these structures. However, there are no major differences between the methods in the sensitivities, specificities, and Dice's indices. Therefore, Method B is only superior in filtering the particular group (e.g. AD) from the other groups.

Success rates of MCI

Although the experiment data have three category groups: AD, MCI, and NL, most of the AD cases are at mild stage. There is only a few cases (< 1%) are at moderate stage, and no severe AD cases at all. If the changes of glucose metabolism on the AD-specific structures are too subtle to be distinguished by the classification algorithm, it is a high possibility to classify the MCI cases into AD or NL. In addition, the calculation of success rates is based on the clinical diagnosis results, which may not only depend on the cognitive scores, but also the experience of doctors. There may have some deviation between the doctor's judgment and the cognitive score. The conflicts between the cognitive scores and the diagnosis results are found in several cases. For example, a patient with 27 MMSE score was diagnosed as AD, and another case with 25 MMSE score was classified as normal subject. For the category of MCI, the highest MMSE score of MCI patients is 30 and the lowest is only 19, but both of them were diagnosed as MCI.

In addition, the MMSE itself is not sensitive in detecting mild dementia [Crum et al., 1993].

Success rates of GVD cases

The statistical models are performed on the GTL cases, which have higher success rates than those of GVD cases. The regression equations and discriminant functions are based on an assumption that the cognitive scores such as MMSE and CDR have linear correlation with the changes of glucose metabolism on AD-specific structures. If the assumption is not always true, or the cognitive scores have correlated with the structures other than those we defined as AD-specific, the regression equations or discriminant functions may depend highly on the template data. When they are applied to the other data which are not the part of template cases, the success rates are dropped.

AD-affected structures are excluded from the statistical analysis

The hippocampus and parahippocampal gyrus are considered the firstly affected structures in the brain by AD. However, they are too small to be accurately segmented by the automatic computer algorithms. In addition, the partial volume effect may be more serious in those small structures than the larger structures due to the high ratio of boundaries of the structure by the whole structure areas.

7.5 Summary

In summary, the results of statistical analysis depend on several factors like the number of samples, statistical models, data distributions, etc. There are a few possible ways to increase the success rates of stepwise regressions by:

- adding more brain structures as the independent variables;
- removing the noise data, for example, the cases with low MMSE but was diagnosed as MCI or NL and vice versa;
- separating the left and right hemispheres for each brain structure; and
- exploring other statistical models such as neural network and non-parameter tests.

This chapter presents an automated atlas-assisted approach, which makes use of the image data processing methods and a high resolution brain atlas presented in the previous chapters, together with the statistical models of stepwise regressions and discriminant classification to assess the cognitive scores and distinguish the patients with AD or MCI from normal subjects. The approach has been applied to hundreds of cases and shown promising results. For template cases, the average success rates are 65.6% and 69.2% by Method B with MMSE scores and CDR scores, respectively. For validation cases, the average success rates are 61.3% and 60.7% by Method B with MMSE scores and CDR scores. This is the first effort to quantitatively calculate the cognitive scores by processing the neuroimages automatically. There are still some rooms to improve the success rates of the diagnosis.

Chapter 8

Research Summary and Future Directions

This chapter summarizes the work in this thesis and discusses the future research directions.

8.1 Research Summary

This thesis investigates the problems of current clinical cognitive assessments and diagnosis for Alzheimer's disease (AD) as well as the mild cognitive impairment (MCI), and presents a rapid and fully automatic way to assist the assessment of cognitions and diagnosis of the disease. Currently the diagnosis is based on the evaluation of medical history and the assessment of cognitive scores like mini mental state examination (MMSE) and clinical dementia rating (CDR). The scores are influenced by several factors like language, education levels, etc. Therefore, the conventional way of AD and MCI diagnosis has the following problems: is subjective, time-consuming, and inaccurate. In addition, it is usually very costly because only experienced professionals are capable of it. The approach presented in this thesis provides an objective and efficient way for the

cognitive assessment and the diagnosis of the patients with AD or MCI, by processing the neuroimages based on the AD-specific brain atlas automatically and analyzing the outcomes of image processing with several statistical models. It is fully automatic and shows the promising success rates to distinguish the AD patients from the normal subjects in a rapid and useful way to reduce the expensive cost by the computer programs.

The accuracy of cognitive assessment and diagnosis highly depends on that of image processing results, including the brain segmentation and registration with the atlas space. To extract the accurate glucose metabolism information from the positron emission tomography (PET) images, a high resolution three-dimensional brain atlas was constructed to meet the requirements. It has the anatomical structures of the human brain accurately segmented and labeled by an interactive platform with several advanced tools such as interactive semi-automatic segmentation tool, powerful contour editor, and user friendly visualization tool for two-dimensional images and three-dimensional objects. The atlas labels the AD-specific regions such as the amygdala, hippocampus, and temporal lobe. It also accurately positions the cortical landmarks as well as the internal landmarks such as the anterior commissure and posterior commissure. The landmarks play a key role in PET image registration with the atlas space, and the accuracy of the landmark identification on the PET images affects that of the image registration.

The automated method of the landmark identification on the PET images has several steps. After the brain is extracted from the volumetric images by the algorithms of thresholding and region growing, the left and right brain hemispheres are separated by a midsagittal plane which is calculated from a group of midsagittal lines on axial slices. Nine landmarks are defined and identified on PET images automatically: anterior commissure and posterior commissure (AC and PC), left and right extents of the cortex

(L and R), anterior and posterior extents of the cortex (A and P), interior and superior extents of the cortex (I and S), and cerebellum inferior (CBI).

After the registration of the PET images with the atlas space, the intensity values of every region can be obtained and calculated to be the input of the statistical models for further analysis. The values of each region are normalized to avoid the variation of image scanning with different scanners and different parameters. The glucose metabolism information of different regions or structures together with the personal information of subjects such as age and gender is combined together for statistical analysis. The data extracted from the AD-specific structures are the independent variables to be calculated in different statistical models such as correlation validation, stepwise regressions, and discriminant classification. The correlation validation is to test the correlation between these independent variables and the cognitive scores in order to exclude the variables which are not or less correlated. The top correlated variables are then applied to the stepwise regressions to construct the regression equations for calculation of the cognitive scores. Any individual subjects with FDG-PET scanning are initially and automatically evaluated for the cognitive impairment. Based on the cognitive scores as well as the top correlated variables (AD-specific structures), the subject is diagnosed as AD, MCI, or Normal.

The algorithms presented in this thesis include the brain extraction from neuroimages, landmark identification on PET images, and spatial and intensity normalization of PET images. They are all fully automatic and have high accuracies by validation with the ground truth manually generated by the neuroanatomy expert. The algorithms gave the promising results by testing hundreds of cases. There are several novel research contributions in this thesis. They are 1) a platform with several powerful and intelligent

tools for a new digital brain atlas construction and other neuroimage processing, the atlas has accurate brain structures segmented and labeled including the AD-specific structures, 3) algorithms for automated brain extraction from structural and functional neuroimages, 4) a set of landmarks is extended to include the cerebellum into the atlas space, 5) automatic landmark detection on PET volumetric data, and 6) an assessment method to evaluate and diagnose the experiment subjects.

In summary, a rapid and automated valuation method is presented in this thesis for cognitive assessment and diagnosis of AD and MCI, and it shows the promising results for both image processing and statistical analysis by comparing with the traditional approach. Chapter 4 presents a new brain atlas constructed by a set of interactive and intelligent construction tools. The atlas contains accurate information of AD-specific structures. Chapter 5 discusses the design and implementation of the automated brain extraction methods from neuroimages including structural CT images and functional PET images. The brain areas are segmented from the neuroimages automatically for further processing in the subsequent steps. Chapter 6 extends the Talairach landmarks to include a new landmark for more accurate transformation of PET images into the standard Talairach space. The AD-specific structures are segmented from the PET images and then analyzed statistically to generate the discriminant functions to assess the cognitive scores in Chapter 7.

8.2 Future Directions

There are two directions for future work: 1) to make the presented method more powerful, which means to increase the accuracy of image processing algorithms as well

as the results of statistical analysis; 2) to build an extendable platform to extend the research to other dementias and neurodegenerative diseases, or even other applications.

8.2.1 Accuracy Improvement

There are several ways to possibly enhance the presented approach: 1) to make use of the data and diagnosis results to add more cases to participate the statistical analysis; 2) to enhance the accuracy of the image processing algorithms; and 3) to consider more sophisticated statistical analysis models.

Post-processing of Diagnosis Results

The outcome of cognitive assessment and disease diagnosis could be post-processed manually as shown in Figure 56. If the computer-generated diagnosis results are same to those by the clinicians manually, the subjects with new assessment scores and diagnosis results can be included into the template cases to generate more accurate regression equations and discriminant functions. Otherwise, if the automatic results are different from those of manually generated by professionals, the further analysis may be required to find out the possible reasons, e.g. the image processing algorithms give an inaccurate result. If there is no reasonable ground for the failure, it is possible to explore more AD-related findings.

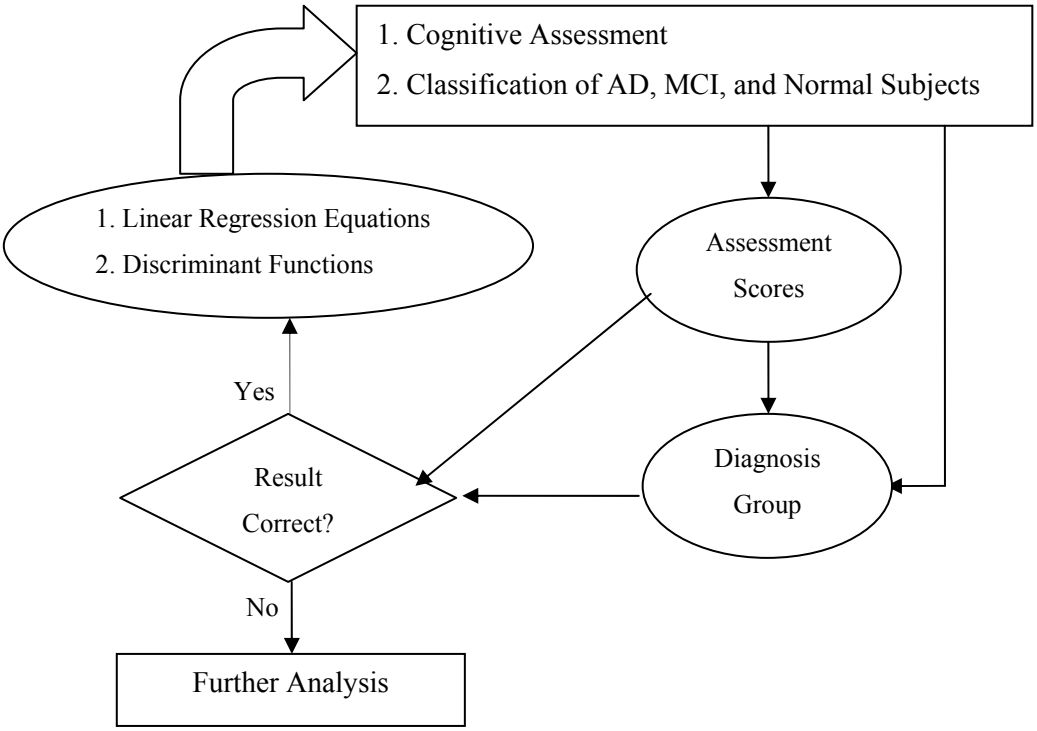

Figure 56. Post-processing of diagnosis results

Image Processing Algorithm Enhancement

The algorithms of image processing have some rooms for enhancement. For example, the partial volume effect of the images may cause inaccuracy of brain segmentation; linear transformation from scan images to atlas space may be inferior to the methods of non-linear transformation, etc. However, the computation cost must be considered too.

More Sample Data

Current collection of the data includes the normal subjects as well as the patients with AD and MCI. However, the AD patients are mostly the mild AD (MMSE > 20). There are very rare moderate or severe cases (MMSE < 20). Therefore, the range of scores is limited, and the success rates of MCI diagnosis are lower than that of AD and normal subjects. If the dataset contained more moderate and severe AD patients to generate the

regression equations and discriminant functions, the higher success rates of diagnosis could be expected.

New Imaging Techniques

The imaging techniques like PET/CT or PET/MRI dual-modality may increase the accuracy of brain extraction and structure segmentation as the structural neuroimages usually have higher contrasts and resolutions than the functional neuroimages. If the dual-modality imaging data, including the patients with AD, MCI, as well as normal subjects, are available in the future, the CT or MRI image processing algorithms may be applied for better segmentation results than that on PET images directly.

Other Intensity Normalization

The glucose consumptions in brain cells are detectable in FDG-PET images. Both the cerebrum and cerebellum are affected, even though the cerebellum is less-affected than some cerebral structures. However, the brainstem or pons may not be affected by the disease and be applied to normalize the intensity values of other structures.

More Brain Structures

More brain structures, which have not been minutely studied for AD, may have potential values to assess the cognitive scores and diagnose the disease. The atlas-based ROI extraction has finer parcellation for almost all brain structures, which may be used for further analysis of the correlation with the disease. The non-affected structures may become the references for intensity normalization, and new AD-related structures may be discovered and become the predict variables for statistical analysis.

More Cognitive Score Systems

More cognitive score systems other than MMSE and CDR may be applied to test the subjects, such as functional assessment questionnaire (FAQ) and neuropsychiatric inventory (NPI). These score systems could be compared to find out which one is more reliable or precise for AD computational assessment and diagnosis.

More Statistical Models

Currently only the linear stepwise regressions are used for the cognitive score regressions, and only a few predict variables participate the regression steps. More sophisticated statistical models such as least squares regression, non-linear regression, categorical regression, may be considered. In addition, other classification methods such as artificial neural network, clustering methods may be applied.

8.2.2 Extendable Platform

The proposed AD assessment and diagnosis approach is based on a set of atlas-based automatic image processing algorithms, a set of powerful tools, and a set of statistical analysis models. Figure 57 shows a diagram of the extendable platform architecture. It may be extended to the assessment or diagnosis of other dementia or even other neurodegenerative diseases, which may be built on top of these algorithms, statistical models, and powerful interactive tools, e.g., the other dementias like vascular dementia, the other neurodegenerative diseases like Parkinson's disease.

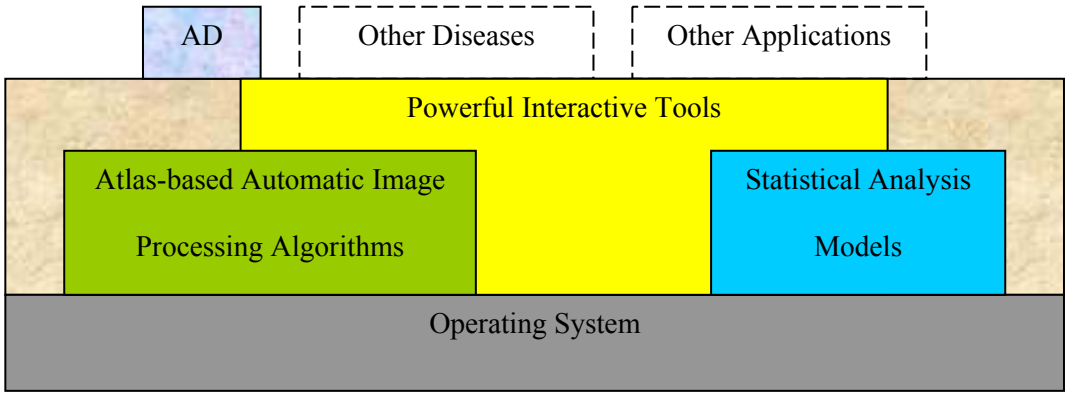

Figure 57. Extendable platform for neuroimage processing and statistical analysis

The presented approach may also be extended to the other potential applications such as the monitoring of disease progression, by calculating the longitudinal time series glucose metabolic rate of particular structures for same patient.

We believe that the extended platform would have a great opportunity for automatic and objective assessment of cognitive severity and diagnosis of neurodegenerative diseases in scientific research as well as clinical practice.

References

[Akselrod-Ballin 2006] Akselrod-Ballin, A., Galun, M., Gomori, M.J., Basri, R., and Brandt, A., *Atlas guided identification of brain structures by combining 3D segmentation and SVM classification.* Lecture Notes in Computer Science, 2006. 4191: pp. 209-216.

[Alexander 2002] Alexander, G.E., *Longitudinal PET evaluation of cerebral metabolic decline in dementia: A potential outcome measure in Alzheimer's disease treatment studies.* American Journal of Psychiatry, 2002. 159(5): pp. 738-745.

[Allen 2008] Allen, P., Laroi, F., McGuire, P., and Aleman, A., *The hallucinating brain: a review of structural and functional neuroimaging studies of hallucinations.* Neuroscience and Biobehavioral Reviews, 2008. 32(1): pp. 175-191.

[Amaro 2006] Amaro, E., *Study design in fMRI: basic principles.* Brain and cognition, 2006. 60(3): pp. 220-232.

[Amunts 2005] Amunts, K., Kedo, O., Kindler, M., Pieperhoff, P., Mohlberg, H., Shah, N., Habel, U., Schneider, F., and Zilles, K., *Cytoarchitectonic mapping of the human amygdala, hippocampal region and entorhinal cortex: intersubject variability and probability maps.* Anatomy and embryology, 2005. 210(5): pp. 343-352.

[Apostolova 2006] Apostolova, L., Lu, P., Rogers, S., Dutton, R., Hayashi, K., Toga, A., Cummings, J., and Thompson, P., *3D mapping of mini-mental state examination performance in clinical and preclinical Alzheimer disease.* Alzheimer Disease & Associated Disorders, 2006. 20(4): pp. 224-231.

[Ashburner 2003] Ashburner, J., Csernansky, J.G., Davatzikos, C., Fox, N.C., Frisoni, G.B., and Thompson, P.M., *Computer-assisted imaging to assess brain structure in healthy and diseased brains.* Lancet Neurol, 2003. 2(2): pp. 79-88.

[Baxter 2006] Baxter, L., Sparks, D., Johnson, S., Lenoski, B., Lopez, J., Connor, D., and Sabbagh, M., *Relationship of cognitive measures and gray and white matter in Alzheimer's disease.* Journal of Alzheimer's Disease, 2006. 9(3): pp. 253-260.

[Berchtold 1998] Berchtold, N. and Cotman, C., *Evolution in the conceptualization of dementia and Alzheimer's disease: Greco-Roman period to the 1960s.* Neurobiology of Aging, 1998. 19(3): pp. 173-189.

[Bhanuprakash 2006] Bhanuprakash, K.N., Hu, Q., Aziz, A., and Nowinski, W.L., *Rapid and automatic localization of the anterior and posterior commissure point landmarks in MR volumetric neuroimages.* Academic Radiology, 2006. 13(1): pp. 36-54.

[Boesen 2004] Boesen, K., Rehm, K., Schaper, K., Stoltzner, S., Woods, R., Luders, E., and Rottenberg, D., *Quantitative comparison of four brain extraction algorithms.* Neuroimage, 2004. 22(3): pp. 1255-1261.

[Borrie 2007] Borrie, M., *Functional neuroimaging in the diagnosis of dementia.* Alzheimer's & Dementia: The Journal of the Alzheimer's Association, 2007. 3(4): pp. 336-340.

[Braak 1991] Braak, H. and Braak, E., *Neuropathological staging of Alzheimer-related changes.* Acta Neuropathol, 1991. 82: pp. 239-259.

[Brankov 2003] Brankov, J.G. and Wernick, N., *Segmentation of dynamic PET or fMRI images based on a similarity metric.* Nuclear Science, IEEE Transactions on, 2003. 50(5): pp. 1410-1414.

[Brenner 2005] Brenner, W., Mester, J., and Clausen, M., *Adjusted scaling of FDG positron emission tomography images for statistical evaluation in patients with suspected Alzheimer's disease.* J Neuroimaging, 2005. 15: pp. 348-355.

[Brown 2000] Brown, M.S., Goldin, J.G., McNitt-Gray, M.F., Greaser, L.E., Sapra, A., Li, K.T., Sayre, J.W., Martin, K., and Aberle, D.R., *Knowledge-based segmentation of thoracic computed tomography images for assessment of split lung function.* Medical Physics, 2000. 27(3): pp. 592-598.

[Buckner 2004] Buckner, R.L., Head, D., Parker, J., Fotenos, A.F., Marcus, D., Morris, J.C., and Snyder, A.Z., *A unified approach for morphometric and functional data analysis in young, old, and demented adults using automated atlas-based head size normalization: reliability and validation against manual measurement of total intracranial volume.* Neuroimage, 2004. 23(2): pp. 724-738.

[Burdette 1996] Burdette, J.H., Minoshima, S., Vander Borght, T., Tran, D.D., and Kuhl, D.E., *Alzheimer disease: improved visual interpretation of PET images*

by using three-dimensional stereotaxic surface projections. Radiology, 1996. 198(3): pp. 837-843.

[Carmichael 2005] Carmichael, O.T., Aizenstein, H.A., Davis, S.W., Becker, J.T., Thompson, P.M., Meltzer, C.C., and Liu, Y., *Atlas-based hippocampus segmentation in Alzheimer's disease and mild cognitive impairment.* NeuroImage, 2005. 27(4): pp. 979-990.

[Chan 2001] Chan, D., Fox, N.C., Jenkins, R., Scahill, R.I., Crum, W.R., and Rossor, M.N., *Rates of global and regional cerebral atrophy in AD and frontotemporal dementia.* Neurology, 2001. 57(10): pp. 1756-1763.

[Chertkow 2007] Chertkow, H. and Black, S., *Imaging biomarkers and their role in dementia clinical trials.* The Canadian Journal of Neurological Sciences, 2007. 34: pp. 77-83.

[Chetelat 2003] Chetelat, G. and Baron, J.C., *Early diagnosis of Alzheimer's disease: contribution of structural neuroimaging.* Neuroimage, 2003. 18(2): pp. 525-541.

[Chupin 2007] Chupin, M., Mukuna-Bantumbakulu, A.R., Hasboun, D., Bardinet, E., Baillet, S., Kinkingnehun, S., Lemieux, L., Dubois, B., and Garnero, L., *Anatomically constrained region deformation for the automated segmentation of the hippocampus and the amygdala: Method and validation on controls and patients with Alzheimer's disease.* NeuroImage, 2007. 34(3): pp. 996-1019.

[Cocosco 1997] Cocosco, C.A., Kollokian, V., Kwan, R.K.S., and Evans, A.C., *BrainWeb: Online interface to a 3D MRI simulated brain database.* Neuroimage, 1997. 5(4): pp. S425.

[Colliot 2008] Colliot, O., Chetelat, G., Chupin, M., Desgranges, B., Magnin, B., Benali, H., Dubois, B., Garnero, L., Eustache, F., and Lehericy, S., *Discrimination between Alzheimer disease, mild cognitive impairment, and normal aging by using automated segmentation of the hippocampus.* Radiology, 2008. 248(1): pp. 194-201.

[Crum 1993] Crum, R., Anthony, J., Bassett, S., and Folstein, M., *Population-based norms for the Mini-Mental State Examination by age and educational level.* JAMA, 1993. 269(18): pp. 2386-2391.

[Dale 1999] Dale, A.M., Fischl, B., and Sereno, M.I., *Cortical surface-based analysis I. Segmentation and surface reconstruction.* Neuroimage, 1999. 9(2): pp. 179-194.

[de Leon 2001] de Leon, M.J., Convit, A., Wolf, O.T., Tarshish, C.Y., DeSanti, S., Rusinek, H., Tsui, W., Kandil, E., Scherer, A.J., and Roche, A., *Prediction of cognitive decline in normal elderly subjects with 2-[18F] fluoro-2-deoxy-D-glucose/positron-emission tomography (FDG/PET).* Proceedings of the National Academy of Sciences, 2001. 98(19): pp. 10966-10971.

[Desikan 2009] Desikan, R., Cabral, H., Hess, C., Dillon, W., Glastonbury, C., Weiner, M., Schmansky, N., Greve, D., Salat, D., and Buckner, R., *Automated MRI measures identify individuals with mild cognitive impairment and Alzheimer's disease.* Brain, 2009. 132(8): pp. 2048-2057.

[Dettori 2007] Dettori, L. and Semler, L., *A comparison of wavelet, ridgelet, and curvelet-based texture classification algorithms in computed tomography.* Computers in Biology and Medicine, 2007. 37(4): pp. 486-498.

[Ding 2005] Ding, F., Leow, W.K., and Wang, S., *Segmentation of 3D CT volume images using a single 2D atlas.* Lecture Notes in Computer Science, 2005. 3765: pp. 459-468.

[Duan 2006] Duan, J., Wang, H., Xu, J., Lin, X., Chen, S., Kang, Z., and Yao, Z., *White matter damage of patients with Alzheimer's disease correlated with the decreased cognitive function.* Surgical and Radiologic Anatomy, 2006. 28(2): pp. 150-156.

[Economics 2005] Economics, *Dementia estimates and projections: Australian states and territories.* Report by Access Economics for Alzheimer's Australia, 2005.

[Estrada 2009] Estrada, L. and Soto, C., *Strategies for Alzheimer's disease diagnosis*. Current Hypotheses and Research Milestones in Alzheimer's Disease. 2009.

[Etkin 2007] Etkin, A. and Wager, T., *Functional neuroimaging of anxiety: a meta-analysis of emotional processing in PTSD, social anxiety disorder, and specific phobia.* American Journal of Psychiatry, 2007. 164(10): pp. 1476-1488.

[Fan 2008] Fan, Y., Batmanghelich, N., Clark, C., and Davatzikos, C., *Spatial patterns of brain atrophy in MCI patients, identified via high-dimensional pattern classification, predict subsequent cognitive decline.* Neuroimage, 2008. 39(4): pp. 1731-1743.

[Folstein 1975] Folstein, M., Folstein, S., and McHugh, P., *Mini-Mental State: a practical method for grading the cognitive state of patients for the clinician.* J Psychiatr Res, 1975. 12(3): pp. 189-198.

[Foster 2002] Foster, N., Heidebrink, J., and Clark, C., *Inter-rater reliability and diagnostic accuracy of FDG-PET is superior to clinical history and examination in dementia.* Neurobiol Aging, 2002. 23: pp. S353.

[Foster 2007] Foster, N.L., Wang, A.Y., Tasdizen, T., Fletcher, P.T., Hoffman, J.M., and Koeppe, R.A., *Realizing the potential of positron emission tomography with 18F-fluorodeoxyglucose to improve the treatment of Alzheimer's disease.* Alzheimer's & Dementia: The Journal of the Alzheimer's Association, 2007. 4(1 Suppl 1): pp. S29-36.

[Fox 1996] Fox, N.C., Freeborough, P.A., and Rossor, M.N., *Visualisation and quantification of rates of atrophy in Alzheimer's disease.* Lancet, 1996. 348(9020): pp. 94-97.

[Frisoni 2009] Frisoni, G., *Neuro-imaging: Structural and functional imaging.* The Journal of Nutrition, Health and Aging, 2009. 13(4): pp. 348-349.

[Frisoni 1999] Frisoni, G.B., Laakso, M.P., Beltramello, A., Geroldi, C., Bianchetti, A., Soininen, H., and Trabucchi, M., *Hippocampal and entorhinal cortex atrophy in frontotemporal dementia and Alzheimer's disease.* Neurology, 1999. 52(1): pp. 91-100.

[Friston 1995] Friston, K.J., Holmes, A.P., Worsley, K.J., Poline, J.B., Frith, C.D., and Frackowiak, R.S.J., *Statistical parametric maps in functional imaging: a general linear approach.* Human Brain Mapping, 1995. 2(4): pp. 189-210.

[Gholipour 2007] Gholipour, A., Kehtarnavaz, N., Briggs, R., Devous, M., and Gopinath, K., *Brain functional localization: A survey of image registration techniques.* IEEE transactions on Medical Imaging, 2007. 26(4): pp. 427-451.

[Gilman 2005] Gilman, S., Koeppe, R.A., Little, R., An, H., Junck, L., Giordani, B., Persad, C., Heumann, M., and Wernette, K., *Differentiation of Alzheimer's disease from dementia with Lewy bodies utilizing positron emission tomography with [18F] fluorodeoxyglucose and neuropsychological testing.* Experimental Neurology, 2005. 191: pp. 95-103.

[Grafton 1992] Grafton, S., Mazziotta, J., Presty, S., Friston, K., Frackowiak, R., and Phelps, M., *Functional anatomy of human procedural learning determined with regional cerebral blood flow and PET.* Journal of Neuroscience, 1992. 12(7): pp. 2542-2548.

[Habra 2010] Habra, M., N ez, R., Chuang, H., Ayala-Ramirez, M., Rich, T., Kyle, K., and Jimenez, C., *Fatal hypoglycemia in malignant pheochromocytoma: direct glucose consumption as suggested by 18 F-2-fluoro-2-deoxy-d-glucose positron emission tomography/computed tomography imaging.* Endocrine, 2010. 37(1): pp. 209-212.

[Harper 2005] Harper, P., *A review and comparison of classification algorithms for medical decision making.* Health Policy, 2005. 71(3): pp. 315-331.

[Henry-Feugeas 2007] Henry-Feugeas, M.C., *MRI of the 'Alzheimer syndrome'.* J Neuroradiol, 2007. 34(4): pp. 220-227.

[Hoffman 2000] Hoffman, J.M., Welsh-Bohmer, K.A., Hanson, M., Crain, B., Hulette, C., Earl, N., and Coleman, R.E., *FDG PET imaging in patients with pathologically verified dementia.* J Nucl Med, 2000. 41(11): pp. 1920-1928.

[Hu 2003] Hu, Q. and Nowinski, W.L., *A rapid algorithm for robust and automatic extraction of the midsagittal plane of the human cerebrum from neuroimages based on local symmetry and outlier removal.* NeuroImage, 2003. 20(4): pp. 2153-2165.

[Hu 2005a] Hu, Q., Qian, G., Aziz, A., and Nowinski, W.L., *Segmentation of brain from computed tomography head images*, in *Engineering in Medicine and Biology Society, 2005. IEEE-EMBS 2005. 27th Annual International Conference*: Shanghai, China. pp. 3375-3378.

[Hu 2005b] Hu, Q., Qian, G., and Nowinski, W.L., *Fast, accurate, and automatic extraction of the modified Talairach cortical landmarks from magnetic resonance images.* Magnetic Resonance in Medicine, 2005. 53(4): pp. 970-976.

[Hu 2008] Hu, Q., Qian, G., Teistler, M., and Huang, S., *Automatic and adaptive brain morphometry on MR images.* Radiographics, 2008. 28(2): pp. 345-356.

[Hunt 2007] Hunt, A., Schonknecht, P., Henze, M., Seidl, U., Haberkorn, U., and Schroder, J., *Reduced cerebral glucose metabolism in patients at risk for Alzheimer's disease.* Psychiatry Research: Neuroimaging, 2007. 155(2): pp. 147-154.

[Ishii 1996] Ishii, K., *Decreased medial temporal oxygen metabolism in Alzheimer's disease shown by PET*. 1996, Soc Nuclear Med. pp. 1159-1165.

[Ishii 2006] Ishii, K., Kono, A.K., Sasaki, H., Miyamoto, N., Fukuda, T., Sakamoto, S., and Mori, E., *Fully automatic diagnostic system for early-and late-*

onset mild Alzheimer's disease using FDG PET and 3D-SSP. European Journal of Nuclear Medicine and Molecular Imaging, 2006. 33(5): pp. 575-583.

[Ishii 2005] Ishii, K., Sasaki, H., Kono, A.K., Miyamoto, N., Fukuda, T., and Mori, E., *Comparison of gray matter and metabolic reduction in mild Alzheimer's disease using FDG-PET and voxel-based morphometric MR studies.* European Journal of Nuclear Medicine and Molecular Imaging, 2005. 32(8): pp. 959-963.

[Ishii 2001] Ishii, K., Willoch, F., Minoshima, S., Drzezga, A., Ficaro, E.P., Cross, D.J., Kuhl, D.E., and Schwaiger, M., *Statistical brain mapping of 18F-FDG PET in Alzheimer's disease: validation of anatomic standardization for atrophied brains.* J Nucl Med, 2001. 42(4): pp. 548-557.

[Jack 2000] Jack, C.R., Petersen, R.C., Xu, Y., O'Brien, P.C., Smith, G.E., Ivnik, R.J., Boeve, B.F., Tangalos, E.G., and Kokmen, E., *Rates of hippocampal atrophy correlate with change in clinical status in aging and AD.* Neurology, 2000. 55(4): pp. 484-490.

[Jack 1999] Jack, C.R., Petersen, R.C., Xu, Y.C., O'Brien, P.C., Smith, G.E., Ivnik, R.J., Boeve, B.F., Waring, S.C., Tangalos, E.G., and Kokmen, E., *Prediction of AD with MRI-based hippocampal volume in mild cognitive impairment.* Neurology, 1999. 52(7): pp. 1397-1403.

[Jack 2004] Jack, C.R., Shiung, M.M., Gunter, J.L., O'Brien, P.C., Weigand, S.D., Knopman, D.S., Boeve, B.F., Ivnik, R.J., Smith, G.E., and Cha, R.H., *Comparison of different MRI brain atrophy rate measures with clinical disease progression in AD.* Neurology, 2004. 62(4): pp. 591-600.

[Jack Jr 2008] Jack Jr, C., Bernstein, M., Fox, N., Thompson, P., Alexander, G., Harvey, D., Borowski, B., Britson, P., Whitwell, J., and Ward, C., *The Alzheimer's disease neuroimaging initiative (ADNI): MRI methods.* Journal of magnetic resonance imaging: JMRI, 2008. 27(4): pp. 685.

[Jack Jr 1998] Jack Jr, C.R., *Rate of medial temporal lobe atrophy in typical aging and Alzheimer's disease.* Neurology, 1998. 51(4): pp. 993-999.

[Jack Jr 1997] Jack Jr, C.R., Petersen, R.C., Xu, Y.C., Waring, S.C., O'Brien, P.C., Tangalos, E.G., Smith, G.E., Ivnik, R.J., and Kokmen, E., *Medial temporal atrophy on MRI in normal aging and very mild Alzheimer's disease.* Neurology, 1997. 49(3): pp. 786-794.

[Jagust 2006] Jagust, W., Gitcho, A., Sun, F., Kuczynski, B., Mungas, D., and Haan, M., *Brain imaging evidence of preclinical Alzheimer's disease in normal aging.* Ann Neurol, 2006. 59(4): pp. 673-681.

[Jagust 1993] Jagust, W.J., Eberling, J.L., Richardson, B.C., Reed, B.R., Baker, M.G., Nordahl, T.E., and Budinger, T.F., *The cortical topography of temporal lobe hypometabolism in early Alzheimer's disease.* Brain Res, 1993. 629(2): pp. 189-198.

[Jalbert 2008] Jalbert, J., Daiello, L., and Lapane, K., *Dementia of the Alzheimer type.* Epidemiologic Reviews, 2008. 30(1): pp. 15-34.

[Johansen-Berg 2009] Johansen-Berg, H., *Imaging the relationship between structure, function and behaviour in the human brain.* Brain Structure and Function, 2009. 213(6): pp. 499-500.

[Johnson 1988] Johnson, R.A. and Wichern, D.W., *Applied multivariate statistical analysis*. 1988: Prentice-Hall, Inc. Upper Saddle River, NJ, USA.

[Kato 2001] Kato, T., Knopman, D., and Liu, H., *Dissociation of regional activation in mild AD during visual encoding: a functional MRI study.* Neurology, 2001. 57(5): pp. 812-816.

[Kawano 2000] Kawano, M., Ichimiya, A., Ogomori, K., Kuwabara, Y., Sasaki, M., Yoshida, T., and Tashiro, N., *Relationship between both IQ and Mini-Mental State Examination and the regional cerebral glucose metabolism in clinically diagnosed Alzheimer's disease: a PET study.* Dementia and geriatric cognitive disorders, 2000. 12(2): pp. 171-176.

[Kaye 1997] Kaye, J.A., Swihart, T., Howieson, D., Dame, A., Moore, M.M., Karnos, T., Camicioli, R., Ball, M., Oken, B., and Sexton, G., *Volume loss of the hippocampus and temporal lobe in healthy elderly persons destined to develop dementia.* Neurology, 1997. 48(5): pp. 1297-1304.

[Kerrouche 2006] Kerrouche, N., Herholz, K., Mielke, R., Holthoff, V., and Baron, J.C., *18FDG PET in vascular dementia: differentiation from Alzheimer's disease using voxel-based multivariate analysis.* J Cereb Blood Flow Metab, 2006. 26(9): pp. 1213-1221.

[Kim 2005] Kim, E.J., Cho, S.S., Jeong, Y., Park, K.C., Kang, S.J., Kang, E., Kim, S.E., Lee, K.H., and Na, D.L., *Glucose metabolism in early onset versus late onset Alzheimer's disease: an SPM analysis of 120 patients.* Brain, 2005. 128(8): pp. 1790-1801.

[Klauschen 2009] Klauschen, F., Goldman, A., Barra, V., Meyer-Lindenberg, A., and Lundervold, A., *Evaluation of automated brain MR image segmentation and volumetry methods.* Hum Brain Mapp, 2009. 30(4): pp. 1310-1327.

[Kober 2008] Kober, H., Barrett, L., Joseph, J., Bliss-Moreau, E., Lindquist, K., and Wager, T., *Functional grouping and cortical-subcortical interactions in emotion: A meta-analysis of neuroimaging studies.* Neuroimage, 2008. 42(2): pp. 998-1031.

[Koivistoinen 2004] Koivistoinen, H., Tohka, J., and Ruotsalainen, U. *Comparison of pattern classification methods in segmentation of dynamic PET brain images*. in Proceedings of the 6th Nordic Signal Processing Symposium - NORSIG 2004. 2004. Espoo, Finland. pp. 73-76.

[Kono 2007] Kono, A.K., Ishii, K., Sofue, K., Miyamoto, N., Sakamoto, S., and Mori, E., *Fully automatic differential diagnosis system for dementia with Lewy bodies and Alzheimer's disease using FDG-PET and 3D-SSP.* European Journal of Nuclear Medicine and Molecular Imaging, 2007. 34(9): pp. 1490-1497.

[Koopman 2009] Koopman, K., Le Bastard, N., Martin, J., Nagels, G., De Deyn, P., and Engelborghs, S., *Improved discrimination of autopsy-confirmed Alzheimer's disease (AD) from non-AD dementias using CSF P-tau181P.* Neurochemistry International, 2009. 55(4): pp. 214-218.

[Kushner 1987] Kushner, M., Tobin, M., Alavi, A., Chawluk, J., Rosen, M., Fazekas, F., Alavi, J., and Reivich, M., *Cerebellar glucose consumption in normal and pathologic states using fluorine-FDG and PET.* Journal of Nuclear Medicine, 1987. 28(11): pp. 1667-1670.

[Laakso 2000] Laakso, M.P., Lehtovirta, M., Partanen, K., Riekkinen, P.J., and Soininen, H., *Hippocampus in Alzheimer's disease: a 3-year follow-up MRI study.* Biological Psychiatry, 2000. 47(6): pp. 557-561.

[Langbaum 2009] Langbaum, J.B.S., Chen, K., Lee, W., Reschke, C., Bandy, D., Fleisher, A.S., Alexander, G.E., Foster, N.L., Weiner, M.W., and Koeppe, R.A., *Categorical and correlational analyses of baseline fluorodeoxyglucose positron emission tomography images from the Alzheimer's Disease Neuroimaging Initiative (ADNI).* Neuroimage, 2009. 45(4): pp. 1107-1116.

[Lawes 2008] Lawes, I.N.C., Barrick, T.R., Murugam, V., Spierings, N., Evans, D.R., Song, M., and Clark, C.A., *Atlas-based segmentation of white matter tracts of the human brain using diffusion tensor tractography and comparison with classical dissection.* NeuroImage, 2008. 39(1): pp. 62-79.

[Lei 1992] Lei, T. and Sewchand, W., *Statistical approach to X-ray CT imaging and its applications in image analysis. II. A new stochastic model-based image segmentation technique for X-ray CT image.* Medical Imaging, IEEE Transactions on, 1992. 11(1): pp. 62-69.

[Lemieux 1999] Lemieux, L., Hagemann, G., Krakow, K., and Woermann, F.G., *Fast, accurate, and reproducible automatic segmentation of the brain in T 1-weighted volume MRI data.* Magnetic Resonance in Medicine, 1999. 42(1): pp. 127-135.

[Lockwood 2002] Lockwood, A., Weissenborn, K., Bokemeyer, M., Tietge, U., and Burchert, W., *Correlations between cerebral glucose metabolism and*

neuropsychological test performance in nonalcoholic cirrhotics. Metabolic brain disease, 2002. 17(1): pp. 29-40.

[Loncaric 1997] Loncaric, S. and Kovacevic, D., *A method for segmentation of CT head images*, in *Proceedings of the 9th International Conference on Image Analysis and Processing-Volume II*. 1997: Florence, Italy. pp. 388-395.

[Lorensen 1987] Lorensen, W.E. and Cline, H.E., *Marching cubes: A high resolution 3D surface construction algorithm.* Proceedings of the 14th annual conference on Computer graphics and interactive techniques, 1987. 21(4): pp. 163-169.

[Luo 2006] Luo, S., *Automated Medical Image Segmentation Using a New Deformable Surface Model.* International Journal of Computer Science and Network Security, 2006. 6(5A): pp. 109-115.

[Matesin 2001] Matesin, M., Loncaric, S., and Petravic, D., *A rule-based approach to stroke lesion analysis from CT brainimages.* Proceedings of the 2nd International Symposium on Image and Signal Processing and Analysis, ISPA, 2001: pp. 219-223.

[Matsuda 2007] Matsuda, H., *Symposium: Brain imaging and neuropathology The role of neuroimaging in mild cognitive impairment.* Neuropathology, 2007. 27(6): pp. 570-577.

[Mazziotta 1992] Mazziotta, J.C., Frackowiak, R.S., and Phelps, M.E., *The use of positron emission tomography in the clinical assessment of dementia.* Semin Nucl Med, 1992. 22(4): pp. 233-246.

[McColl 1994] McColl, J., Holmes, A., and Ford, I., *Statistical methods in neuroimaging with particular application to emission tomography.* Statistical methods in medical research, 1994. 3(1): pp. 63-86.

[McLachlan 1997] McLachlan, G.J. and Krishnan, T., *The EM algorithm and extensions*. 1997: Wiley.

[Minoshima 1994] Minoshima, S., *Anatomic standardization: linear scaling and nonlinear warping of functional brain images*. 1994, Soc Nuclear Med. pp. 1528-1537.

[Minoshima 1995] Minoshima, S., Frey, K.A., Koeppe, R.A., Foster, N.L., and Kuhl, D.E., *A diagnostic approach in Alzheimer's disease using three-dimensional stereotactic surface projections of fluorine-18-FDG PET.* J Nucl Med, 1995. 36(7): pp. 1238-1248.

[Minoshima 1997] Minoshima, S., Giordani, B., Berent, S., Frey, K.A., Foster, N.L., and Kuhl, D.E., *Metabolic reduction in the posterior cingulate cortex in very early Alzheimer's disease.* Annals of Neurology, 1997. 42(1): pp. 85-94.

[Morard 1994] Morard, M., Tcherekayev, V., and de Tribolet, N., *The superior orbital fissure: A microanatomical study.* Neurosurgery, 1994. 35(6): pp. 1087-1093.

[Morris 1993] Morris, J., *The Clinical Dementia Rating (CDR): current version and scoring rules.* Neurology, 1993. 43(11): pp. 2412-2414.

[Mosconi 2005] Mosconi, L., *Brain glucose metabolism in the early and specific diagnosis of Alzheimer's disease.* European Journal of Nuclear Medicine and Molecular Imaging, 2005. 32(4): pp. 486-510.

[Mosconi 2007] Mosconi, L., Tsui, W.H., Pupi, A., De Santi, S., Drzezga, A., Minoshima, S., and de Leon, M.J., *18F-FDG PET Database of Longitudinally Confirmed Healthy Elderly Individuals Improves Detection of Mild Cognitive Impairment and Alzheimer's Disease.* Journal of Nuclear Medicine, 2007. 48(7): pp. 1129.

[Mulenbruch 2006] Mulenbruch, G., Das, M., Hohl, C., Wildberger, J.E., Rinck, D., Flohr, T.G., Koos, R., Knackstedt, C., Gunther, R.W., and Mahnken, A.H., *Global left ventricular function in cardiac CT. Evaluation of an automated 3D region-growing segmentation algorithm.* European Radiology, 2006. 16(5): pp. 1117-1123.

[Mykkanen 2000] Mykkanen, J.M., Juhola, M., and Ruotsalainen, U., *Extracting VOIs from brain PET images.* International Journal of Medical Informatics, 2000. 58-59: pp. 51-57.

[Nowinski 2001a] Nowinski, W.L., *Computerized brain atlases for surgery of movement disorders.* Seminars in Neurosurgery, 2001. 12(2): pp. 183-194.

[Nowinski 2001b] Nowinski, W.L., *Modified Talairach landmarks.* Acta Neurochirurgica, 2001. 143(10): pp. 1045-1057.

[Nowinski 2002] Nowinski, W.L., *Electronic Brain Atlases: Features and Applications*, in 3D Image Processing: Techniques and Clinical Applications. 2002, Springer. pp. 79-93.

[Nowinski 2008] Nowinski, W.L., Qian, G., Prakash, K.N.B., Volkau, I., Leong, W.K., Huang, S., Ananthasubramaniam, A., Liu, J., Ng, T.T., and Gupta, V., *Stroke Suite: CAD systems for acute ischemic stroke, hemorrhagic stroke, and stroke in ER.* Lecture Notes In Computer Science, 2008. 4987: pp. 377-386.

[Okamura 2001] Okamura, N., Arai, H., Higuchi, M., Tashiro, M., Matsui, T., Hu, X.S., Takeda, A., Itoh, M., and Sasaki, H., *[18F] FDG-PET study in dementia with Lewy bodies and Alzheimer's disease.* Prog Neuropsychopharmacol Biol Psychiatry, 2001. 25(2): pp. 447-456.

[Pardo 1997] Pardo, J.M., Cabello, D., and Heras, J., *A snake for model-based segmentation of biomedical images.* Pattern Recognition Letters, 1997. 18(14): pp. 1529-1538.

[Perneczky 2006] Perneczky, R., Drzezga, A., Diehl-Schmid, J., Schmid, G., Wohlschlager, A., Kars, S., Grimmer, T., Wagenpfeil, S., Monsch, A., and Kurz, A., *Schooling mediates brain reserve in Alzheimer's disease: findings of fluoro-deoxy-glucose-positron emission tomography.* Journal of Neurology, Neurosurgery & Psychiatry, 2006. 77(9): pp. 1060-1063.

[Petersen 2009] Petersen, R., *Early diagnosis of Alzheimers disease: is MCI too late?* Current Alzheimer Research, 2009. 6(4): pp. 324-330.

[Petrella 2003] Petrella, J.R., Coleman, R.E., and Doraiswamy, P.M., *Neuroimaging and early diagnosis of Alzheimer disease: a look to the future.* Radiology, 2003. 226(2): pp. 315-336.

[Pham 2000] Pham, D.L., Xu, C., and Prince, J.L., *A survey of current methods in medical image segmentation.* Annual Review of Biomedical Engineering, 2000. 2: pp. 315-337.

[Pohle 2001] Pohle, R. and Toennies, K.D., *Segmentation of medical images using adaptive region growing.* Proc. SPIE Medical Imaging, 2001: pp. 1337-1346.

[Qian 2010a] Qian, G., Luo, S., Jin, J., and Nowinski, W.L., *Extended Talairach landmarks on neuroimages for atlas registration*, in *The 4th International Conference on Bioinformatics and Biomedical Engineering (iCBBE 2010)*: Chengdu, China, June 18-20, Volume 2, paper 40935.

[Qian 2008] Qian, G., Luo, S., Jin, J., Park, M., and Nowinski, W.L. *Interactive and intelligent approach for brain extraction from high-resolution volumetric MR neuroimages*. in International Symposium on Intelligent Information Technology Application. 2008. Shanghai, China, Dec 20-22. pp. 885-889.

[Qian 2009a] Qian, G., Luo, S., Jin, J., Park, M., and Nowinski, W.L., *Automated and domain knowledge-based brain extraction from CT head scans.* International Journal of Computer Aided Engineering and Technology, 2009. 1(4): pp. 480-493.

[Qian 2009b] Qian, G., Luo, S., Jin, J., Park, M., and Nowinski, W.L., *A fast and automatic approach to extract the brain and midsagittal lines from FDG-PET head scans*, in *The 1st International Conference on Information Science and Engineering*: Nanjing, China, Dec 18-20, 2009. pp. 1035-1038.

[Qian 2010b] Qian, G., Shen, X., Luo, S., Jin, J., and Nowinski, W.L., *Rapid and automatic atlas-based approach of Alzheimer's disease assessment by positron emission tomography neuroimages*, in *The 9th IEEE International Conference on Cognitive Informatics (ICCI 2010)*: July 7-9, 2010, Beijing, China, pp.375-382.

[Querbes 2009] Querbes, O., Aubry, F., Pariente, J., Lotterie, J., Demonet, J., Duret, V., Puel, M., Berry, I., Fort, J., and Celsis, P., *Early diagnosis of Alzheimer's disease using cortical thickness: impact of cognitive reserve.* Brain, 2009. 132(8): pp. 20362-47.

[Robb 1990] Robb, R.A., Hanson, D.P., and Found, M. *ANALYZE: A software system for biomedical image analysis*. 1990. pp. 507-518.

[Ryu 2008] Ryu, E.K. and Chen, X., *Development of Alzheimer's disease imaging agents for clinical studies.* Front Biosci, 2008. 13: pp. 777-789.

[Sandor 1991] Sandor, T., Metcalf, D., and Kim, Y.-J., *Segmentation of brain CT images using the concept of region growing.* International Journal of Bio-Medical Computing, 1991. 29(2): pp. 133-147.

[Saykin 1999] Saykin, A.J., Flashman, L.A., Frutiger, S.A., Johnson, S.C., Mamourian, A.C., Moritz, C.H., O'Jile, J.R., Riordan, H.J., Santulli, R.B., and Smith, C.A., *Neuroanatomic substrates of semantic memory impairment in Alzheimer's disease: Patterns of functional MRI activation.* Journal of the International Neuropsychological Society, 1999. 5(05): pp. 377-392.

[Schroeder 2004] Schroeder, W., Martin, K., and Lorensen, B., *The visualization toolkit an object-oriented approach to 3D graphics.* Kitware, 2004.

[Senda 2002] Senda, M., Kimura, Y., and Herscovitch, P., *Brain imaging using PET*. 2002: Academic Press.

[Shan 2005] Shan, Z.Y., Ji, Q., Gajjar, A., and Reddick, W.E., *A knowledge-guided active contour method of segmentation of cerebella on MR images of pediatric patients with medulloblastoma.* Journal of Magnetic Resonance Imaging, 2005. 21(1): pp. 1-11.

[Shan 2002] Shan, Z.Y., Yue, G.H., and Liu, J.Z., *Automated histogram-based brain segmentation in T1-weighted three-dimensional magnetic resonance head images.* Neuroimage, 2002. 17(3): pp. 1587-1598.

[Shattuck 2002] Shattuck, D.W. and Leahy, R.M., *BrainSuite: An automated cortical surface identification tool.* Medical Image Analysis, 2002. 6(2): pp. 129-142.

[Shreiner 2005] Shreiner, D., Woo, M., Neider, J., and Davis, T., *OpenGL programming guide: the official guide to learning OpenGL, version 2*. 2005, Boston: Addison-Wesley Professional.

[Sigel 2006] Sigel, A., Sigel, H., and Sigel, R., *Neurodegenerative diseases and metal ions*. 2006: Wiley.

[Silverman 2001] Silverman, D.H., Small, G.W., Chang, C.Y., Lu, C.S., Kung De Aburto, M.A., Chen, W., Czernin, J., Rapoport, S.I., Pietrini, P., and Alexander, G.E., *Positron emission tomography in evaluation of dementia: Regional brain metabolism and long-term outcome.* JAMA, 2001. 286(17): pp. 2120-2127.

[Solms 2002] Solms, M. and Turnbull, O., *The brain and the inner world: An introduction to the neuroscience of subjective experience*. 2002: Other Press, LLC.

[Soltanian-Zadeh 1997] Soltanian-Zadeh, H. and Windham, J.P., *A multiresolution approach for contour extraction from brain images.* Medical Physics, 1997. 24(12): pp. 1844-1853.

[Sonka 1994] Sonka, M., Sundaramoorthy, G., and Hoffman, E.A., *Knowledge-based segmentation of intrathoracic airways from multidimensional high resolution CT images.* Proceedings of SPIE, Volume 2168, Medical Imaging, 1994: pp. 73-85.

[Stokking 2000] Stokking, R., Vincken, K.L., and Viergever, M.A., *Automatic morphology-based brain segmentation (MBRASE) from MRI-T1 data.* Neuroimage, 2000. 12(6): pp. 726-738.

[Takagi 2004] Takagi, S., Takahashi, W., Shinohara, Y., Yasuda, S., Ide, M., Shohtsu, A., and Seio, T., *Quantitative PET cerebral glucose metabolism estimates using a single non-arterialized venous-blood sample.* Annals of Nuclear Medicine, 2004. 18(4): pp. 297-302.

[Talairach 1988] Talairach, J. and Tournoux, P., *Co-planar stereotaxic atlas of the human brain*. 1988: Thieme New York.

[Teipel 2003] Teipel, S.J., Bayer, W., Alexander, G.E., Bokde, A.L.W., Zebuhr, Y., Teichberg, D., Muller-Spahn, F., Schapiro, M.B., Moller, H.J., and Rapoport, S.I., *Regional pattern of hippocampus and corpus callosum atrophy in*

Alzheimer's disease in relation to dementia severity: evidence for early neocortical degeneration. Neurobiology of Aging, 2003. 24(1): pp. 85-94.

[Teipel 2006] Teipel, S.J., Drzezga, A., Bartenstein, P., Moller, H.J., Schwaiger, M., and Hampel, H., *Effects of donepezil on cortical metabolic response to activation during 18 FDG-PET in Alzheimer's disease: a double-blind cross-over trial.* Psychopharmacology, 2006. 187(1): pp. 86-94.

[Terminology 1999] Terminology, F.C.o.A., *Terminologia Anatomica*. 1999: Thieme, Stuttgart - New York.

[Thompson 2004] Thompson, P., Hayashi, K., de Zubicaray, G., Janke, A., Rose, S., Semple, J., Hong, M., Herman, D., Gravano, D., and Doddrell, D., *Mapping hippocampal and ventricular change in Alzheimer disease.* Neuroimage, 2004. 22(4): pp. 1754-1766.

[Toga 2006] Toga, A.W., Thompson, P.M., Mori, S., Amunts, K., and Zilles, K., *Towards multimodal atlases of the human brain.* Nature Reviews Neuroscience, 2006. 7(12): pp. 952-966.

[Townsend 2001] Townsend, D.W. and Cherry, S.R., *Combining anatomy and function: the path to true image fusion.* European Radiology, 2001. 11(10): pp. 1968-1974.

[Ushijima 2002] Ushijima, Y., Okuyama, C., Mori, S., Nakamura, T., Kubota, T., and Nishimura, T., *Relationship between cognitive function and regional cerebral blood flow in Alzheimer's disease.* Nuclear medicine communications, 2002. 23(8): pp. 779-784.

[Van 2001] Van De Graaff, K.M., *Human Anatomy, Sixth edition*. 2001: McGraw-Hill.

[von 2006] von Borczyskowski, D., Wilke, F., Martin, B., Brenner, W., Clausen, M., Mester, J., and Buchert, R., *Evaluation of a new expert system for fully automated detection of the Alzheimer's dementia pattern in FDG PET.* Nucl Med Commun, 2006. 27(9): pp. 739-743.

[Waldemar 2006] Waldemar, G., Dubois, B., Emre, M., Georges, J., McKeith, I., Rossor, M., Scheltens, P., Tariska, P., and Winblad, B., *Alzheimer's disease and other disorders associated with dementia*, in R. Hughes et al. European handbook of neurological management. Oxford. Blackwell Publishing. 2006. pp. 266-298.

[Wang 2007] Wang, Y., Chiu, E., Rosenberg, J., and Gambhir, S.S., *Standardized uptake value atlas: characterization of physiological 2-deoxy-2-[18 F] fluoro-D-glucose uptake in normal tissues.* Molecular Imaging and Biology, 2007. 9(2): pp. 83-90.

[Weber 2000] Weber, W., Schwaiger, M., and Avril, N., *Quantitative assessment of tumor metabolism using FDG-PET imaging.* Nuclear medicine and biology, 2000. 27(7): pp. 683-687.

[Wegner 1996] Wegner, S., Harms, T., Oswald, H., and Fleck, E., *The watershed transformation on graphs for the segmentation of CT images*, in *Proc. of the 13th ICPR*. 1996: Vienna, Austria. pp. 498-502.

[Whitwell 2008] Whitwell, J.L., Jack, C.R., Pankratz, V.S., Parisi, J.E., Knopman, D.S., Boeve, B.F., Petersen, R.C., Dickson, D.W., and Josephs, K.A., *Rates of*

brain atrophy over time in autopsy-proven frontotemporal dementia and Alzheimer disease. Neuroimage, 2008. 39(3): pp. 1034-1040.

[Wong 2002] Wong, K.P., Feng, D., Meikle, S.R., and Fulham, M.J., *Segmentation of dynamic PET images using cluster analysis.* Nuclear Science, IEEE Transactions on, 2002. 49(1): pp. 200-207.

[Xuan 1995] Xuan, J., Adali, T., and Wang, Y. *Segmentation of magnetic resonance brain image: integrating region growing and edge detection*. in International Conference on Image Processing (ICIP'95). 1995. Washington D.C. pp. 3544.

[Zahn 2004] Zahn, R., Juengling, F., Bubrowski, P., Jost, E., Dykierek, P., Talazko, J., and Huell, M., *Hemispheric asymmetries of hypometabolism associated with semantic memory impairment in Alzheimer's disease: a study using positron emission tomography with fluorodeoxyglucose-F18.* Psychiatry Research: Neuroimaging, 2004. 132(2): pp. 159-172.

[Zakzanis 2003] Zakzanis, K.K., Graham, S.J., and Campbell, Z., *A meta-analysis of structural and functional brain imaging in dementia of the Alzheimer's type: A neuroimaging profile.* Neuropsychology Review, 2003. 13(1): pp. 1-18.

[Zincirkeser 2007] Zincirkeser, S., Sahin, E., Halac, M., and Sager, S., *Standardized uptake values of normal organs on 18 F-fluorodeoxyglucose positron emission tomography and computed tomography imaging.* Journal of international medical research, 2007. 35(2): pp. 231-236.

List of Thesis-related Publications

Journals

1. Qian, G., Luo, S., Jin, J., Park, M., and Nowinski, W.L., "*Automated and domain knowledge-based brain extraction from CT head scans*", International Journal of Computer Aided Engineering and Technology, vol. 1, pp. 480-493, 2009.

2. Qian, G., Luo, S., Jin, J., Park, M., and Nowinski, W.L., "*An interactive post-processing platform for brain extraction from volumetric MR neuroimages*", Journal of Computers, accepted on 11 Feb 2009.

3. Qian, G., Luo, S., Jin, J., Park, M., Li, J., and Nowinski, W.L., "*Fast and automated extraction of cerebral hemispheres from volumetric FDG-PET scans*", Journal of Communications, submitted on 15 Nov 2009.

4. Hu, Q., Luo, S., Qiao, Y., Qian, G., "*Supervised grayscale thresholding based on transition regions*", Image and Vision Computing, 2008, 26(12), pp. 1677-1684.

Conferences

1. Qian, G., Luo, S., Jin, J., Park, M., and Nowinski, W.L., "*Extraction of the brain from CT head scans based on domain knowledge*", 2007 International Symposium on Computational Models for Life Sciences (CMLS'07), Dec 17-19, 2007, Gold Coast, Queensland, Australia. AIP Conference Proceedings, Volume 952, pp. 76-85.

2. Qian, G., Luo, S., Jin, J., Park, M., and Nowinski, W.L., "*Interactive and intelligent approach for brain extraction from high-resolution volumetric MR neuroimages*", 2008 International Symposium on Intelligent Information Technology Application (IITA 2008) Dec. 21-22, 2008, Shanghai, China, Volume 2, pp.885-889.

3. Qian, G., Luo, S., Jin, J., Park, M., Li, J., and Nowinski, W.L., "*A fast and automatic approach to extract the brain and midsagittal lines from FDG-PET head scans*", The 1st International Conference on Information Science and Engineering (ICISE2009), Dec 18-20, 2009, Nanjing, China, pp.1035-1038.

4. Qian, G., Luo, S., Jin, J., and Nowinski, W.L., "*Extended Talairach landmarks on neuroimages for atlas registration*", The 4th International Conference on Bioinformatics and Biomedical Engineering (iCBBE 2010), Jun 18-20, 2010, Chengdu, China, Volume 2, paper 40935.

5. Qian, G., Shen, X., Luo, S., Jin, J., and Nowinski, W.L., "*Rapid and automatic atlas-based approach of Alzheimer's disease assessment by positron emission tomography neuroimages*", The 9th IEEE International Conference on Cognitive Informatics (ICCI 2010), Jul 7-9, 2010, Beijing, China, pp. 375-382.

6. Luo, S., Jin, J., Chalup, S., and Qian, G., "*A liver segmentation algorithm based on wavelets and machine learning*", 2009 International Conference on Computational Intelligence and Natural Computing (CINC 2009), Jun 6-7 2009, Wuhan, China, pp 122-125.

List of Abbreviations

AC	Anterior commissure
AD	Alzheimer's disease
ADNI	Alzheimer's disease neuroimaging initiative
ANOVA	Analysis of variance
APL	AC-PC line
CBI	Cerebellum inferior
CDR	Clinical dementia rating
CL	Candidate line
CSF	Cerebrospinal fluid
CPU	Central processing unit
CT	Computed tomography
DI	Dice's index
FAQ	Functional assessment questionnaire
FCAT	Federative committee on anatomical terminology
FDG	Fluoro-deoxy-glucose
fMRI	Functional MRI
FN	False negative
FP	False positive
FSL	FRMIB software library
GCL	Glucose consumption line
GM	Grey matter

GT	Ground truth
GTL	Group template
GVD	Group validation
HU	Hounsfield unit
IBSR	Internet brain segmentation repository
MCI	Mild cognitive impairment
MMSE	Mini mental state examination
MNI	Montreal Neurological Institute
MR	Magnetic resonance
MRA	MR angiography
MRI	MR imaging
MSL	Midsagittal line
MSP	Midsagittal plane
NPI	Neuropsychiatric inventory
PC	Posterior commissure
PET	Positron emission tomography
ROI	Region of interest
SD	Standard deviation
SE	Structuring element
SI	Symmetry index
SOF	Superior orbital fissure
SPM	Statistical parametric mapping
SPSS	Statistical package for social sciences
SSP	Stereotactic surface projections
T	Tesla

TN	True negative
TP	True positive
VAC	Coronal plane passing through AC
VCB	Coronal plane passing through the most superior point of cerebellum
VPC	Coronal plane passing through PC
VTK	Visualization toolkit
WM	White matter

Appendices

A. Mini Mental State Examination (MMSE)

Patient's Name: _____ Date: _____

Instruction: Ask the questions in the order listed. Score one point for each correct response within each question or activity.

Maximum Score	Patient's Score	Questions
5		"What is the year? Season? Date? Day of the week? Month?
5		"Where are we now: State? Country? Town/city? Hospital? Floor?
3		The examiner names three unrelated objects clearly and slowly, then asks the patient to name all three of them. The patient's response is used for scoring. The examiner repeats them until patient learns all of them, if possible. Number of trials: _____
5		"I would like you to count backward from 100 by sevens." (93, 86, 79, 72, 65, …) Stop after five answers. Alternative: "Spell WORLD backwards." (D-L-R-O-W)
3		"Earlier I told you the names of three things. Can you tell me what those were?"
2		Show the patient two simple objects, such as a wristwatch and a pencil, and ask the patient to name them.
1		"Repeat the phrase: No ifs, ands, or buts."
3		"Take the paper in your right hand, fold it in half, and put it on the floor." (The examiner gives the patient a piece of blank paper.)
1		"Please read this and do what it says." (Written instruction is "Close your eyes.")
1		"Make up and write a sentence about anything." (This sentence must contain a noun and a verb.)
1		"Please copy this picture." (The examiner gives the patient a blank piece of paper and asks him/her to draw the symbol below. All 10 angles must be present and two must intersect.) 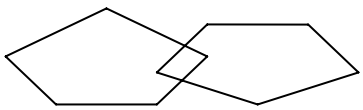
30		TOTAL

Instructions for administration and scoring of the MMSE

Orientation (10 points):

- Ask for the date. Then specifically ask for parts omitted (e.g. "Can you also tell me what season it is?"). One point for each correct answer.
- Ask in turn, "Can you tell me the name of this hospital (town, country, etc.)?" One point for each correct answer.

Registration (3 points):

- Say the names of three unrelated objects clearly and slowly, allowing approximately one second for each. After you have said all three, ask the patient to repeat them. The number of objects the patient names correctly upon the first repetition determines the cores (0-3). If the patient does not repeat all three objects the first time, continue saying the names until the patient is able to repeat al three items, up to six trials. Record the number of trials it takes for the patient to learn the words. If the patient does not eventually learn all three, recall cannot be meaningfully tested.
- After completing this task, tell the patient, "Try to remember the words, as I will ask for them in a little while."

Attention and Calculation (5 points):

- Ask the patient to begin with 100 and count backward by sevens. Stop after five subtractions (93, 86, 79, 72, 65). Score the total number of correct answers.
- If the patient cannot or will not perform the subtraction task, ask the patient to spell the word "world" backwards. The score is the number if letters in correct order (e.g. dlrow=5, dlorw=3)

Recall (3 points):

- Ask the patient if he or she can recall the three words your previously asked him or her to remember. Score the total number of correct answers (0-3).

Language and Praxis (9 points):

- Naming: Show the patient a wrist watch and ask the patient what it is. Repeat with a pencil. Score one point for each correct naming (0-2).
- Repetition: Ask the patient to repeat the sentence after you ("No ifs, ands, or buts."). Allow only one trial. Score 0 or 1.
- 3-Stage Command: Give the patient a piece of blank paper and say, "Take this paper in your right hand, fold it in half, and out it on the floor." Score one point for each part of the command correctly executed.
- Reading: On a blank piece of paper print the sentence, "Close your eye," in letters large enough for the patient to see clearly. Ask the patient to read the sentence and do what it says. Score one point only if the patient actually closes his or her eyes. This is nota test of memory, so you may prompt the patient to "do what it says" after the patient reads the sentence.
- Writing: Give the patient a blank piece of paper and ask him or her to write a sentence for you. Do not dictate a sentence; it should be written spontaneously. The sentence must contain a subject and a verb and make sense. Correct grammar and punctuation are not necessary.
- Coping: Show the patient the picture of two intersecting pentagons and ask the patient to copy the figure exactly as it is. All ten angles must be present and two must intersect to score one point. Ignore tremor and rotation.

(Folstein, Folstein & McHugh, 1975)

Interpretation of the MMSE

Method	Score	Interpretation
Single Cutoff	< 24	Abnormal
Range	< 21	Increased odds of dementia
	> 25	Decreased odds of dementia
Education	21	Abnormal for 8th grade education
	< 23	Abnormal for high school education
	< 24	Abnormal for college education
Severity	24-30	No cognitive impairment
	18-23	Mild cognitive impairment
	0-17	Severe cognitive impairment

Source:

- Crum RM, Anthony JC, Bassett SS, Folstein MF. Population-based norms for the mini-mental state examination by age and educational level. *JAMA*. 1993;269(18):2386-2391.
- Folstein MF, Folstein SE, McHugh PR. "Mini-mental state": a practical method for grading the cognitive state of patients for the clinician. *J Psychiatr Res*. 1975;12:189-198.
- Rovner BW, Folstein MF. Mini-mental state exam in clinical practice. *Hosp Pract*. 1987;22(1A):99, 103, 106, 110.
- Tombaugh TN, McIntyre NJ. The mini-mental state examination: a comprehensive review. *J Am Geriatr Soc*. 1992;40(9):922-935.

B. Clinical Dementia Rating (CDR)

Parameters:

- memory
- orientation
- judgment and problem solving
- community affairs
- home and hobbies
- personal care

Score the impairment when decline is due to cognitive loss not impairment from other causes.

Impairment	Points
None (normal)	0
Questionable	0.5
Mild impairment	1
Moderate impairment	2
Severe impairment	3

Parameter	Finding	Points
Memory	No memory loss or slight inconstant forgetfulness	0
	Consistent slight forgetfulness; partial recollection of events; "benign" forgetfulness	0.5
	Moderate memory loss; more marked for recent events; defect interferes with everyday activities	1
	Severe memory loss; only highly learned material retained; new material rapidly lose	2
	Severe memory loss; only fragments remain	3
Orientation	Fully oriented	0
	Fully oriented except for slight difficulty with time relationships	0.5
	Moderate difficulty with time relationships; oriented to place at examination; may have geographic disorientation elsewhere	1
	Severe difficulty with time relationships; usually disoriented to time often to place	2
	Oriented to person only	3

Judgment and problem solving	Solves everyday problems and handles business and financial affairs well; judgment good in relation to past performance	0
	Slight impairment in solving problems similarities and differences	0.5
	Moderate difficulty in handing problems similarities and differences; social judgment usually maintained	1
	Severely impaired in handling problems similarities and differences; social judgment usually impaired	2
	Unable to make judgment or solve problems	3
Community affairs	Independent function at usual level in job shopping and volunteer and social groups	0
	Slight impairment in these activities	0.5
	Unable to function independently in these activities although may still be engaged in some; appears normal to casual inspection	1
	Appears well enough to be taken to functions outside of the family home; unable to function independently outside of home	2
	Appears to ill to be taken to function outside of family home; unable to function independently outside of home	3
Home and hobbies	Life at home hobbies and intellectual interests well maintained	0
	Life at home hobbies and intellectual interests slightly impaired	0.5
	Mild but definite impairment of function at home; more difficult chores abandoned more complicated hobbies and interests abandoned	1
	Only simple chores preserved; very restricted interests poorly maintained	2
	No significant function in home	3
Personal care	Fully capable of self-care	0
	Needs prompting	1
	Requires assistances in dressing hygiene keeping of personal effects	2
	Requires much help with personal care; frequent incontinence	3

where, in personal care there is no questionable category.

- If unable to decide between 2 categories of impairment ("draw") then select the higher impairment.
- If aphasia is present to a greater degree than the general dementia then rate based on the general level of dementia based on nonlanguage cognitive function.

Interpretations:

- Memory is the primary category and the other 5 are secondary.

Results	CDR Value
3 to 5 secondary categories same as M	M
1 secondary categories same as M with 2 greater and 2 less	M
2 secondary categories same as M with 2 greater and 1 less	M
2 secondary categories same as M with 1 greater and 2 less	M
3 to 5 secondary categories > M	Value for majority > M; if tied use value closest to M
M = 0.5 and 3 to 5 secondary categories >= 1.0	1
M = 0 and 2 to 5 secondary categories >= 0.5	0.5
3 to 5 secondary categories < M	Value for majority < M; if tied use value closet to M
3 to 5 secondary categories 0 and M >= 1	0.5
3 secondary categories > M and 2 categories < M	M

References:

- Morris JC. The clinical Dementia Rating (CDR): Current version and scoring rules. Neurology. 1993; 43:2412-2414